Characterization and Fabrication of In and Ga Dual-doped ZnO Thermoelectric Ceramics by Spark Plasma Sintering

ジョン, アロン

Ph. D. Thesis

Characterization and Fabrication of In and Ga Dual-doped ZnO Thermoelectric Ceramics by Spark Plasma Sintering

In、Ga 共ドープ ZnO 系酸化物 放電プラズマ焼結体の熱電特性評価

Department of Applied Science for Electronics and Materials
Interdisciplinary Graduate School of Engineering Sciences
Kyushu University

ジョン　アロン
JEONG AHRONG

Supervisor: Prof. Byung-Koog Jang

January, 2023

博 士 学 位 論 文

Characterization and Fabrication of In and Ga Dual-doped ZnO Thermoelectric Ceramics by Spark Plasma Sintering

In、Ga 共ドープ ZnO 系酸化物放電プラズマ焼結体の熱電特性評価

九州大学
大学院総合理工学府
量子プロセス理工学専攻

ジョン　アロン
JEONG AHRONG

指導教員：張 炳國

2023 年　1 月

論文調査委員会

主査　九州大学　教授　　張　炳國
副査　九州大学　教授　　大瀧　倫卓
副査　九州大学　准教授　末國　晃一郎
副査　九州大学　准教授　渡邉　賢
副査　九州大学　教授　　宮崎　康次（工学府）

Abstract

ZnO-based materials have received considerable attention in energy harvesting, such as photovoltaic, piezoelectric, and thermoelectric (TE) applications. ZnO is the most anticipated TE material, which has advantages such as a large Seebeck coefficient, nontoxicity, and good thermal stability. Even though ZnO is a promising candidate as a TE material, the drawback of ZnO is its high thermal conductivity. Oxide materials such as ZnO allow for a simple preparation starting from precursors by spark plasma sintering (SPS), which has proven to be capable of consolidating bulk ceramic bodies using an electric field and short sintering time with fine-grained microstructures showing superior properties.

The principal objective of this thesis is to investigate the fabrication of In- and Ga-doped ZnO with various amounts of dopants, and then the effect of two-step sintering and SPS (TS-SPS) conditions on the TE properties. The influence of the doping was evaluated to increase the low intrinsic electrical conductivity by increasing the carrier concentrations of ZnO, and the TS-SPS process was applied to suppress grain-growth for reduction of the thermal conductivity through the enhancement of phonon scattering thereby increasing the dimensionless figure of merit (*ZT*). The following is the accomplishment of this thesis.

In Chapter 1, an introduction to basic principles of the thermoelectric conversion, research and development trends, typical oxide-based thermoelectric materials, and SPS methods is presented. In particular, the motivation and final target of this study and the main objectives of each chapter are briefly summarized.

In Chapter 2, crystal structure and microstructural analyses of In and Ga-doped ZnO TE ceramics, $[Zn_{(1-x-y)}Ga_xIn_y]O$ (x = 0, 0.02; y = 0, 0.005, 0.01, 0.02), were conducted to confirm the solubility of the dopants and to understand the correlations between the crystallographic

phases and the chemical compositions. It can be concluded that the addition of In contributed to an increase in the solubility of Ga because the doping with In and Ga (x = 0.02; y = 0.005) resulted in a higher doping of Ga, and the highest power factor (*PF*) of 0.99 mW K^{-2} m^{-1} was acquired at 773°C.

In Chapter 3, In single-doped $[Zn_{(1-y)}In_y]O$ (y = 0.005, 0.01, 0.02, 0.03, 0.05) and In and Ga dual-doped $[Zn_{(1-x-y)}Ga_xIn_y]O$ (y = 0.005; x = 0.005, 0.01, 0.02, 0.03, 0.05) ceramics were fabricated to compare the effect of single- and dual-doping. The microstructural and chemical composition analyses revealed that the single-doped ZnO ($y \geq 0.02$) and dual-doped ZnO (y = 0.005; $x \geq 0.02$) contained secondary phases of $Zn_7In_2O_{10}$ and $ZnGa_2O_4$, respectively. The segregation of $ZnGa_2O_4$ phase decreased the electrical conductivity so that the highest *PF* of 1.05 mW K^{-2} m^{-1} at 773°C was achieved by the lightly dual-doped $[Zn_{(1-x-y)}Ga_xIn_y]O$ sample with x = 0.05 and y = 0.005 without $ZnGa_2O_4$ phase. The dual-doped ZnO ceramics thereby showed an improved TE performance, attaining the *ZT* of 0.17 at 773°C as compared to 0.12 of pure (non-doped) ZnO.

In Chapter 4, pure ZnO ceramics were consolidated by SPS along with one-step/two-step sintering (OS/TS) temperature profiles, the latter employing a strategy of heating to a higher temperature (T_1) for achieving a critical density of > 90% theoretical density followed by prolonged sintering at a lower temperature (T_2) for densification while preventing grain-growth. Electron backscatter diffraction (EBSD) showed a noticeable grain-growth suppression of 56% (reduced from 8.1 to 3.6 μm) for TS-1100-120 (TS-T_1-duration of second-step sintering at 1050°C) sample fabricated by the TS and SPS processes (TS-SPS). As a result, TS-SPS process was revealed to be effective to achieve the highest *PF*, 7.8×10^{-5} W K^{-2} m^{-1} (higher than that of the pure ZnO in Chapter 3), and a *ZT* of 0.017 at 775°C (TS-1100-120).

In Chapter 5, in order to optimize the TS-SPS process, pure and In-doped ZnO ceramics were successfully prepared by SPS with the OS/TS temperature profiles. The strategy of the TS temperature profile was the same as explained in Chapter 4. The EBSD analysis indicated a grain-growth suppression of 14.0% and 21.8% for the pure/In-doped TS-SPS samples as compared with OS-SPS samples, respectively. The microstructure control by TS-SPS resulted in the most improved *PF* of 1.0 mW K^{-2} m^{-1} in I-TS-950 sample and an increased *ZT* (55.2%, from 0.125 to 0.194 compared with I-OS-1150) at 773°C, and a decrease of grain sizes from 7.8 μm (I-OS-1150) to 6.1 μm (I-TS-950). The *PF* value was higher than that of the In-doped ZnO sample in Chapter 3, proving that the TS-SPS process is an effective strategy for improving *PF*, strongly suggesting that the carrier doping to TS-SPS ZnO achieves much higher *PF* and, therefore, higher *ZT* values.

The comprehensive experimental results and conclusions of each chapter of the Ph.D. thesis are summarized **in Chapter 6**.

List of Figures

Figure 1. Energy statistics from several sources of waste thermal energy and energy recovering by TE generators 1

Figure 2. Schematics of a) a typical RTG and b) its inside of components..... 3

Figure 3. Typical energy path for a vehicle equipped with an internal combustion engine powered by gasoline. 4

Figure 4. Schematics for the mechanism of the Peltier Effect and Seebeck Effect..... 5

Figure 5. The dependencies of the S, σ, and κ values on the carrier concentration..... 9

Figure 6. TE materials classified based on typical waste heat and heat-recovery range..... 10

Figure 7. The development of the maximum ZT values of bulk TE materials throughout the past decades. 11

Figure 8. Crystal structures of layered cobalt oxides 13

Figure 9. Representation of the development of thermoelectric oxides over the years..... 14

Figure 10. Crystal structure of STO 16

Figure 11. Crystal structure of ZnO..... 18

Figure 12. Schematic diagrams of SPS equipment. 22

Figure 13. Illustrative representation of the differences between the two TSS sintering plots. 23

Figure 14. (a) Wurtzite crystal structure of ZnO and (b) view of ZnO along the c-axis with the unit cell. Wyckoff positions for the space group $P6_3mc$ (186) are described..... 39

Figure 15. XRD patterns of examined SPSed (a) pure ZnO and (b)–(e) $[Zn_{(1-x-y)}Ga_xIn_y]O$ (x = 0.02); (b) y = 0, (c) y = 0.005, (d) y = 0.01, and (e) y = 0.02 41

Figure 16. BSE images of SPSed $[Zn_{(1-x-y)}Ga_xIn_y]O$ (x = 0.02); (a) y = 0, (b) y = 0.005, (c) y = 0.01, and (d) y = 0.02. The white area is composed of Zn–Ga–In–O with a high

amount of In 42

Figure 17. EDS maps of In and Ga in $[Zn_{(1-x-y)}Ga_xIn_y]O$ (x = 0.02); (a) y = 0, (b) y = 0.005, (c) y = 0.01, and (d) y = 0.02 46

Figure 18. Lattice constants with respect to the nominal concentration of $[Zn_{(1-x-y)}Ga_xIn_y]O$ (x = 0.02; y = 0, 0.005, 0.01, 0.02) and pure ZnO. 48

Figure 19. Temperature dependence of the (a) electrical conductivity σ, (b) Seebeck coefficient S, and (c) power factor $S^2\sigma$ of $[Zn_{(1-x-y)}Ga_xIn_y]O$ (x = 0.02; y = 0, 0.005, 0.01, 0.02) 50

Figure 20. Temperature dependence of the (a) total thermal conductivity (κ_{tot}), (b) electron thermal conductivity (κ_{el}), and (c) lattice thermal conductivity (κ_{lat}) of $[Zn_{(1-x-y)}Ga_xIn_y]O$ (x = 0.02; y = 0, 0.005, 0.01, 0.02) and pure ZnO. 53

Figure 21. Dimensionless figure of merit (ZT) of $[Zn_{(1-x-y)}Ga_xIn_y]O$ (x = 0.02; y = 0, 0.005, 0.01, 0.02) 56

Figure 22. Powder XRD patterns of (a) pure ZnO and the In single-doped $[Zn_{(1-y)}In_y]O$ sintered ceramics: y = (b) 0.005, (c) 0.01, (d) 0.02, (e) 0.03, and (f) 0.05. The right panel shows the expanded view over a range of 2θ = 31–38° 68

Figure 23. Microstructures of the polished surfaces of the In single-doped $[Zn_{(1-y)}In_y]O$ sintered ceramics: y = (a) 0.005, (b) 0.01, (c) 0.02, (d) 0.03, and (e) 0.05 in the BSE mode of SEM. The normalized atomic compositions of (e) marked as A, B, and C were measured using the EDS point analysis results. 70

Figure 24. EDS elemental mapping of In for the In single-doped $[Zn_{(1-y)}In_y]O$ sintered ceramics: y = (a) 0.005, (b) 0.01, (c) 0.02, (d) 0.03, and (e) 0.05 72

Figure 25. Powder XRD patterns of (a) pure ZnO, and the In and Ga dual-doped $[Zn_{(1-x-y)}Ga_xIn_y]O$ sintered ceramics: y = 0.005; x = (b) 0.005, (c) 0.01, (d) 0.02, (e) 0.03, and (f) 0.05 73

Figure 26. Microstructures of the polished surfaces of the In and Ga dual-doped $[Zn_{(1-x-y)}Ga_xIn_y]O$ sintered ceramics: y = 0.005; x = (a) 0.005, (b) 0.01, (c) 0.02, (d) 0.03, and (e) 0.05 in the BSE mode of SEM. The normalized atomic compositions of (e) marked as A, B, C, and D were measured using the EDS point analysis results. 75

Figure 27. EDS elemental mapping of In and Ga for the In and Ga dual-doped $[Zn_{(1-x-y)}Ga_xIn_y]O$ sintered ceramics: y = 0.005; x = (a) 0.005, (b) 0.01, (c) 0.02, (d) 0.03, and (e) 0.05. The relative concentration of Ga in the same area are shown as the inset of each panel in a pink color..... 76

Figure 28. Temperature dependence of (a, b) the electrical conductivity σ, (c, d) the Seebeck coefficient S, and (e, f) the power factor $S^2\sigma$: (a), (c), and (e) of pure ZnO and the In single-doped ZnO, and (b), (d), and (f) of the In and Ga dual-doped ZnO sintered ceramics, respectively. The S of pure ZnO is given in the inset of (c) 78

Figure 29. Temperature dependence of (a, b) the total thermal conductivity κ_{tot}, (c, d) the electron thermal conductivity κ_{ele}, and (e, f) the lattice thermal conductivity κ_{lat} are shown: (a), (c), and (e) of pure ZnO and the In single-doped ZnO, and (b), (d), and (f) of the In and Ga dual-doped ZnO sintered ceramics, respectively 81

Figure 30. Dimensionless figure of merit ZT of (a) pure ZnO and the In single-doped ZnO, and (b) the In and Ga dual-doped ZnO sintered ceramics 83

Figure 31. Powder XRD patterns of nanosized (a) pure ZnO, and the In and Ga dual-doped $[Zn_{(1-x-y)}Ga_xIn_y]O$ sintered ceramics: y = 0.005; x = (b) 0.005, (c) 0.01, (d) 0.02, (e) 0.03, and (f) 0.05 85

Figure 32. Temperature dependence of the (a) electrical conductivity (σ), (b) Seebeck coefficient (S), and (c) power factor $S^2\sigma$ of nanosized $[Zn_{(1-x-y)}Ga_xIn_y]O$ (y = 0.005; x = 0.005, 0.01, 0.02, 0.03, 0.05) and pure ZnO 86

Figure 33. AFM images of $[Zn_{(1-x-y)}Ga_xIn_y]O$ (y = 0.005), (a) x = 0.005, (b) x = 0.01, (c) x = 0.02, (d) 0.03, and (e) 0.05 ZnO epitaxial layer on YSZ (111)..... 87

Figure 34. Lattice constant with respect to the nominal concentration of $[Zn_{(1-x-y)}Ga_xIn_y]O$ (y = 0.005; x = 0.005, 0.01, 0.02, 0.05) and pure ZnO.....88

Figure 35. The power factor $S^2\sigma$ with respect to the nominal concentration of $[Zn_{(1-x-y)}Ga_xIn_y]O$ (y = 0.005; x = 0.005, 0.01, 0.02, 0.03, 0.05).....89

Figure 36. Temperature profiles of OS/TS-SPS processes for ZnO ceramic samples. 101

Figure 37. X-ray diffraction patterns of the OS/TS-SPS ZnO samples in Table 6. The first-step sintering of (a)–(d) was at 1100°C for 15 min, while that of (e)–(h) was at 1150°C for 5 min. The second-step was maintained at 1050°C for 30, 60, and 120 min for (b) and (f), (c) and (g), and (d) and (h), respectively. 102

Figure 38. IPF maps of the OS/TS-SPS ZnO. The samples are (a) OS-1100, (b) TS-1100-30, and (c) TS-1100-120. The map colors are assigned using the IPF color scale shown in (a). 104

Figure 39. Temperature dependence of (a, b) the electrical conductivity σ, (c, d) the Seebeck coefficient S, and (e, f) the power factor $S^2\sigma$. The first-step sintering conditions of (a), (c), and (e) were 1100°C for 15 min, and those for (b), (d), and (f) were 1150°C for 5 min..... 107

Figure 40. Temperature dependence of the thermal conductivity κ of the OS/TS-SPS ZnO ceramic samples. The first-step sintering condition of (a) was 1100°C for 15 min, while that of (b) was 1150°C for 5 min 108

Figure 41. Dimensionless figure of merit ZT of the OS/TS-SPS ZnO. The first-step sintering condition of (a) was 1100°C for 15 min, while that of (b) was 1150°C for 5 min. 109

Figure 42. Temperature profiles of the OS/TS-SPS processes for (a) pure and (b) In-doped ZnO

ceramic samples. 120
Figure 43. X-ray diffraction patterns of (a)–(f) pure and (g)–(k) In-doped ZnO samples sintered by OS/TS-SPS in Table 8. The first-step sintering of (a)–(j) was at 1150°C for 15 min. The second-step sintering was maintained over a temperature range of 900–1100°C for 30 min..... 121
Figure 44. Fundamental phenomena of sintering under the driving force, Δ (γA).....123
Figure 45. Schematics of the sintering process at (a) early, (b) Intermediate, and (c) final stage.....124
Figure 46. Mass transport paths in the formation and growth of necks between particles during sintering.....126
Figure 47. Inverse pole figure (IPF) maps of the OS/TS-SPS pure and In-doped ZnO. The samples are (a) P-OS-1150, (b) P-TS-950, (c) I-OS-1150, and (d) I-TS-950. The EBSD color maps are assigned using the IPF color scale shown in (a)..... 128
Figure 48. Temperature dependences of (a, b) the electrical conductivity σ, (c, d) the Seebeck coefficient S, and (e, f) the power factor $S^2\sigma$ are shown: (a), (c), and (e) OS/TS-SPS pure and (b), (d), and (f) In-doped ZnO ceramic samples. First-step sintering of all samples was at 1150°C for 15 min. Second-step sintering was maintained over a temperature range of 900–1100°C for 30 min, and the number of "XX" in TS-XX samples indicated each sintering temperature..... 130
Figure 49. Temperature dependence of the thermal conductivity κ of (a) the OS/TS-SPS pure and (b) the In-doped ZnO ceramic samples. First-step sintering of all samples was at 1150°C for 15 min. Second-step sintering was maintained over a temperature range of 900–1100°C for 30 min, and the number of "XX" in TS-XX samples indicated each sintering temperature. 131
Figure 50. Dimensionless figure of merit ZT of (a) the OS/TS-SPS pure and (b) In-doped ZnO

ceramic samples. First-step sintering of all samples was at 1150°C for 15 min. Second-step sintering was maintained over a temperature range of 900–1100°C for 30 min, and the number of “XX” in TS-XX samples indicated each sintering temperature. 133

List of Tables

Table 1. Relative density of SPSed pure ZnO and $[Zn_{(1-x-y)}Ga_xIn_y]O$ with various compositions. 42

Table 2. Sintering aids and grain-growth inhibitors. 44

Table 3. Atomic composition of the ZnO matrix determined by EDS point analysis of SPSed $[Zn_{(1-x-y)}Ga_xIn_y]O$ (x = 0.02; y = 0, 0.005, 0.01, 0.02). The standard deviations of the mean atomic composition are given in parentheses. 47

Table 4. Relative densities of the single/dual-doped $[Zn_{(1-x-y)}Ga_xIn_y]O$ sintered ceramics with different compositions 71

Table 5. Chemical composition of the primary phase of the single/dual-doped $[Zn_{(1-x-y)}Ga_xIn_y]O$ ceramics, as estimated from the EDS point analysis results. The composition was normalized oxygen by setting the total to 100 77

Table 6. Conditions of the OS/TS-SPS processes for ZnO ceramic samples 101

Table 7. Relative densities of the OS/TS-SPS ZnO under various conditions 103

Table 8. Sintering conditions of the OS/TS-SPS processes for pure and In-doped ZnO ceramic samples. 119

Table 9. Relative densities of the OS/TS-SPS processes for pure and In-doped ZnO with various sintering conditions 122

Contents

Abstract ..... **I**

List of Figures ..... **IV**

List of Tables ..... **X**

Contents ..... **XI**

Chapter 1. Introduction **1**

1.1. Backgrounds 1

1.1.1. Energy Needs and Wasted Energy 1

1.1.2. Thermoelectric Applications 2

1.1.3. Fundamentals for Thermoelectrics 4

1.2. High Temperature Thermoelectric Materials 10

1.2.1. Metal Oxide 12

1.2.2. *p*-type Metal Oxides 12

1.2.3. *n*-type Metal Oxides 15

1.2.3.1. $SrTiO_3$-based Materials 15

1.2.3.2. ZnO-based Oxides 17

1.3. Advanced Sintering Technologies 20

1.3.1. Spark Plasma Sintering (SPS) 20

1.3.2. Two-Step Sintering (TSS) 22

1.4. Motivation and Objectives 25

References 28

Chapter 2. Thermoelectric Properties of In- and Ga-doped Spark Plasma Sintered ZnO Ceramics **35**

2.1. Introduction 35

2.2. Experimental Procedures 37

2.3. Results and Discussion 39

2.3.1. Crystal Structure Analysis of In- and Ga-doped ZnO 39

2.3.2. Microstructural Analysis 41

2.3.3. Electrical Conductivity 49

2.3.4. Thermal Conductivity and Dimensionless Figure of Merit 51

2.4. Conclusions 57

References 58

Chapter 3. Thermoelectric Performance of In and Ga Single/Dual-doped ZnO Ceramics Fabricated by SPS 63

3.1. Introduction 63

3.2. Experimental Procedures 65

3.3. Results and Discussion 68

3.3.1. In Single-doped ZnO 68

3.3.1.1. Crystal Phase 68

3.3.1.2. Microstructure and Phase Transition 69

3.3.2. In and Ga Dual-doped ZnO 72

3.3.2.1. Crystal Phase 72

3.3.2.2. Microstructure and Phase Transition 74

3.3.3. Thermoelectric Properties of Single/Dual-doped ZnO 76

3.3.4. Crystal Phase and Electrical Conductivity of Single/Dual-doped Nanosized ZnO 84

3.3.5. Thin Films of In and Ga Dual-doped ZnO 87

3.4. Conclusions 91

References 92

Chapter 4. Characterization of ZnO Thermoelectric Ceramics and Their Microstructures Consolidated by Two-Step Spark Plasma Sintering 97

4.1. Introduction 97

4.2. Experimental Procedures 99

4.3. Results and Discussion 102

4.3.1. Microstructural Analysis of ZnO 102

4.3.2. Thermoelectric Properties 106

4.4. Conclusions 110

References 111

Chapter 5. Effects of Two-Step Spark Plasma Sintering on the Microstructures and Thermoelectric Properties of Pure/In-doped ZnO 115

5.1. Introduction 115

5.2. Experimental Procedures 117

5.3. Results and Discussion 121

5.3.1. Microstructural Analysis of Pure/In-doped ZnO 121

5.3.2. Thermoelectric Properties 128

5.4. Conclusions 134
References 135
Chapter 6. Conclusions 139
Research Achievements 142
Acknowledgments 144

Chapter 1. Introduction

1.1. Backgrounds

1.1.1. Energy Needs and Wasted Energy

Owing to the limited supply of fossil fuels and the global climate by human-induced, a new energy crisis has been realized in the 21st century, and it causes the use of green energy and alternative energy resources [1]. Consumption of energy resources is increasing significantly, mainly the consumption of fossil fuels due to industrial development and population increase. In industrial environments or daily life, it is not possible to use the generated heat energy effectively in large quantities, so it is inevitable to be wasted in environments such as factory boiler emissions, car exhaust, and friction.

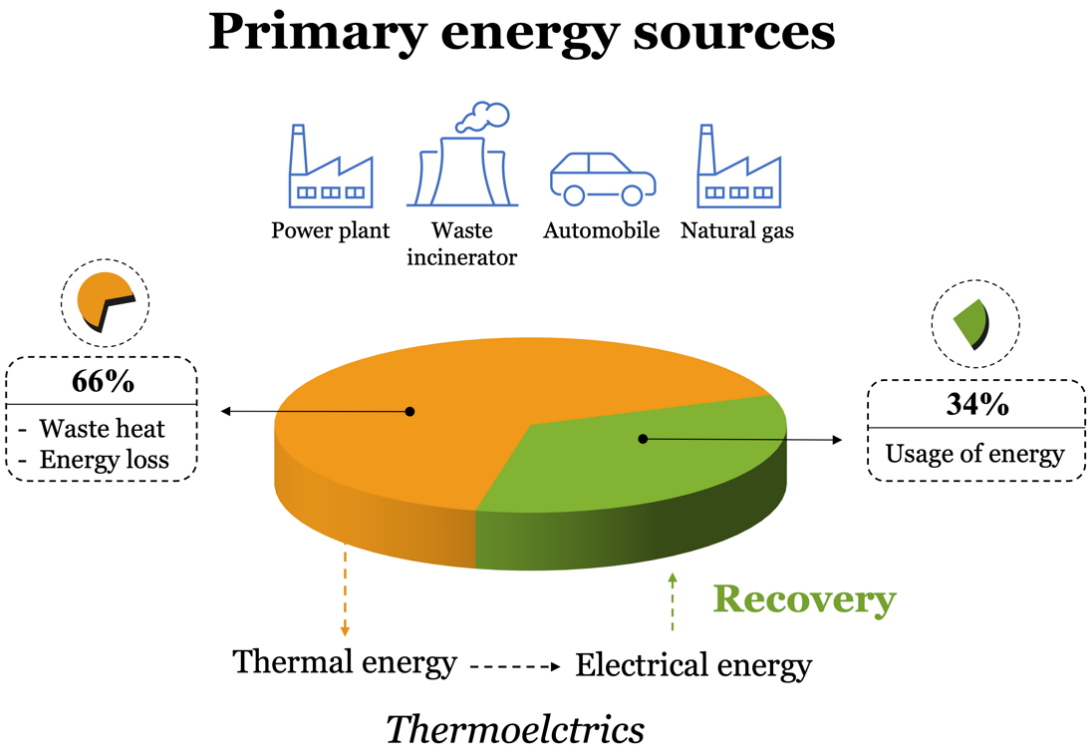

Fig. 1. Energy statistics from several sources of waste thermal energy and energy recovering by TE generators.

The main cause of waste heat is the transport sector, and only 34% of fuel energy with useful energy. In comparison, aviation and automobiles are examples of high energy use with low efficiency, where approximately 66% of the energy generated during combustion is lost in the form of heat from turbine/exhaust or engine cooling water. The usage of primary energy schematically shows various sectors, and the waste heat can be converted into electrical energy through the placement of thermoelectric (TE) materials as shown in Fig. 1. Thus, the key solution to solve large waste of thermal energy (over 60%) is an indispensable energy harvesting technology for efficiently recycling the wasted energy. In addition to finding alternative energy sources such as solar, thermal, wind, hydrogen energy, and biomass energy is a convenient and a practical solutions by increasing energy utilization efficiency to replace existing fossil fuels.

1.1.2. Thermoelectric Applications

TE devices have been applied for a long time because they can generate state power generation or refrigeration without noise or vibration, having many advantages such as high sensitivity to temperature changes and emission-free operation. These features are a great advantage when TE materials are used in various fields such as remote power supply (radioisotope thermoelectric generators, RTGs), automotives, temperature sensors, control devices, water condensation, and implantable or wearable devices [2–5]. The development of high-performance TE devices has progressed greatly so far, and it will be introduced in detail below.

As representative applications of TE materials, RTGs and automotive TE generators (TEGs) have been developed with high efficiency. RTG has always been a reliable and robust power source for remote power supply due to its high energy density and excellent long life without maintenance and refueling that cannot otherwise obtain sufficient other means. The

RTG applications include deep ocean exploration and aerospace missions such as Apollo lunar and Mars landers. In these systems, the RTGs typically consisted of radioisotope heat sources, thermal insulators, and TE converters as shown in Fig. 2. The heat source of RTG is supplied from nuclear decay of radioactive isotopes so that it is covered with protective heat insulators, and provides a stable heat flow that can be converted into electricity in the TE converter. The output energy density and efficiency of RTGs depend heavily on TE converters. In the RTG, the high temperature side of the TE device is typically controlled over the temperature range of 800–1200 K so that components of the devices are chosen from high performance TE materials at a high temperature.

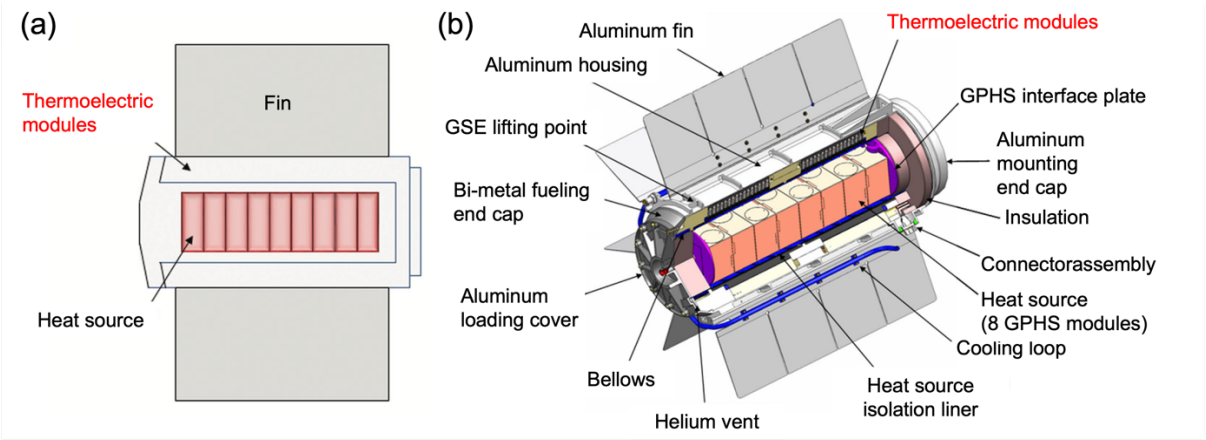

Fig. 2. Schematics of a) a typical RTG and b) its inside of components (revised from [2,3]).

The efficiency of the combustion engine is less than 30% because of the vehicle exhaust or cooling system as shown in Fig. 3. This waste heat can be collected and utilized by TE material to generate electricity, improving fuel efficiency and reducing CO_2 emissions. A well-developed TE device can also improve the efficiency of air conditioning in vehicles. The exhaust TEG is possible to convert waste heat from the exhaust gas containing 40% of the energy by fuel combustion into electricity. The exhaust gas temperature can be over the

temperature range of 500-1073 K downstream, providing the hot side for TE modules in the middle-high temperature.

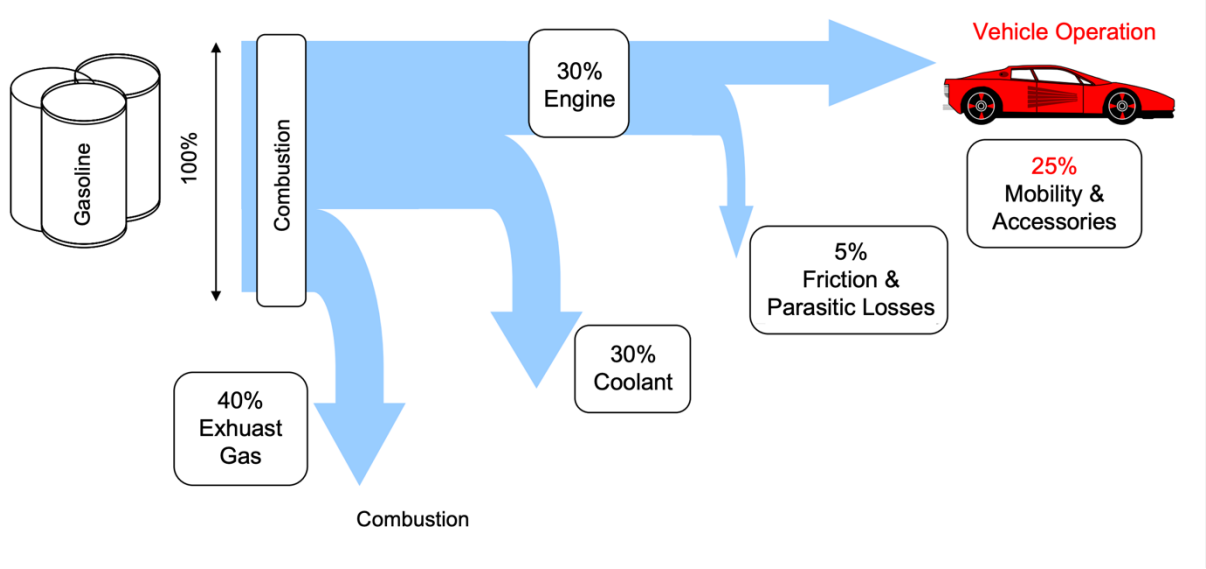

Fig. 3. Typical energy path for a vehicle equipped with an internal combustion engine powered by gasoline (revised from [6]).

1.1.3. Fundamentals for Thermoelectrics

The TE effect, also known as the Seebeck effect, is the direct conversion of temperature differences between two different electric conductors or semiconductors into electric voltages. When the sides of the TE material are exposed to different temperatures, voltage is generated on both sides of the material. Conversely, applying a voltage can cause a temperature difference called the Peltier effect. At the atomic scale, if temperature gradients are applied to both ends of a thermocouple, the electron and hole move faster, the density of the high-temperature side decreases, and the electron/hole diffuses to the low-temperature side as schematically illustrated in Fig. 4. This movement of the carrier (holes in *n*-type electrons and *p*-type materials) is converted into the generation of electric fields across the thermocouple. This is

called the Seebeck effect, and the voltage generated for the temperature difference ΔT under thermodynamic equilibrium is $S \times \Delta T$, where S is the Seebeck coefficient. Therefore, TE materials are one of the potential candidates for harvesting the thermal energy of waste because they have the ability to convert the thermal energy of waste into electricity even under a very low temperature gradient for environmental temperatures. This technology represents a clear advantage over other energy acquisition technologies. Firstly, TE conversion is reliable and operates in silence as it works without mechanical movement. Secondly, it is an environmentally friendly green technology, since no heat and no gaseous or chemical wastes are produced during operation. Lastly, it can be widely used in places where other energy conversion technologies are unavailable, such as in the remote outer space, etc. [7].

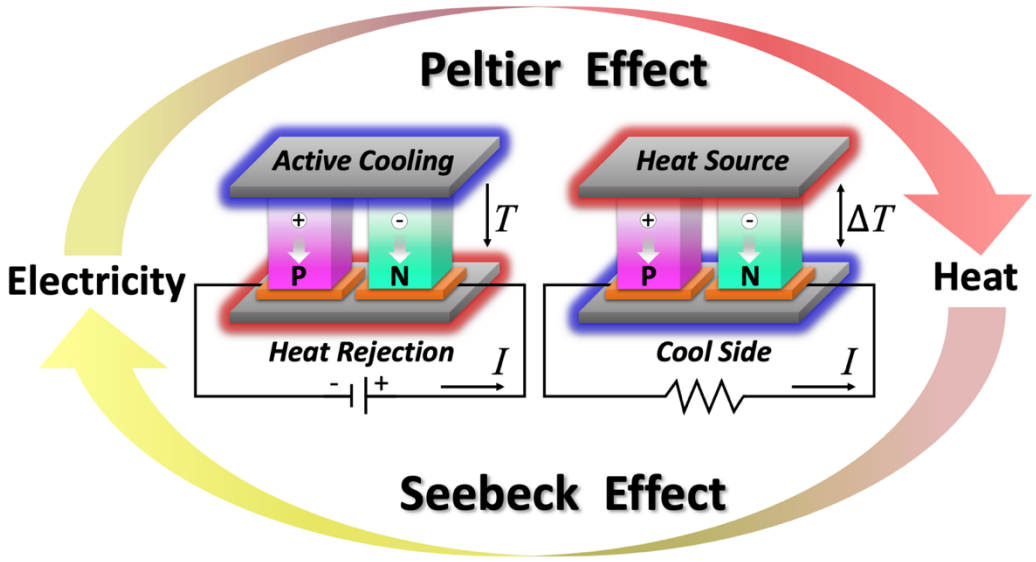

Fig. 4. Schematics for the mechanism of the Peltier Effect and Seebeck Effect.

The TE effect includes three different effects: (i) the Seebeck effect, (ii) the Peltier effect, and (iii) the Thomson effect. The Seebeck effect and the Peltier effect are often called the Peltier-Seebeck effect as different representations of the same physical process. The Thomson effect is an extension of the Peltier-Seebeck model and is trusted by Kelvin. In 1821, Seebeck

created a circuit of two different metals, copper (Cu) and bismuth (Bi), exposing two edge joints at different temperatures (high temperatures/low temperatures), and the applied temperature gradient produced a voltage (experimentally observed that the compass magnet was biased), commonly called the Seebeck effect [7,8]. Later, in 1834, Peltier observed that current flowing to Cu and Bi lines at room temperature could cause temperature differences, known as the Peltier effect, which is widely deployed in the refrigeration process. The Seebeck effect provides a theoretical basis for TE transducer (energy harvesting) applications, and the Peltier effect is applied to cooling devices (refrigeration). Until now, TE materials have been widely used in many high-tech applications, including aerospace, military, medical thermostats, microsensors, and wearables. Seebeck effect can be elucidated through the second law of thermodynamics and the change of entropy. The Seebeck effect converts some of the thermal energy into electromotive force due to the temperature gradient, inside the TE materials, which is not contradicted by the second law. The relationship between the Seebeck and entropy is given by the following equations:

$$\Delta S = \frac{Q}{T} \qquad (1)$$

where ΔS is the change in entropy, Q is the heat transferred, and T is the temperature at the changes occurred.

The Seebeck coefficient could be explained by the law of thermodynamic as the entropy transported per charge carrier [9], and is written as:

$$S = \frac{1}{e}\frac{\partial S_{\mathrm{n}}}{\partial n} \qquad (2)$$

where n is the carrier density and S_{n} the entropy density of the charge carriers, and e is the

electronic charge. So the change in entropy density could also be expressed as the total electronic heat capacity over the total number of carrier in the system, which can be obtained from the following relationship:

$$S = \frac{1}{e}\frac{C_{el}}{N} = \frac{1}{eN}\frac{\partial U_{el}}{\partial T} \qquad (3)$$

where C_{el} is the total electronic heat capacity for the system, N is the total number of carriers in the system, and U_{el} is the total thermal kinetic energy carried by the electrons. It is worth noting that not all charges contribute to the Seebeck coefficient, but those who take part in the conduction process. In the case of a semiconductor that has not degenerated, charge carriers need to be excited from the valence band across the bandgap to the conduction band so that it contributes to the Seebeck coefficient.

TE materials obey the TE or Seebeck effect described by the TE power, or thermopower, or Seebeck coefficient (S): S = ΔV / ΔT, where ΔV and ΔT are the electric potential difference and a temperature gradient, respectively. The Seebeck coefficient is used for the calculation of the power factor ($PF = S^2\sigma$) (σ is the electrical conductivity), a well-known entity for comparing the voltage output of different TE materials. The efficiency of TE materials is characterized by a dimensionless figure of merit (ZT): ZT = ($S^2\sigma$ /κ) × T, where σ represents the electric conductivity (S/m), S the Seebeck coefficient (μV/K), κ is the thermal conductivity (W K^{-1} m^{-1}) of materials and T the absolute temperature (K).

In recent years, great progress has been made in improving the ZT. It could be realized that an efficient TE material should exhibit high electrical conductivity combined with high Seebeck coefficient and low thermal conductivity. The Seebeck coefficient S, characteristic of the average entropy per charge transport, should be large in order to create a high voltage induced by a temperature gradient. The Seebeck coefficient, however, is not the only parameter

to be optimized in order to maximize *ZT*. The electrical conductivity (σ) must be large to minimize the Joule heating during charge transport. Apart from the two parameters mentioned, a good TE material should exhibit also low thermal conductivity (κ), to prevent heat flow through the material. These three factors are interdependent in bulk TE mate- rials, and altering one changes the other two. The difficulty in simultaneously optimizing them causes TE research to decay, until great reduction of thermal conductivity were both theoretically and experimentally proven in nanomaterials in 1993. The difficulty of designing high-performance TE materials arises from the fact that both electrical and thermal conductivities are related via the carrier concentration and, thus, optimizing one parameter will negatively affect the other. This interdependence has delayed the development of TE materials for many years. The energy conversion efficiency (η) of TE devices depend on the *ZT* values as defined in Eq. (4) [10].

$$\eta = \frac{\Delta T}{T_{\mathrm{h}}} \frac{\sqrt{1+ZT}-1}{\sqrt{1+ZT}+T_{\mathrm{c}}/T_{\mathrm{h}}} \qquad (4)$$

where DT/T_{h} is the Carnot efficiency and *ZT* is the dimensionless figure of merit of the material. It can be seen that with an increase in the *ZT* value, the conversion efficiency increases. Therefore, it is necessary to maximize the *ZT* value of TE materials by increasing their power factor (*PF*, $S^2\sigma$) and reducing the thermal conductivity in order to improve their TE performance. Various approaches, such as enhancement of phonon scattering by creating nanostructured grains or point defects [11], porous structure engineering [12–14], and reducing grain size [15,16], have also been proposed to reduce the thermal conductivity of ZnO.

This approximation yields a better estimation for κ_{el} and so the deduced κ_{lat} is als o more accurate. Thus, the all the TE parameters are dependent on the carrier concen tration, and can be optimized by the model of dependencies upon the carrier concentr ation, as plotted in Fig. 5.

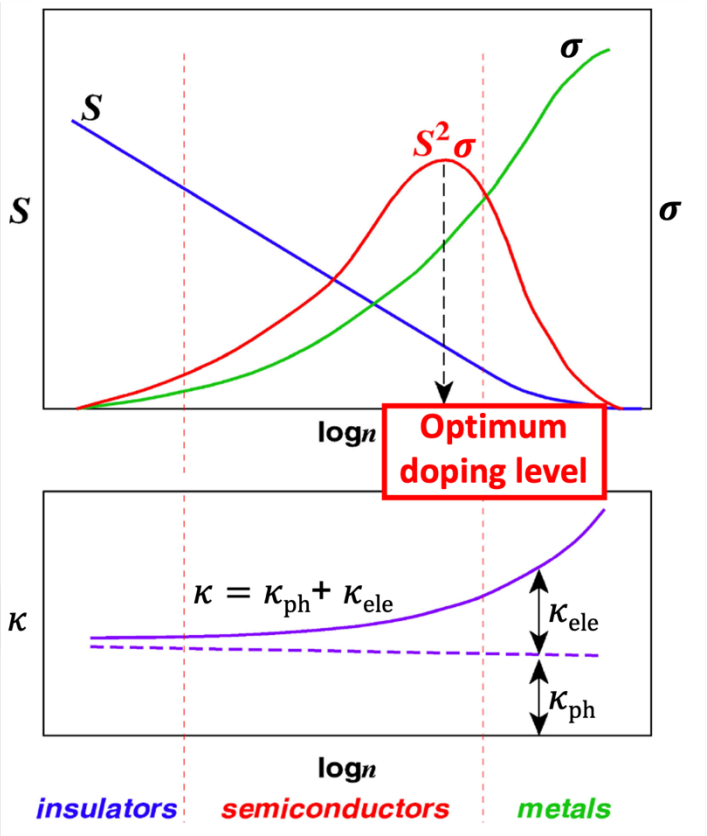

Fig. 5. The dependencies of the S, σ, and κ values on the carrier concentration [17].

Good TE materials often are heavily doped semiconductors with carrier concentration values between 10^{8} and 10^{21} cm^{-3} as predicted. TE materials with optimized carrier concentrations can be considered as the strategy for improving ZT. Nevertheless, simultaneous improvement of the three parameters σ, $|S|$ and κ_{ele}, is difficult to achieve since they all depend on carrier concentration. Another simple way is to reduce κ_{lat} by using an additional phonon scattering mechanism because smaller grain sizes can improve phonon scattering for intrinsically lower lattice thermal conductivity.

1.2. High Temperature Thermoelectric Materials

According to the energy conversion efficiency prediction, the higher the operating temperature, the higher the efficiency. Therefore, high *ZT* materials at high temperatures are strongly desired. This section provides a brief introduction to high temperature TE materials with their properties and *ZT*.

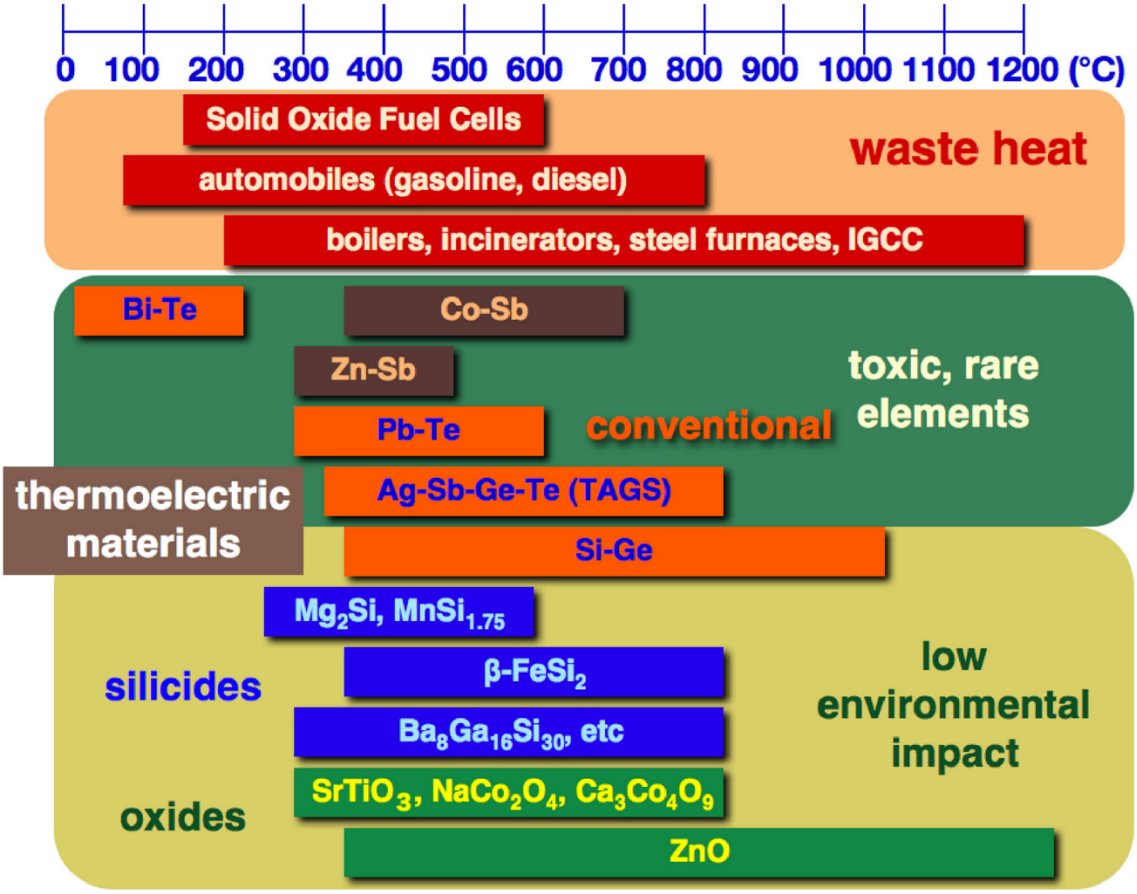

Fig. 6. TE materials classified based on typical waste heat and heat-recovery range [17].

Until the 1990s, conventional TE materials with intermetallic compounds and alloys have been focused heavily dependent on those criteria, which make the heavies elements such as Bi, Te, and Pb the most suited with their corresponding low κ_{lat}. The usage of typical materials are shown that Bi_2Te_3 at room temperature up to 200 °C, PbTe at 300–600 °C, and Si-Ge alloy at

400–1000 °C as shown Fig. 6. The representation in Fig. 6 makes it clear that studies on ZnO, $SrTiO_3$, $Ca_3Co_4O_9$ and other oxide-based systems. The development of the *ZT* of TE bulk materials is shown in Fig. 7, most of which are not practical for industrial purposes because of the poor durability at high temperatures in the air, expensive, low reserves, and often highly toxic.

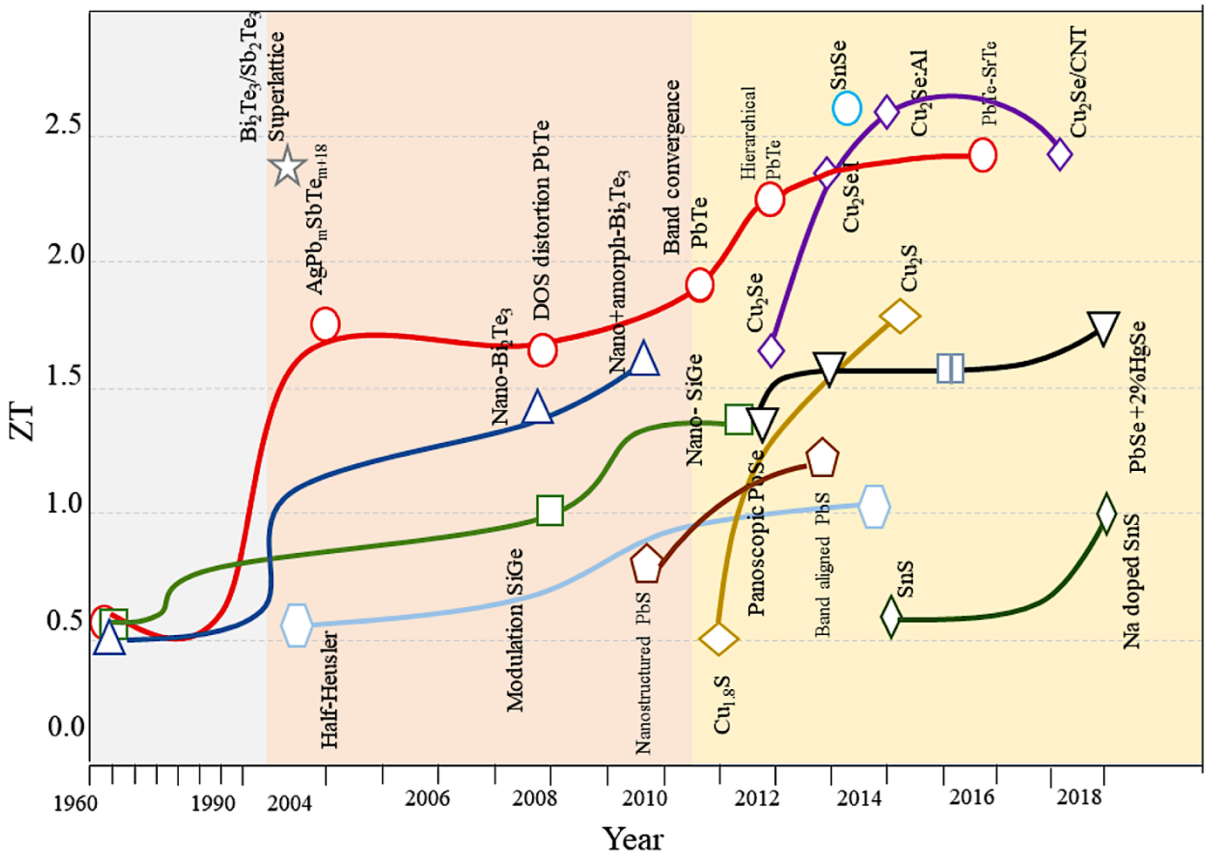

Fig. 7. The development of the maximum *ZT* values of bulk TE materials throughout the past decades [18].

Many new TE materials have been developed outside the existing range of conventional criteria so far. New promising materials have been reported and studied, such as copper and tin chalcogenide, oxide-based materials [19,20], half-Heusler [21], copper sulfides [22], and finally organic polymers [23]. Among these materials, oxides that were not considered suitable

for TE applications in the past. However, due to the development of nanostructurings, the κ value of oxide has decreased significantly, and it is expected that oxide-based materials can be commercialized in thermoelectricity.

1.2.1. Metal Oxide

Metal oxides are binary compounds of oxygen with a metal. The large polarization is also the reason for the highly stable and durability of metal oxide, nevertheless, it is also the origin of low charge mobility and high effective mass, resulting in an overall low *ZT* value. Bandgap manipulation and carrier concentration are often controlled via doping between oxide and donor or acceptor cations. This method also enables the formation of *p*-type and *n*-type TE materials based on each donor or receptor for doping. Furthermore, the manipulation of the carrier concentration through doping is limited by the formation of a compound thermodynamically preferred as a solubility limit of the dopant and a high temperature. Doping effects on the stoichiometry of metal oxides can also cause obstacles. The vibration characteristics of the crystal structure are manipulated and the heat transfer rate is reduced by implementing an additional phonon scattering site. The phonon velocity of a crystal is related to bond energy, force constant, group velocity, and atomic mass. Thus, as with the ideal gas model, the average distance traveled between the two scattering events of the phonon can define the average free path of the phonon. The phonon mean free path is affected by particle boundaries, the scattering of defects, or other phonons. Therefore, this strategy can be used to manipulate phonon speeds and reduce κ_{lat} in order, leading finally increasing the *ZT* value.

1.2.2. *p*-type Metal Oxides

The p-type metal oxides were firstly discovered in the Na_xCoO_2 system and has a similar

structure with layered of cobaltites. Na_xCoO_2 is composed of the alternating stacks of Na^+ plane and CoO_2 plane along with the *c*-axis, with a hexagonal layered crystal structure as shown in Fig. 8. Phonon and electron transports follow different paths in this structure. The electrons and holes are transported by passing through the CdI_2-type CoO_2 layer for *p*-type electronic conduction, while the disordered charge-balancing Na^+ layer is providing the path for phonons. The materials with this kind of layered structure are so-called, phonon glass electronic crystals, which often show high electrical conductivity with low thermal conductivity [24], an ideal material property for TE applications. Therefore, the *p*-type alkali cobalt oxide-based compounds have been recognized as the most promising oxide TE materials [25]. The following graph depicts the different promising TE oxides reported over the years and the development of TE *n* and *p*-type oxides is given in Fig. 9.

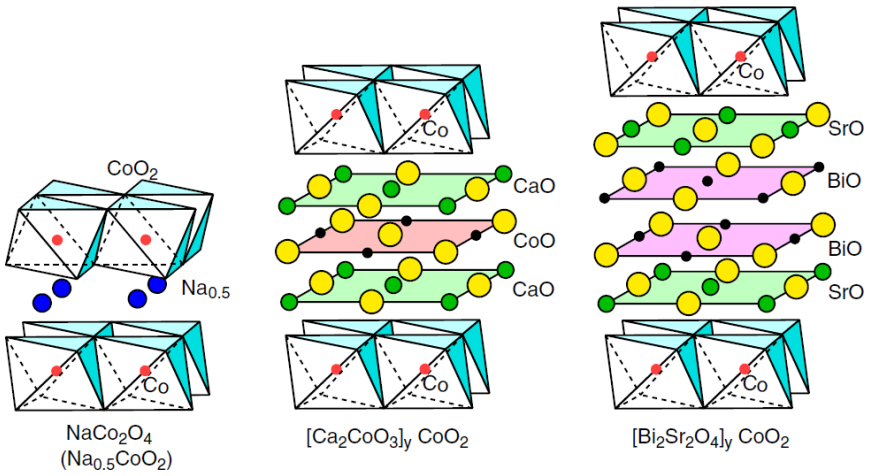

Fig. 8. Crystal structures of layered cobalt oxides [17].

The TE properties of polycrystalline Na_xCoO_2 have been widely investigated with different dopants and doping level of Na_xCoO_2. The amount of Na plays very important role in Na_xCoO_2, forming the disordered phonon glass layers and influencing the phonon scattering and electronic properties. It was found that Ag doping is the most effective because it can improve

the electrical conductivity and the Seebeck coefficient of Na_xCoO_2 simultaneously, resulting in an enhanced *PF* value.

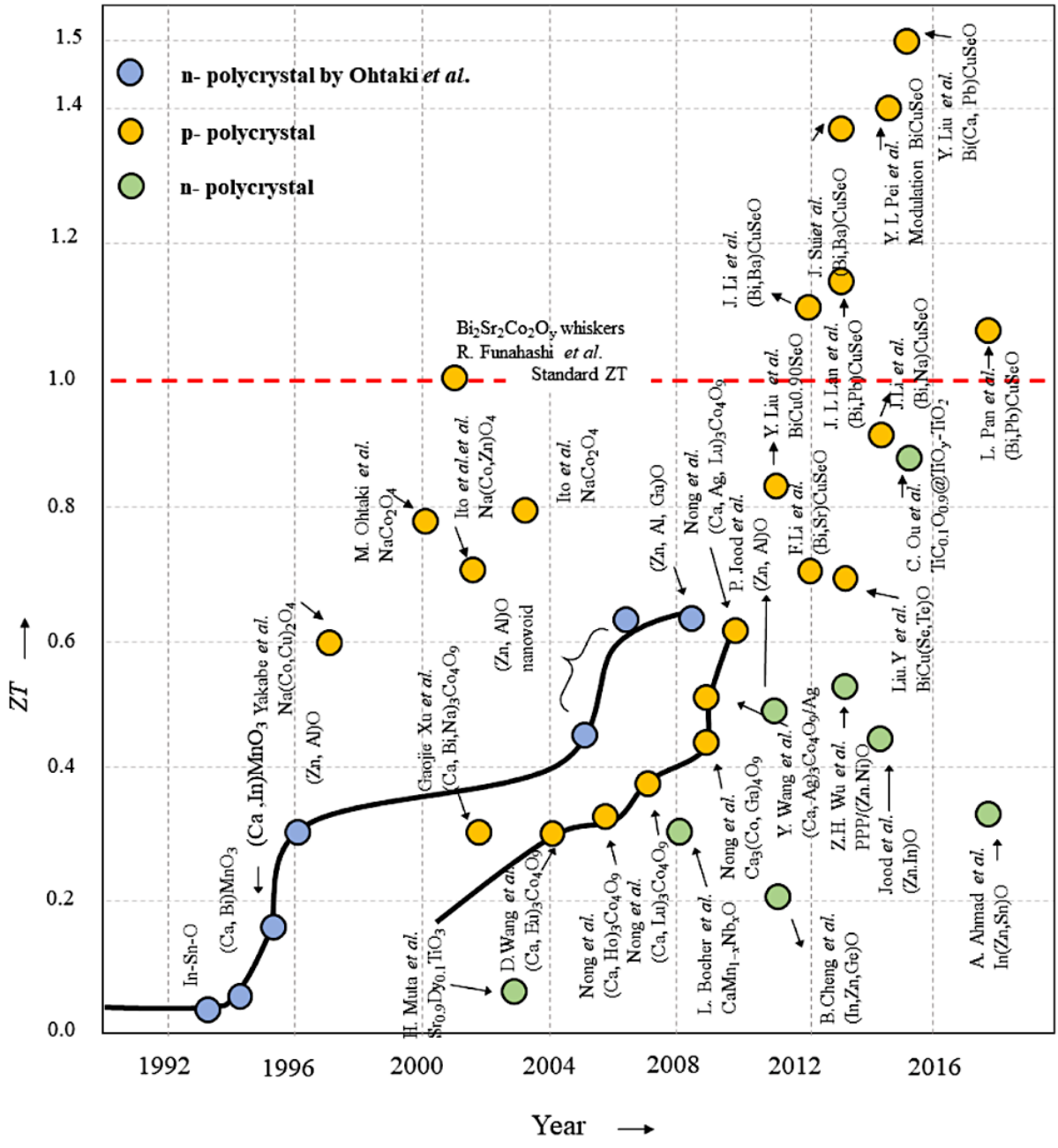

Fig. 9. Representation of the development of thermoelectric oxides over the years [26].

Ag, as a metal-phase dopant, can obviously increase the electrical conductivity, but the mechanism of Ag doping enhancing the Seebeck value is still unclear. It could be caused by

the uniform Ag doping in the samples or the electron-electron correlation. Compared with un-doped $NaCoO_2$, other dopants (Y, Nd, Sr, Sm) have little effects on improving *PF* values, and some dopants (Ni, Yb) even have negative effects [27,28]. Because of the interdependent relations between the Seebeck coefficient and electrical conductivity, these dopants often improve one while they degrade the other. In contrast, doping transition metal elements turn out to be more effective in improving the *PF* of Na_xCoO_2 composites.

1.2.3. *n*-type Metal Oxides

Along with the discovery of *p*-type cobaltites, *n*-type oxide materials are also being developed to suit the unicouple for TE generators. Several promising candidates have been introduced with the most dominant being $SrTiO_3$ based and ZnO-based. Each material has its advantages and disadvantages, which are going to be briefly introduced in the next section.

1.2.3.1. $SrTiO_3$-based Materials

The TE properties of perovskite-type STO have been intensively investigated in the form of single crystals, films, and polycrystalline ceramic bulks. As previously reported [29], *ZT* values can be 0.37 at 1000 K for single-crystals, lower for polycrystalline ceramics, and as high as 2.4 for $SrTiO_3/SrTiO_3$:Nb superlattices [30]. As for the TE practical applications, the performance is still insufficient, and improving their *ZT* values is still a challenge.

STO is a typical perovskite-type oxide with a very high melting point of 2080°C, suggesting the potential of TE applications at high temperatures as shown in Fig. 10. High electrical conductivity σ can be obtained by substitutional doping, e.g. with lanthanides for Sr^{2+} or Nb^{5+} for Ti^{4+}. The thermopower $|S|$ of STO single crystals and $Sr_{1-x}La_xTiO_3$ (x = 0.1–0.5) ceramics was reported, which can be comparable to the TE properties of Na_xCoO_2 [31]. Both STO single crystals and polycrystalline ceramics show a rather heavy DOS effective mass, m^*,

due to the large DOS of the triply degenerate 3d-t_{2g} orbitals at the bottom of the conduction band. The large effective mass results in a large S > 0.1 mV K^{-1} at 300K. In $Sr_{1-x}La_xTiO_3$ (x = 0–0.1) and reduced single crystals, large power factors (1.2–3.6 mW m^{-1} K^{-2} at 300 K) are also observed. However, the thermal conductivity of STO crystals is very high (7–11W m^{-1} K^{-1}) due to strongly bonded lightweight atoms [32] . The further reduction in κ is critical to improve the *ZT* of STO.

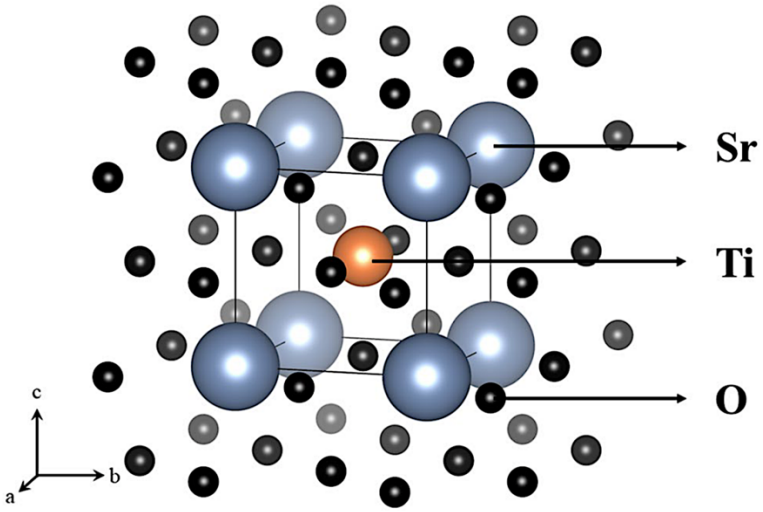

Fig. 10. Crystal structure of STO [26].

Various La dopant concentrations tuned TE properties, and this TE property can significantly change electrical properties and reduce thermal conductivity. Other lanthanide elements can also be used for the enhancement of *ZT* performance. Ti site substitution with Nb ions is another way to improve the TE performance of STO. Wang et al. [33,34] investigated Nb-doped STO composites with second phase and showed that TE performance of the STO can be further enhanced than with only Nb dopant. Ta-doped strontium titanates were studied and their results indicated that 10% Ta-doped sample exhibits the best performance.

1.2.3.2. ZnO-based Oxides

ZnO is an *n*-type wide band-gap semiconductor [19,35,36] having bandgap of 3.37 eV, and has been used extensively for various applications such as UV-light emitters, solar cells, flat panel display, light-emitting devices, piezoelectric transducers, brake linings, cosmetics, dental cements, lubricants, paints, phosphors, and other products due to its low cost, abundance, non-toxicity, and thermal/chemical stability [37–42]. The density of ZnO are 5.61 g cm^{-3} with a very high melting point of 1974°C. Wurtzite structure is the most common structure exhibited by ZnO with a space group of $P6_3mc$ with the lattice parameters *a* and *c* equal to 3.2495 Å and 5.2062 Å as shown in Fig. 11, respectively, and the large piezoelectric constants enable strong piezoelectric polarization in the material, resulting not only in the possibility of piezoelectronic device fabrication but also the fabrication of high quality 2D electron gas structures with the recent observation of fractional quantum Hall effect [43]. From a more chemical point of view, the lattice can be described as two intertwined hexagonal close packed Zn and O lattices, arranged in such a way that each Zn^{2+} ion is coordinated by four O^{2-} ions in a tetrahedral arrangement and likewise, each O^{2-} ion is coordinated by four Zn^{2+} ions in the same way.

Mechanical properties are important parameters for evaluating the practicability of materials, such as hardness, stiffness, piezoelectric constants, Young's and bulk moduli, yield strength. Decremps et al. [44] have studied the pressure behavior of elastic moduli for the wurtzite phase of single-crystal ZnO.

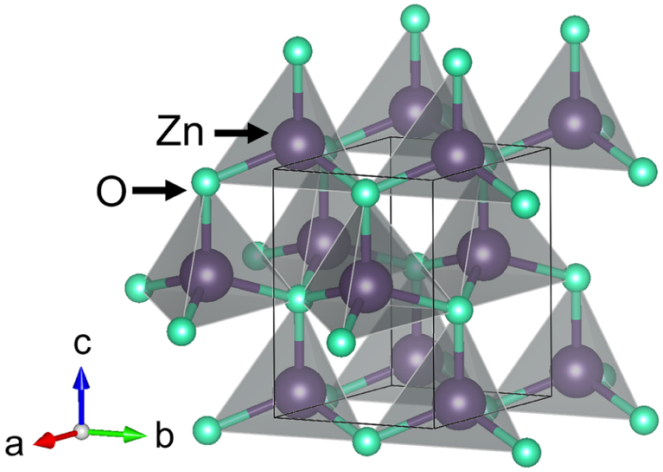

Fig. 11. Crystal structure of ZnO.

M.W. Wolf and Martin investigated the thermal conductivities of large single crystals of zinc oxide from 3.5 to 300 K [45], which suggested that anisotropy in thermal conductivity of ZnO single crystals is very small. As the temperature increased from room temperature to 1000°C, thermal conductivity of a fully sintered polycrystalline sample decreased from 37 to 4 W m^{-1} K^{-1}. Therefore, for the ZnO, the lattice thermal conductivity is the critical factor determining the thermal conductivity.

According to Albrecht et al., the theoretical electron mobility of ZnO is about 300 cm^2 V^{-1} s by Monte Carlo simulations at room temperature [46]. Nominally undoped ZnO with a wurtzite structure naturally becomes an *n*-type semiconductor due to the presence of intrinsic or extrinsic defects. There are major native defects such as the Zn-on-O antisite Zn_O, the Zn interstitial Zn_I,and the O vacancy V_O. However, recently first-principles investigations based on density functional theory suggest that hydrogen in ZnO occurs exclusively in the positive charge state and is responsible for the *n*-type conductivity of ZnO [47].

Elements such as Al, In, Ga, etc. are doped in the ZnO matrix to optimize the wide bandgap of ZnO for applications in the field of solar cells, TE, and optoelectronic applications [48–50]. A high carrier concentration (> 10^{20} cm^{-3}) is exhibited by the group III elements which

makes them ideal dopants. Out of the group III elements, Al has been identified to be the most abundant and also is a shallow donor making it one of the most suitable dopants to increase the *n*-type character. ZnO exhibits a harmonically vibrating lattice as a result of the ionic and covalent nature leading to high thermal conductivity (~ 40 W K^{-1} m^{-1}). Ohtaki in 1996 identified ZnO to be a potential TE material exhibiting a *PF* of 8–15 × 10^{-4} W m^{-1} K^{-2} for Al-doped zinc oxide and leading to *ZT* of 0.3 at 1273 K. Though they possess high thermal conductivity due to the ionic character of ZnO, due to higher carrier mobility and carrier concentration, the electrical conductivity shot up without much decrement in thermopower [35]. Observation of enhancement in thermopower of Al-doped ZnO-based systems was reported by Ohtaki as a result of phonon scattering by the nanovoids—leading to suppressed thermal conductivity [13] to give a *ZT* of 0.55 to 0.57 at 1273 K, thermionic effects due to the nanovoids and suspected carrier energy filtering by the nanovoids to deliver a *ZT* of up to 0.6 at 1250 K [12]. Later, dually doped ZnO (Ga, Al) set a benchmark by exhibiting a *ZT* of 0.65 at 1247 K where Ga acted as the scattering centers to reduce thermal conductivity, whereas Al acted as an agent to increase the carrier mobility which increases the electrical conductivity [19]. More recently, Jood et al. reported a *ZT* of ~ 0.44 for 1000 K that reached thermal conductivity of ~ 2 W K^{-1} m^{-1}. However, further improvements are necessary to obtain better *ZT* values [51].

1.3. Advanced Sintering Technologies

1.3.1. Spark Plasma Sintering (SPS)

In 1906, Bloxam applied for the first patent for the successful consolidation of powder using SPS technology. SPS technology was developed in the early 1960s based on the idea of using plasma in electric discharge equipment that sinter bulk materials. It steadily advanced from the mid-1980s to the 1990s. SPS technology simultaneously applies mechanical pressure and DC pulses, simultaneously sintering in a challenging type that increases density to enable the sintering process [52–60]. The setting of the SPS consists of a graphite die charged with a powder raw material, 50–250 kN, and a uniaxial hydraulic press device that achieves an electric pulse current of low voltage (<10 V) and high current (1–10 kA) [61]. The system achieves a heating rate of 200°C/min or more, the soaking time is only a few minutes, and can be sintered for a very short time. However, one sample can be sintered only once. The particle size of the bulk can be maintained after the SPS process with nano powder. Lan et al. [62] prepared In_2O_3-based ceramics with an average grain size of about 50 nm via SPS; the thermal conductivity of 50 nm grained In_2O_3-based ceramic is only 7.9 W m^{-1} K^{-1}, which is much smaller than that of the 2-μm grained In_2O_3-based ceramic, which is 13.2 W m^{-1} K^{-1}. SPS is not only used for forming and sintering, but also can be used to synthesize materials. Liu et al., [63] prepared BiCuSeO-based ceramics via SPS directly using raw materials such as Bi_2O_3, Bi, Cu, and Se powder mixtures, which immensely shortens the time to prepare bulk ceramics. SPS can be operated under vacuum or inert gas atmosphere at atmospheric pressure with a maximum temperature of 2400°C.

The sintering mechanisms in SPS are a result of three effects, namely, mechanical, thermal and electrical [61]. The fast heating rates achieved in SPS enables densification while retarding microstructure coarsening owing to the short times required to reach sintering temperature. This allows for the densification of nano powders with suppression grain coarsening. The SPS

system offers a number of advantages over the conventional sintering systems such as hot pressing, hot isostatic pressing (HIP) [54,64–66] which include high sintering speeds, high reproducibility, better control of sintering energy and reliability. The mechanism of sintering is not well understood but several authors have postulated a number of theories. The widely accepted SPS sintering mechanisms involve joule heating, plasma generation and electro plastic effect. The electrical effects are a function of the electrical properties of the powders. For powders that are electrically conducting, current can easily flow through, and heat is generated mainly by joule heating and transferred to the bulk of the powder [67] by conduction as depicted in Fig. 12. In the presence of an applied pressure, the electric current through the particles enhances formation of interparticle bonds through localized welding, vaporization or cleaning of powder surfaces. This ensures a smoother and more favorable path for the current flow. This also promotes the production of high-quality sintered compacts at lower temperatures in a shorter time than conventional sintering methods. The sintering of nonconducting powders, although not well understood, is thought to occur through grain boundary migration and matter transport at higher input voltages.

Although the SPS has the capability to sinter at high heating and cooling rates, the expectation is that the system can sinter without appreciable grain-growth. However in reality this is not always the case; a complete avoidance of the grain-growth at the sintering temperatures for most nano-grained materials will always promote grain-growth. It is therefore imperative to adopt an approach/methodology that is more effective in suppressing grain-growth using the SPS system. The two-step sintering (TSS) approach has been found to be effective in suppressing grain-growth of ceramic materials during sintering. It is thus important to dedicate the following section to the success studies on the sintering of functional ceramics to give an insight and a better understanding of the TSS method.

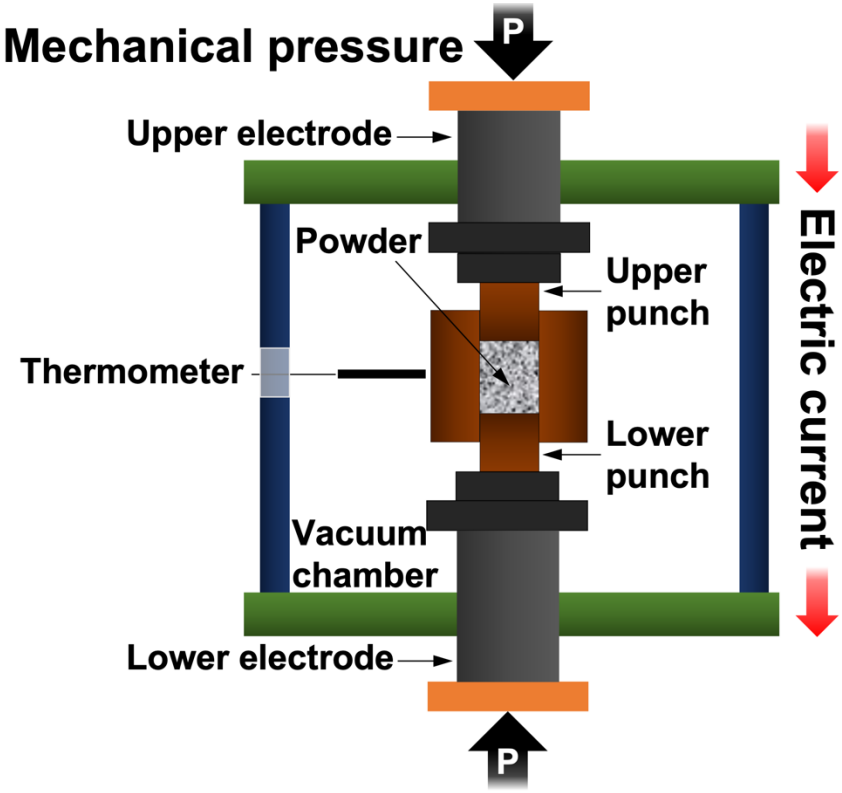

Fig. 12. Schematic diagrams of SPS equipment.

1.3.2. Two-Step Sintering (TSS)

The reliability in ceramic materials is a key function and determines the final performance. Finely controlled microstructures have a greater impact on the properties and reliability of functional ceramic materials. In the previous section, it was found that the development of ceramic with high density nanometric or ultrafine particle size was not easily carried out through conventional sintering. Even though SPS technology has shown excellent potential in the production of high-density nanometric materials, it is hard to maintain microstructural refinement at high sintering temperatures. It should be emphasized that solid phase sintering requires high temperatures to facilitate diffusion that promotes material density. However, the diffusion process promotes grain growth as well as density [68]. Therefore, in order to achieve particle refinement during sintering, it is essential to develop a sintering methodology that only

promotes density without stimulating particle growth. This method has been enhanced over the years to achieve microstructural refinement. The two-stage sintering (TSS) was subsequently introduced by Chu and others in the 1990s [69]. Essentially, the technology consists of two stages: the noble process, the first stage performed at a relatively low temperature, the subsequent high temperature stage, and the subsequent cooling. However, if not properly controlled, the high temperature stage can lead to grain growth. In 2000, Chen and Wang introduced a modified TSS methodology that effectively restrained grain growth accelerated in the second stages [70]. In the modified TSS approach, high temperature heating is first performed for a short time, and then structural cooling and sintering are performed at a low temperature. The concept of heating to a higher temperature (T_1) following rapid cooling without sintering holding time (Fig. 13) is to remove residual porosity at higher temperatures and develop a neck of grain boundary anchoring at triple points.

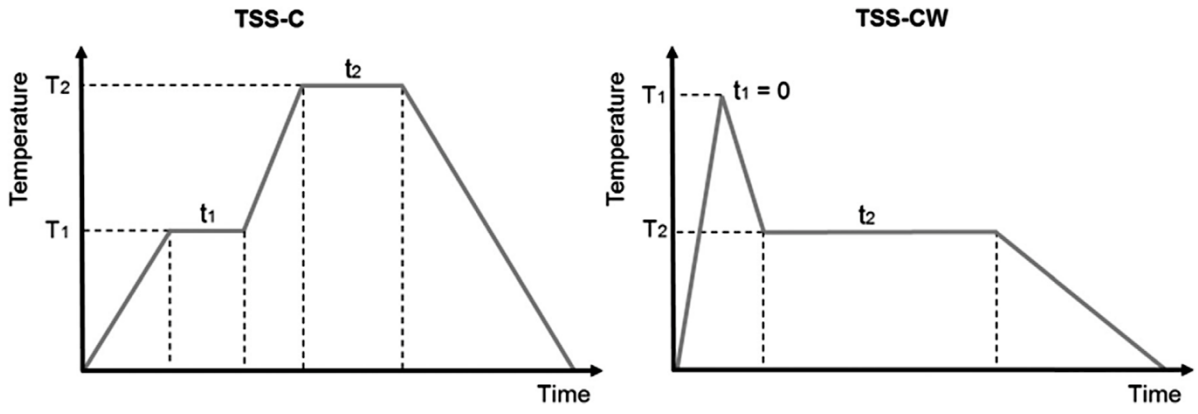

Fig. 13. Illustrative representation of the differences between the two TSS sintering plots [71].

Such pinned triple junctions are considered to have higher activation energy for material movement than the grain boundary. The second step is effectively carried out in microstructure frozen by slow kinetics. A kinetic window separates grain boundary diffusion from grain boundary movement. Grain-growth experienced at intermediate and high temperatures in the

particulate matter is led by very high capillary pressure available in fined-controlled grains. Thermodynamically, the temperature (T_2) is high enough to allow grain boundary diffusion while minimizing grain boundary movement. This promotes density without the growth of particles. However, it is important to select the best (T_2) temperature. If (T_2) is too low, sintering proceeds for a long time until exhaustion occurs, and conversely, if (T_2) is too high, particle growth is likely to occur.

1.4. Motivation and Objectives

To enhance the efficiency of the oxide TE materials as the intermediate and high temperatures applications for energy harvesting with waste heat from the incinerator, this thesis address the doping strategy and TS-SPS process to ZnO-based material. Even though non-doped ZnO is an insulator but it shows metallic behavior by increasing the electrical conductivity with doping. Owing to the feature of ZnO, Al-doped ZnO, In-doped ZnO, and Ga-doped ZnO research has been studied by many groups for the evaluation of TE performance. The most attractive approach to increase the electrical conductivity of ZnO-based TE materials is to dope them with In and Ga due to comparable radii of In^{3+} (0.80 Å), Ga^{3+} (0.62 Å), and Zn^{2+} (0.74 Å). Thus, it is expected that In^{3+} and Ga^{3+} can substitute Zn^{2+} in the ZnO matrix. The main limitation of ZnO as a TE material is its high thermal conductivity. Therefore a strategy can be proposed to lower thermal conductivity, increasing the phonon scattering frequency by reducing the crystal grain size.

In addition, the SPS technique offers an opportunity to produce fine-grained microstructures with suppressed grain-growth due to the uniaxial pressure with direct heating of mold and powder by an electrical current at low temperature. The TSS process has already been proposed for several sintering technologies but a new combination of TSS and SPS (TS-SPS) process has not been studied so far. Therefore, it is expected that optimization of the sintering condition allows suppression of grain-growth and densification for the fine-grained microstructure. Up to now, the contribution of doping to increase electrical conductivity and the control of grain-growth by SPS on the bulk In and Ga dual-doped ZnO has not been investigated.

The main purpose of this study is to improve the TE properties of In and Ga dual-doped ZnO through the investigation of the doping effect in solubility limit to increase electrical conductivity and the control of microstructure to decrease thermal conductivity as a TE

material for the application at the intermediate and high temperatures. Therefore, the solubility limit of In and Ga in ZnO with the highest TE properties was first examined by the detailed crystal structure and microstructural analysis. Secondly, the control of microstructure was accomplished by OS/TS-SPS temperature profiles to improve the TE properties of In doped ZnO ceramics. Accordingly, the fabrication of the ZnO TE materials and the improvement of its TE properties by applying the TS-SPS process can sufficiently prove the originality and value of this study.

This study consists of 2 parts, such as In and Ga dual-doped ZnO TE material with the effect of dopants in chapters 2 and 3, and pure (non-doped) and In-doped ZnO with controlled microstructures by TS-SPS in chapters 4 and 5. The purpose of each chapter is briefly presented below.

In chapter 2, the main purpose is to investigate the TE properties and fabrication of In- and Ga-doped ZnO with various amounts of dopants by SPS. The influence of doping was evaluated through the crystal structure and microstructural analyses to confirm the solubility of dopants and understand their correlations with the TE properties.

In chapter 3, the comparison between the In single, and In and Ga dual doping ZnO ceramics is conducted on their TE performance. Microstructural and chemical composition analyses and TE measurements are conducted to identify the key factors affecting the TE properties of the ceramics.

In chapter 4, the investigation of pure ZnO ceramics by the TS-SPS process under different heating conditions are addressed with a focus on the relative density, grain size, and TE performance.

In chapter 5, the optimization of the TS-SPS processes is focused on different temperature profiles. The investigation on relative density, grain size, and TE performance of the pure/In-doped ZnO ceramics is conducted. Through the temperature profiles, the SPS process achieve

a high critical density and accomplished densification while preventing grain-growth at the first and second heating steps, respectively.

References

[1] G.J. Snyder, E.S. Toberer, Complex thermoelectric materials, Nat. Mater. 7 (2008) 105–114.

[2] L. Yang, Z.G. Chen, M.S. Dargusch, J. Zou, High performance thermoelectric materials: progress and their applications, Adv. Energy Mater. 8 (2018) 1701797.

[3] T.C. Holgate, R. Bennett, T. Hammel, T. Caillat, S. Keyser, B. Sievers, Increasing the efficiency of the multi-mission radioisotope thermoelectric Generator, J. Electron. Mater. 44 (2015) 1814–1821.

[4] M. Rasouli, L.S.J. Phee, Energy sources and their development for application in medical devices, Expert Rev. Med. Devices 7 (2010) 693–709.

[5] E. Romero, R.O. Warrington, M.R. Neuman, Energy scavenging sources for biomedical sensors, Physiol. Meas. 30 (2009) R35–R62.

[6] J. Yang, F.R. Stabler, Automotive applications of thermoelectric materials, J. Electron. Mater. 38 (2009) 1245–1251.

[7] L.E. Bell, Cooling, Heating, Generating power, and recovering waste heat with thermoelectric systems, Science 321 (2008) 1457–1461.

[8] T. Mori, S. Priya, Materials for energy harvesting: at the forefront of a new wave, MRS Bull. 43 (2018) 176–180.

[9] C. Goupil, W. Seifert, K. Zabrocki, E. Müller, G.J. Snyder, Thermodynamics of thermoelectric phenomena and applications, Entropy 13 (2011) 1481–1517.

[10] G.J. Snyder, A.H. Snyder, Figure of merit ZT of a thermoelectric device defined from materials properties, Energy Environ. Sci. 10 (2017) 2280–2283.

[11] H.S. Kim, S. Il Kim, K.H. Lee, S.W. Kim, G.J. Snyder, Phonon scattering by dislocations at grain boundaries in polycrystalline $Bi_{0.5}Sb_{1.5}Te_3$, Phys. Status Solidi B. 254 (2017) 1600103.

[12] M. Ohtaki, R. Hayashi, Enhanced thermoelectric performance of nanostructured ZnO: a possibility of selective phonon scattering, 25th Int. Conf. Thermoelectr. (2006) 276–279.

[13] M. Ohtaki, K. Araki, Thermoelectric properties and thermopower enhancement of Al-doped ZnO with nanosized pore structure, J. Ceram. Soc. Jpn. 119 (2011) 813–816.

[14] B.K. Jang, Y. Sakka, Thermophysical properties of porous SiC ceramics fabricated by pressureless sintering, Sci. Technol. Adv. Mater. 8 (2007) 655–659.

[15] L. Han, N. V. Nong, W. Zhang, L.T. Hung, T. Holgate, K. Tashiro, M. Ohtaki, N. Pryds, S. Linderoth, Effects of morphology on the thermoelectric properties of Al-doped ZnO, RSC Adv. 4 (2014) 12353–12361.

[16] B.K. Jang, Y. Sakka, Influence of microstructure on the thermophysical properties of sintered SiC ceramics, J. Alloys Compd. 463 (2008) 493–497.

[17] M. Ohtaki, Recent aspects of oxide thermoelectric materials for power generation from mid-to-high temperature heat source, J. Ceram. Soc. Jpn. 119 (2011) 770–775.

[18] X. Zhang, L.D. Zhao, Thermoelectric materials: energy conversion between heat and electricity, J. Materiomics 1 (2015) 92–105.

[19] M. Ohtaki, K. Araki, K. Yamamoto, High thermoelectric performance of dually doped ZnO ceramics, J. Electron. Mater. 38 (2009) 1234–1238.

[20] G. Ren, J. Lan, C. Zeng, Y. Liu, B. Zhan, S. Butt, Y.H. Lin, C.W. Nan, High performance oxides-based thermoelectric materials, Jom. 67 (2014) 211–221.

[21] W.G. Zeier, J. Schmitt, G. Hautier, U. Aydemir, Z.M. Gibbs, C. Felser, G.J. Snyder, Engineering half-Heusler thermoelectric materials using Zintl chemistry, Nat. Rev. Mater. 1 (2016) 16032.

[22] K K. Suekuni, H. Usui, S. Qiao, K. Hashikuni, T. Hirano, H. Nishiate, C.H. Lee, K. Kuroki, K. Watanabe, M. Ohtaki, Electronic structure and thermoelectric properties of $Sn_{1.2-x}Nb_xTi_{0.8}S_3$ with a quasi-one-dimensional structure, J. Appl. Phys. 125 (2019)

175111.

[23] G. Chen, W. Xu, D. Zhu, Recent advances in organic polymer thermoelectric composites, J. Mater. Chem. C. 5 (2017) 4350–4360.

[24] A. Nag, V. Shubha, Oxide thermoelectric materials: A structure-property relationship, J. Electron. Mater. 43 (2014) 962–977.

[25] Q. Li, Z. Lin, J. Zhou, Thermoelectric materials with potential high power factors for electricity generation, J. Electron. Mater. 38 (2009) 1268–1272.

[26] R. Prasad, S.D. Bhame, Review on texturization effects in thermoelectric oxides, Mater. Renew. Sustain. Energy. 9 (2020) 3.

[27] L. Wang, M. Wang, D. Zhao, Thermoelectric properties of c-axis oriented Ni-substituted $NaCoO_2$ thermoelectric oxide by the citric acid complex method, J. Alloys Compd. 471 (2009) 519–523.

[28] T. Nagira, M. Ito, S. Katsuyama, K. Majima, H. Nagai, Thermoelectric properties of $(Na_{1-y}M_y)_xCo_2O_4$ (M = K, Sr, Y, Nd, Sm and Yb; Y = 0.01 ~ 0.35), J. Alloys Compd. 348 (2003) 263–269.

[29] S. Ohta, T. Nomura, H. Ohta, M. Hirano, H. Hosono, K. Koumoto, Large thermoelectric performance of heavily Nb-doped $SrTiO_3$ epitaxial film at high temperature, Appl. Phys. Lett. 87 (2005) 092108.

[30] H. Ohta, S. Kim, Y. Mune, T. Mizoguchi, K. Nomura, S. Ohta, T. Nomura, Y. Nakanishi, Y. Ikuhara, M. Hirano, H. Hosono, K. Koumoto, Giant thermoelectric Seebeck coefficient of a two-dimensional electron gas in $SrTiO_3$, Nat. Mater. 6 (2007) 129–134.

[31] I. Terasaki, Y. Sasago, K. Uchinokura, Large thermoelectric power in single crystals, Phys. Rev. B Condens. Matter. 56 (1997) R12685–R12687.

[32] H. Muta, K. Kurosaki, S. Yamanaka, Thermoelectric properties of reduced and La-doped single-crystalline $SrTiO_3$, J. Alloys Compd. 392 (2005) 306–309.

[33] N. Wang, L. Han, H. He, Y. Ba, K. Koumoto, Effects of mesoporous silica addition on thermoelectric properties of Nb-doped $SrTiO_3$, J. Alloys Compd. 497 (2010) 308–311.

[34] N. Wang, H. Chen, H. He, W. Norimatsu, M. Kusunoki, K. Koumoto, Enhanced thermoelectric performance of Nb-doped $SrTiO_3$ by nano-inclusion with low thermal conductivity, Sci. Rep. 3 (2013) 3449.

[35] M. Ohtaki, T. Tsubota, K. Eguchi, H. Arai, High-temperature thermoelectric properties of $(Zn_{1-x}Al_x)O$, J. Appl. Phys. 79 (1996) 1816–1818.

[36] T. Tsubota, M. Ohtaki, K. Eguchi, H. Arai, Thermoelectric properties of Al-doped ZnO as a promising oxide material for high-temperature thermoelectric conversion, J. Mater. Chem. 7 (1997) 85–90.

[37] M.H. Huang, S. Mao, H. Feick, H. Yan, Y. Wu, H. Kind, E. Weber, R. Russo, P. Yang, Room-temperature ultraviolet nanowire nanolasers, Science 292 (2001) 1897–1899.

[38] D.C. Look, Progress in ZnO materials and devices, J. Electron. Mater. 35 (2006) 1299–1305.

[39] C.F. Klingshirn, ZnO: Material, physics and applications, ChemPhysChem. 8 (2007) 782–803.

[40] P. Durán, J. Tartaj, C. Moure, Fully dense, fine-grained, doped zinc oxide varistors with improved nonlinear properties by thermal processing optimization, J. Am. Ceram. Soc. 86 (2003) 1326–1329.

[41] F. Giovannelli, A. Ngo Ndimba, P. Diaz-Chao, M. Motelica-Heino, P.I. Raynal, C. Autret, F. Delorme, Synthesis of Al doped ZnO nanoparticles by aqueous coprecipitation, Powder Technol. 262 (2014) 203–208.

[42] S. Liu, G. Li, M. Lan, M. Zhu, T. Mori, Q. Wang, Improvement of thermoelectric properties of evaporated ZnO:Al Films by CNT and Au nanocomposites, J. Phys. Chem. C. 124 (2020) 12713–12722.

[43] H.Y. Hwang, Y. Iwasa, M. Kawasaki, B. Keimer, N. Nagaosa, Y. Tokura, Emergent phenomena at oxide interfaces, Nat. Mater. 11 (2012) 103–113.

[44] F. Decremps, J. Zhang, B. Li, R.C. Liebermann, Pressure-induced softening of shear modes in ZnO, Phys. Rev. B. 63 (2001) 2241051.

[45] M.W. Wolf, J.J. Martin, Low temperature thermal conductivity of zinc oxide, Phys. Status Solidi. 17 (1973) 215–220.

[46] J.D. Albrecht, P.P. Ruden, S. Limpijumnong, W.R.L. Lambrecht, K.F. Brennan, High field electron transport properties of bulk ZnO, J. Appl. Phys. 86 (1999) 6864–6867.

[47] C.G. Van De Walle, Hydrogen as a cause of doping in zinc oxide, Phys. Rev. Lett. 85 (2000) 1012–1015.

[48] T. Ogi, D. Hidayat, F. Iskandar, A. Purwanto, K. Okuyama, Direct synthesis of highly crystalline transparent conducting oxide nanoparticles by low pressure spray pyrolysis, Adv. Powder Technol. 20 (2009) 203–209.

[49] J.N. Hasnidawani, H.N. Azlina, H. Norita, N.N. Bonnia, S. Ratim, E.S. Ali, Synthesis of ZnO Nanostructures using sol-gel method, Procedia Chem. 19 (2016) 211–216.

[50] H. Serier, M. Gaudon, M. Ménétrier, Al-doped ZnO powdered materials: Al solubility limit and IR absorption properties, Solid State Sci. 11 (2009) 1192–1197.

[51] P. Jood, R.J. Mehta, Y. Zhang, G. Peleckis, X. Wang, R.W. Siegel, T. Borca-Tasciuc, S.X. Dou, G. Ramanath, Al-doped zinc oxide nanocomposites with enhanced thermoelectric properties, Nano Lett. 11 (2011) 4337–4342.

[52] M. Tokita, Recent and future progress on advanced ceramics sintering by spark plasma sintering, Nanotechnol Russ. 10 (2015) 261–267.

[53] T. Mori, Novel principles and nanostructuring methods for enhanced thermoelectrics, Small. 13 (2017) 1702013.

[54] P.M. Radingoana, S. Guillemet-Fritsch, P.A. Olubambi, G. Chevallier, C. Estournès,

Influence of processing parameters on the densification and the microstructure of pure zinc oxide ceramics prepared by spark plasma sintering, Ceram. Int. 45 (2019) 10035–10043.

[55] P.M. Radingoana, S. Guillemet-Fritsch, J. Noudem, P.A. Olubambi, G. Chevallier, C. Estournès, Thermoelectric properties of ZnO ceramics densified through spark plasma sintering, Ceram. Int. 46 (2020) 5229–5238.

[56] Z. Shen, M. Johnsson, Z. Zhao, M. Nygren, Spark plasma sintering of alumina, J. Am. Ceram. Soc. 85 (2002) 1921–1927.

[57] S. Grasso, C. Hu, G. Maizza, B.N. Kim, Y. Sakka, Effects of pressure application method on transparency of spark plasma sintered alumina, J. Am. Ceram. Soc. 94 (2011) 1405–1409.

[58] B.K. Jang, S. Kim, Y.S. Oh, H.T. Kim, Y. Sakka, H. Murakami, Influence of La_2O_3 addition on thermophysical properties of ZrO_2-4 mol%Y_2O_3 ceramics fabricated by spark plasma sintering, J. Ceram. Soc. Jpn. 119 (2011) 929–932.

[59] B.K. Jang, S. Kim, Y.S. Oh, H.T. Kim, Y. Sakka, H. Murakami, Effect of Gd_2O_3 on the thermal conductivity of ZrO_2-4 mol.% Y_2O_3 ceramics fabricated by spark plasma sintering, Scr. Mater. 69 (2013) 165–170.

[60] A. Jeong, M. Ohtaki, B.K. Jang, Characterization of ZnO thermoelectric ceramics and their microstructures consolidated by two-step spark plasma sintering, J. Ceram. Soc. Jpn. 130 (2022) 889–894.

[61] W. Matizamhuka, Spark plasma sintering (SPS) – an advanced sintering technique for structural nanocomposite materials, J. South. African Inst. Min. Metall. 116 (2016) 1171–1180.

[62] J. Lan, Y.H. Lin, Y. Liu, S. Xu, C.W. Nan, High thermoelectric performance of nanostructured in_2O_3-based ceramics, J. Am. Ceram. Soc. 95 (2012) 2465–2469.

[63] Y.C. Liu, J. Le Lan, B. Zhan, J. Ding, Y. Liu, Y.H. Lin, B. Zhang, C.W. Nan, Thermoelectric properties of Pb-doped BiCuSeO ceramics, J. Am. Ceram. Soc. 96 (2013) 2710–2713.

[64] S. Hirano, S. Isobe, T. Tani, N. Kitamura, I. Matsubara, K. Koumoto, Electrical and thermal transport properties in layer-structured $(ZnO)_mIn_2O_3$ (m = 5 and 9) ceramics, Jpn. J. Appl. Phys. 41 (2002) 6430–6435.

[65] M. Mazaheri, A.M. Zahedi, M. Haghighatzadeh, S.K. Sadrnezhaad, Sintering of titania nanoceramic: densification and grain growth, Ceram. Int. 35 (2009) 685–691.

[66] M. Gao, H. Zhang, Y. Xie, L. Miao, W. Yao, F. Zhang, T. Wang, H. Zhang, Characteristics of ultra-high density Al:ZnO sputtering targets prepared by hot isostatic pressing, Ceram. Int. 44 (2018) 5486–5491.

[67] O. Guillon, J. Gonzalez-Julian, B. Dargatz, T. Kessel, G. Schierning, J. Räthel, M. Herrmann, Field-assisted sintering technology/spark plasma sintering: mechanisms, materials, and technology developments, Adv. Eng. Mater. 16 (2014) 830–849.

[68] I.W. Chen, X.H. Wang, Sintering dense nanocrystalline ceramics without final-stage grain growth, Nature. 404 (2000) 168–171.

[69] M.Y. Chu, L.C. De Jonghe, M.K.F. Lin, F.J.T. Lin, Precoarsening to improve microstructure and sintering of powder compacts, J. Am. Ceram. Soc. 74 (1991) 2902–2911.

[70] X.H. Wang, P.L. Chen, I.W. Chen, Two-step sintering of ceramics with constant grain-size, I. Y_2O_3, J. Am. Ceram. Soc. 89 (2006) 431–437.

[71] N.J. Lóh, L. Simão, C.A. Faller, A. De Noni, O.R.K. Montedo, A review of two-step sintering for ceramics, Ceram. Int. 42 (2016) 12556–12572.

Chapter 2. Thermoelectric Properties of In- and Ga-doped Spark Plasma Sintered ZnO Ceramics

2.1. Introduction

The demand for renewable energy resources is increasing owing to global warming and the depletion of fossil fuels, and the development of alternative energy sources is crucial [1]. For this reason, thermoelectric (TE) energy conversion has received considerable attention as a potential candidate for power generation from renewable and unused energy sources. TE devices have a substantial advantage in that many heat sources can be used without air pollution or excessive energy consumption [2]. The conversion efficiency of TE materials is generally determined by a dimensionless figure of merit (ZT): $ZT = S^2\sigma T\kappa^{-1}$, where S, σ, T, and κ are the Seebeck coefficient, electrical conductivity, absolute temperature, and thermal conductivity (which is composed of the electron (κ_{el}) and lattice (κ_{lat}) thermal conductivities), respectively. For a high ZT, a high Seebeck coefficient, high electrical conductivity, and low thermal conductivity are required. However, it is difficult to improve ZT because TE materials entail a trade-off relationship between the Seebeck coefficient and electrical conductivity. Hence, it is necessary to optimize multiple factors, including the Seebeck coefficient, electrical conductivity, and thermal conductivity, simultaneously to enhance the ZT of TE materials.

ZnO-based TE oxides, such as Al-doped ZnO, In-doped ZnO, and Ga-doped ZnO [3,4–6], have attracted considerable attention for use at high temperatures. The main limitation of ZnO as a TE material is its high thermal conductivity [7]. Therefore, some strategies, such as increasing the frequency of phonon scattering by reducing the crystal grain size, have been proposed to reduce the thermal conductivity. Other strategies include ceramic texturing with a maximum ZT value of 0.23 achieved at 1053 K [8], generating a new crystal structure type, including the homologous series $Ga_2O_3(ZnO)_m$ [9,10], and tuning the porosity [11,12]. The

most attractive method for reducing the thermal conductivity is doping elements such as Al, In, and Ga into the ZnO matrix. Although In- and Ga-doped ZnO thin films are well studied [13], there is little research on bulk In- and Ga-doped ZnO [14,15]. The miscibility of dopant and ZnO was very low. In addition, excessive dopant content inevitably leads to secondary phases, which can worsen carrier transport properties. Accordingly, using one smaller and the other larger dual dopant than Zn ion can be a promising method for efficiently adjusting crystal quality along with electrical conductivity and controlling thermoelectric properties [13]. The contributions of doping with In and Ga [14], which are heavier group 13 elements [6], to the reduction in the thermal conductivity of ZnO have not been investigated fully; thus, there remains a lack of understanding of the correlation between the doping effects of In and Ga and the TE characteristics.

Herein, we focus on the fabrication of In- and Ga-doped ZnO by a solid-state reaction method and spark plasma sintering (SPS) owing to advancements in sintering techniques that enhance fine grains and achieve fully densified microstructures by suppressing grain-growth [16–19]. Moreover, under the vacuum and carbon-rich environment of SPS, an oxygen reduction reaction can occur, which may create oxygen vacancies. Phonon propagation with a low or high number of oxygen vacancies can reduce the thermal conductivity.

The purpose of the present study is to investigate the TE properties and fabrication of In- and Ga-doped ZnO with various amounts of dopants by SPS. The influence of doping was evaluated through crystal structure and microstructural analyses to confirm the solubility of dopants and understand their correlations with the TE properties.

2.2. Experimental Procedures

$[Zn_{(1-x-y)}Ga_xIn_y]O$ (x = 0, 0.02; y = 0, 0.005, 0.01, 0.02) powders were synthesized by a solid-state reaction method using ZnO, Ga_2O_3, and In_2O_3. Pure ZnO and ZnO–Ga_2O_3–In_2O_3 (Zn–Ga–In–O) were fabricated, and the amount of Ga was consistently x = 0.02 with a variable amount of In. ZnO, Ga_2O_3, and In_2O_3 (99.99%, Sigma-Aldrich Co. LLC., USA) were used as starting materials, weighed according to the target elemental compositions, and then mixed by planetary ball milling (Pulverisette 6, Fritsch GmbH, Germany) to produce small-sized particles using 40 g of zirconia beads (Ø = 5 mm) at a rotational speed of 100 rpm for 50 cycles of 30 s with a 2 min pause to ensure that no component became stuck to the grinding jar. The mixed powders were sifted with a 250 μm mesh. The mixtures were then molded into pellets by applying a uniaxial pressure of 100 MPa, and the pellets were placed in an alumina container. The first calcination was conducted at 1373 K with a heating rate of 100 K h^{-1}; this temperature was maintained for 24 h, and then the specimen was cooled to room temperature over a period of 11 h under an air atmosphere. After the first calcination, the pellets were thoroughly pulverized in an agate mortar, pressed, and calcinated again for an additional 24 h at 1373 K to improve the homogeneity of the specimens. Subsequently, the pellets were reground and loaded into a graphite die with an inner diameter of 10 mm. SPS was expected to suppress grain-growth [19] to achieve small particle sizes to decrease the mean free path of phonons for a low thermal conductivity, and it was a different sintering technique compared with those in reported research [14,15]. For SPS densification, the die was placed in the SPS machine (PLASMAN CSP-I-03121, S. S. Alloy, Japan). The vacuum chamber was evacuated to ≤ 35 Pa, and the specimen was heated to 1423 K at a heating rate of 100 K min^{-1} under a uniaxial pressure of 50 MPa with a holding time of 15 min. The pressure was released from 50 to 14 MPa after the holding time, and the specimen was cooled to room temperature at a cooling rate of 20 K min^{-1}. After densification, the pellet was separated from the graphite die and polished

using SiC sandpaper to remove all possible carbon contamination from the pellet surface.

The crystallographic structure and phase purity of the specimens were examined by powder X-ray diffraction (XRD) using an X-ray diffractometer (MiniFlex600, Rigaku, Japan) with a Cu Kα radiation (λ = 1.5406 Å) source within the range $20° \leq 2\theta \leq 80°$ at a scanning step and speed of 0.01° and 10° min^{-1}, respectively; the operating voltage and current were 40 kV and 15 mA, respectively. The crystal structure was refined using the Rietveld method. Scanning electron microscopy (SEM) was performed to observe the surface morphologies and chemical compositions of the mirror-polished specimens using a JCM-6000Plus NeoScope (JEOL, Japan) microscope equipped for energy-dispersive X-ray spectrometer (EDS).

Highly dense specimens were cut into bars (2.5 × 2.5 × 8 mm^3 for TE property measurements) and squares (5 × 5 × 1 mm^3 for thermal conductivity measurements) along the same direction, parallel (//) to the sintering pressing axis owing to the anisotropic properties [20], and polished with SiC sandpaper. The electrical conductivity (σ) and Seebeck coefficient (S) were measured simultaneously under an air atmosphere using the four-probe DC method and temperature differential method (RZ2001i, Ozawa Science, Japan), which do not have a reduction source. The thermal conductivity (κ) was determined from the thermal diffusivity (α) and heat capacity (C_p), which were measured simultaneously using a laser-flash method (LFA-502, Kyoto Electronics Manufacturing, Japan) under vacuum conditions at 373–1073 K. The absolute values of C_p were obtained using a comparative method with molybdenum as a reference. The thermal conductivity was calculated using the definition $\kappa = \alpha C_p \rho$, where ρ is the density of the specimen.

2.3. Results and Discussion

2.3.1. Crystal Structure Analysis of In- and Ga-doped ZnO

The most common structure in ZnO crystals is the wurtzite structure in the space group of *P*6$_3$*mc* (186), as shown in Fig. 14. A view of ZnO along the c-axis is shown in Fig. 14(b), which shows the hexagonal structure simulated using VESTA software [21]. The purple spheres represent zinc atoms, and the cyan spheres represent oxygen atoms. In the lattice, each Zn^{2+} ion is coordinated by four O^{2-} ions in a tetrahedral arrangement, and each O^{2-} ion is coordinated by four Zn^{2+} ions in the same way.

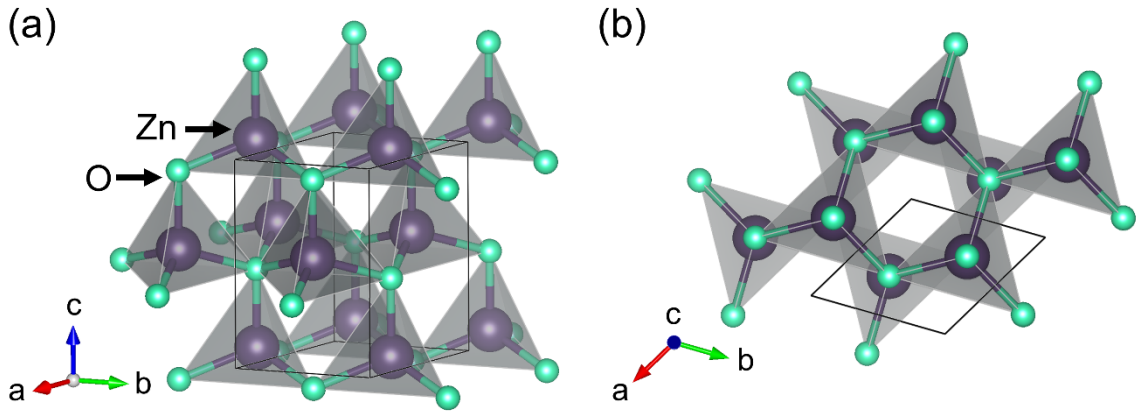

Fig. 14. (a) Wurtzite crystal structure of ZnO and (b) view of ZnO along the c-axis with the unit cell. Wyckoff positions for the space group *P*6$_3$*mc* (186) are described.

The crystal structure of the SPSed specimens at 1423 K was examined using XRD, as shown in Fig. 15. The XRD peaks of pure ZnO were indexed to the wurtzite structure of ZnO based on the Inorganic Crystal Structure Database (ICSD), as shown in Fig. 15(a). The diffraction patterns of $[Zn_{(1-x-y)}Ga_xIn_y]O$ (x = 0.02; y = 0, 0.005, 0.01, 0.02) show that the primary phase was the wurtzite structure of ZnO. The sharp and narrow peak intensities

indicate that the specimens had good crystallinity and a fine grain size. The $[Zn_{(1-x-y)}Ga_xIn_y]O$ specimens were indexed with y = 0, indicating that they contained a secondary spinel phase of $ZnGa_2O_4$ (2θ = 35.70°), as shown in Fig. 15(b). The secondary phase ($ZnGa_2O_4$) started to disappear in the range y = 0.005–0.02, as shown in Fig. 15(c)–15(e). There were no secondary phase peaks other than those of the $ZnGa_2O_4$ spinel structure for any of the specimens, and the peak positions and relative intensities of the patterns agreed with those of the ZnO pattern. One of the meanings of the peak shift in XRD analysis is a change in the d-spacing, which can be calculated using Bragg's law:

$$n\lambda = 2d \sin\theta \qquad (1)$$

where n is an integer, λ is the wavelength of the electrons, and d is the spacing of the crystal planes. It is expected that the peaks will shift to higher angles because the d-spacing of the specimens will decrease owing to doping with In and Ga. If well-doped specimens could be obtained, it is expected that the XRD peaks of specimens with y = 0, 0.005, 0.01, and 0.02 will shift to higher angles, but the XRD results showed a shift to lower angles from the substitution of In^{3+} (0.80 Å, coordination VI) and Ga^{3+} (0.62 Å, coordination VI) into the position of Zn^{2+} (0.74 Å, coordination VI) (values are ion radii) [22,21], which indicates that the doping process was insufficient. Although the XRD results of In- and Ga-doped ZnO did not exhibit a shift to higher angles, the doping effect of In and Ga was confirmed by EDS point analysis, which will be discussed in the next section.

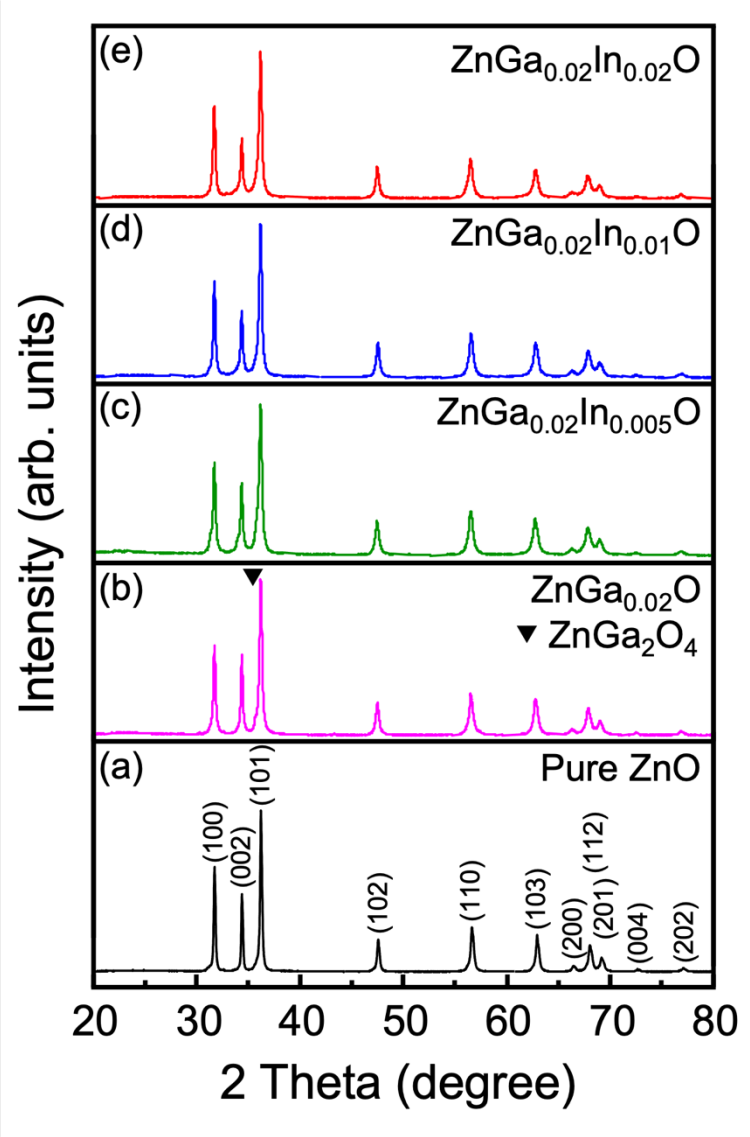

Fig. 15. XRD patterns of examined SPSed (a) pure ZnO and (b)–(e) $[Zn_{(1-x-y)}Ga_xIn_y]O$ (x = 0.02); (b) y = 0, (c) y = 0.005, (d) y = 0.01, and (e) y = 0.02.

2.3.2. Microstructural Analysis

The microstructure and various phases of the SPSed $[Zn_{(1-x-y)}Ga_xIn_y]O$ (x = 0.02; y = 0, 0.005, 0.01, 0.02) are shown in the backscattered electron (BSE) images presented in Fig. 16. In addition, Fig. 16 shows the existence of the primary phase (ZnO) and secondary phases of $ZnGa_2O_4$ or intermediate compounds of Zn–Ga–In–O with a dense morphology. Although pure ZnO exhibited a lower relative density of 91.3% compared with those of the In- and Ga-doped

specimens, all the specimens showed a high relative density of ≥ 97.3% of the theoretical density of ZnO ($\rho \approx 5.61$ g cm^{-3}), as listed in Table 1.

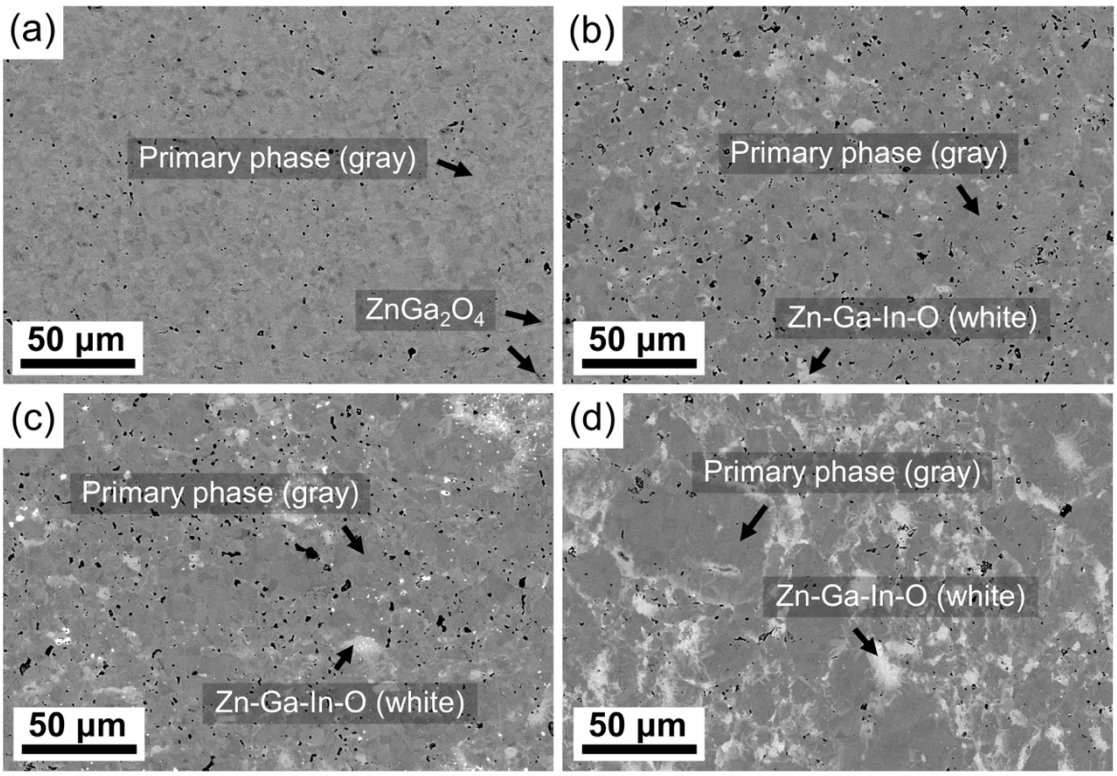

Fig. 16. BSE images of SPSed $[Zn_{(1-x-y)}Ga_xIn_y]O$ (x = 0.02); (a) y = 0, (b) y = 0.005, (c) y = 0.01, and (d) y = 0.02. The white area is composed of Zn–Ga–In–O with a high amount of In.

Table 1. Relative density of SPSed pure ZnO and $[Zn_{(1-x-y)}Ga_xIn_y]O$ with various compositions.

Material	Relative density (%)
Pure ZnO	91.3
x = 0.02, y = 0	99.7
x = 0.02, y = 0.005	97.3
x = 0.02, y = 0.01	98.2
x = 0.02, y = 0.02	99.5

The high relative density of In- and Ga-doped ZnO reached 97.3–99.5% in the present work in comparison with the low relative density (79.8–91.0%) of In- and Ga-doped ZnO from previously reported results [14]. The improvement in the relative density can be elucidated through previous research that obtained dense ZnO by reducing the sintering temperature [24]. It was reported that an Al-doped ZnO specimen sintered at 773 K had a considerably higher relative density (90–96%), while pure ZnO sintered at 873 K had a low relative density (65%). The increase in the relative density indicates that Al doping decreases the sintering temperature required to achieve dense ZnO.

There are many factors in the sintering temperature of ceramics. Theoretically, these parameters can be divided into two categories [25]:

(i) Intrinsic: they specify essential properties of sintered material such as surface free energy, diffusion coefficient, vapor pressure, viscosity, and so on. These parameters vary depending on the chemical composition, ambient atmosphere, or temperature change.

(ii) Extrinsic: it varies depending on the geometric or topological details of the entire sintering system. These include average particle size, size distribution, green body density, and particle morphology.

To reduce sintering temperatures, sintering under pressure and adding sintering additives can be chosen [25,26]. In the case of the sintering under pressure, the driving force for sintering is increased, and a higher density can usually be obtained at a lower sintering temperature. Also, an increased driving force is generated by a local increase in the free energy of the material in a high stress region where the particles come into contact. The sintering driving force is determined by the differences in bulk pressure, vacancy concentration, and vapor pressure. There are mechanisms of mass transport in bulk, which are plastic flow, volume diffusion, and grain boundary diffusion [27]. In the case of the sintering additives, many types of sintering aids have been accepted and listed in Table 2. Sintering additives are usually used to enhance

the sinterability and called dopants are usually called when their concentration is low, and it forms point defect, being capable to decrease sintering temperature [27]. Li- and In-doped ZnO has been studied on the synergetic effect of different dopants on sintering [28]. Li- and In-doped ZnO were shown to have the greatest sinterability among pure, Li-doped, In-doped ZnO, and mixtures. These results are described in consideration of the electrostatic field by electronic rearrangement between the In-doped ZnO with a high Fermi level and the Li-doped ZnO with a low Fermi level. It is considered that this electrostatic field contacts well between particles of two oxides and improves the sintering of doped ZnO. In addition, the sintering rate of In-doped ZnO was found to be faster than pure ZnO, which seems to have improved the sintering rate due to the high surface energy by the roughness that arose from the secondary (compounds) phase. Therefore, the increased relative density according to the In addition amount in In- and Ga-doped ZnO (Table 1) can be explained as an enhancement in sinterability by electrostatic fields of two different dopants and an improvement in sintering speed due to the high surface energy from intermediate compounds (Zn–Ga–In–O) by increasing In amount. Therefore, it is assumed that In and Ga play the role of sintering additives in ZnO for densification.

Table 2. Sintering aids and grain-growth inhibitors (revised from [25]).

Materials	Sintering aids	Grain-growth inhibitors
ZnO	Li_2O, In_2O_3, PbO [28,29]	K_2O, Sb_2O_3 [30]
Al_2O_3	LiF	Mg, Zn, Ni, W, BN, ZrB_2
MgO	LiF, NaF	MgFe, Fe, Cr, Mo, Ni, BN
BeO	Li_2O	Graphite
Si_3N_4	MgO, Y_2O_3, $BeSiN_2$	–
SiC	B, Al, Al_2O_3	–
ZrO_2	–	H_2, Cr, Ti, Ni, Mn
$BaTiO_3$	–	Ti, Ta, Al/Si/Ti
Y_2O_3	–	Th

The dominance of the gray and black areas in Fig. 16 confirms the primary phase of ZnO and the pore or secondary phase of Zn–Ga–In–O. Moreover, the secondary spinel phase $ZnGa_2O_4$ is present in Fig. 16(a), which corresponds to the XRD results for y = 0 in Fig. 15(b). When the amount of In doping increased from 0 to 0.005, $ZnGa_2O_4$, the secondary spinel phase, disappeared, and the secondary Zn–Ga–In–O phases in the white area started to appear at y = 0.005, as shown in Fig. 16(b). The secondary Zn–Ga–In–O phases still existed at y = 0.01, where the fraction of the white area was small compared with the gray area of the primary phase, as shown in Fig. 16(c). It is possible to increase the proportion of In within the white area by forming solid solutions or by diffusion [31]. In addition, when the amount of In reached y = 0.02, the white area that contained high amounts of In spread out in agglomerated clusters, as shown in Fig. 16(d).

The EDS maps of In and Ga in $[Zn_{(1-x-y)}Ga_xIn_y]O$ (x = 0.02) with y = 0, 0.005, 0.01, and 0.02, respectively, as shown in Fig. 17(a)–17(d). The secondary spinel phase ($ZnGa_2O_4$) was verified by the EDS maps, as shown in Fig. 17(a). When In increased from y = 0 to 0.005 in $[Zn_{(1-x-y)}Ga_xIn_y]O$ (x = 0.02), $ZnGa_2O_4$ disappeared, Zn–Ga–In–O appeared, and the agglomerated clusters of Ga decreased. It is assumed that Ga was doped homogeneously into the ZnO matrix by comparison of the compositions with y = 0 and 0.005, as shown in Fig. 17(a) and (b), respectively. In addition, Zn–Ga–In–O phases remained in agglomerated clusters when In was doped to y = 0.01, as shown in Fig. 17(c). The high intensity of In indicates an increased amount of inhomogeneous In clusters. It should be noted that the fine color scale bar of In on the left side of the EDS maps, as shown in Fig. 17(c), indicates the high count (white color) of elements as compared with those in y = 0.005 and 0.02, which makes it difficult to distinguish the existence of In in the overall area. In addition, when the amount of In increased to 0.02, the agglomerated clusters of the Zn–Ga–In–O phases exhibited high amounts of In, as shown in Fig. 17(d). The secondary phase of $ZnGa_2O_4$, which disappeared in the range y = 0.005–0.02,

was confirmed through the EDS maps, and the EDS mapping results are consistent with Fig. 15 and Fig. 16.

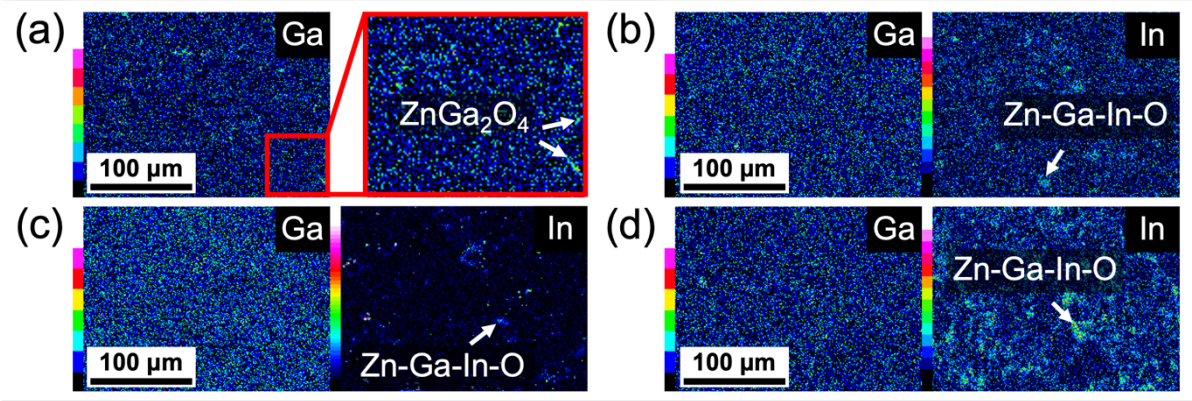

Fig. 17. EDS maps of In and Ga in $[Zn_{(1-x-y)}Ga_xIn_y]O$ (x = 0.02); (a) y = 0, (b) y = 0.005, (c) y = 0.01, and (d) y = 0.02.

The atomic composition of the ZnO matrix was examined by EDS point analysis. The atomic composition was averaged over twenty spots on the matrix, and all of the numbers were normalized to 100% (Table 3). In the primary phase, the Ga-doped ZnO (x = 0.02; y = 0) was determined to have a Ga content of 0.7 at.%, and it was increased to 0.8 at.% in the In- and Ga-doped ZnO (x = 0.02; y = 0.005) specimen. The highest solubility of Ga in the ZnO matrix was confirmed in the composition with y = 0.005. From this result, the highest solubility was revealed to be Ga/In in a 0.02/0.005 ratio, in comparison with those of the y = 0.01 and 0.02 specimens. Although the Zn–Ga–In–O secondary phases were not revealed (except for the $ZnGa_2O_4$ secondary spinel phase) through the XRD analysis in Fig. 15, they were confirmed by EDS point analysis. Furthermore, doping with In contributed to the solubility of Ga in ZnO; in other words, doping with In and Ga increased the solubility of Ga in ZnO (x = 0.02; y = 0.005). According to a previous report, the solubility of Ga in bulk ZnO is strictly limited to 1 at.% [5], and the solubility of Ga was determined to be less than 0.8 at.% in the In- and Ga-

doped ZnO specimens in this study, which is in good agreement with previous results [5]. Although the XRD results showed no observable secondary phases except $ZnGa_2O_4$, the secondary phases of Zn–Ga–In–O were confirmed by EDS analysis.

Table 3. Atomic composition of the ZnO matrix determined by EDS point analysis of SPSed $[Zn_{(1-x-y)}Ga_xIn_y]O$ (x = 0.02; y = 0, 0.005, 0.01, 0.02). The standard deviations of the mean atomic composition are given in parentheses.

		Atomic composition (at.%)			
Specimen	Phase	Zn	Ga	In	Total
x = 0.02, y = 0	Primary phase	99.3(7)	0.7(7)		100
x = 0.02, y = 0.005		99.0(7)	0.8(7)	0.2(2)	100
x = 0.02, y = 0.01		99.2(6)	0.6(6)	0.2(1)	100
x = 0.02, y = 0.02		98.9(6)	0.7(6)	0.4(2)	100

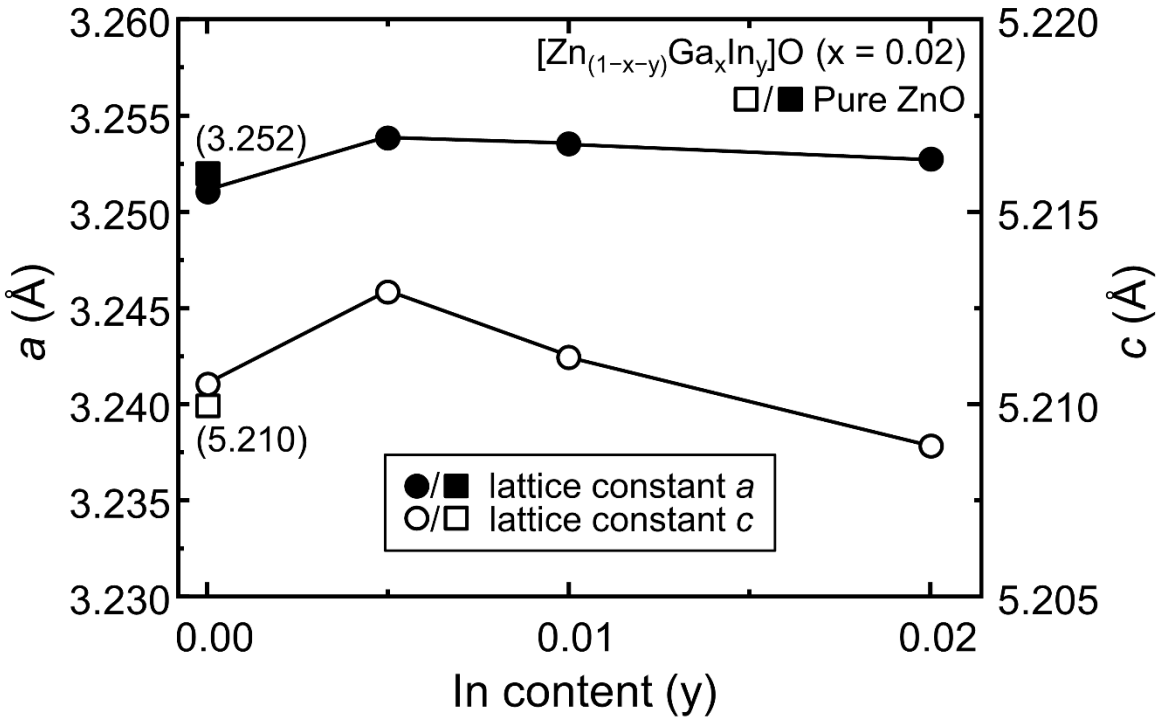

Fig. 18. Lattice constants with respect to the nominal concentration of $[Zn_{(1-x-y)}Ga_xIn_y]O$ (x = 0.02; y = 0, 0.005, 0.01, 0.02) and pure ZnO.

The lattice constants of In- and Ga-doped ZnO as well as pure ZnO, which were slightly changed by doping with different amounts of In, were investigated after Rietveld refinement, as shown in Fig. 18. The lattice constants of the non-substituted pure ZnO were *a* = 3.252 Å and *c* = 5.210 Å, which is in agreement with previous observations [32]. The decrease in lattice constant *a* and increase in lattice constant *c* of the specimen with y = 0 compared with those of pure ZnO indicate the influence of the $ZnGa_2O_4$ spinel secondary phase (*a* = 8.333 Å) [33] and substitution of Ga^{3+} in the position of Zn^{2+}. As the content of In increased to y = 0.005, the lattice constants *a* and *c* increased, indicating the substitution of In^{3+} into the ZnO matrix. The lattice constant *a* was constant, whereas the tendency of the lattice constant *c* to decrease was due to the dominant substitution of Ga^{3+} into the ZnO matrix in the compositions with y = 0.01 and 0.02. The lattice constants of the In- and Ga-substituted specimens were within 0.1%

difference of those of pure ZnO. Because the ionic radii of In^{3+}, Ga^{3+}, and Zn^{2+} are similar, it is expected that In^{3+} and Ga^{3+} can substitute Zn^{2+} in the ZnO matrix.

2.3.3. Electrical Conductivity

Figure 19 shows the temperature dependence of the electrical conductivity (σ), Seebeck coefficient (S), and power factor ($S^2\sigma$). The electrical conductivity and Seebeck coefficient are given by the following equations:

$$\sigma = ne\mu \quad (2)$$

$$S = \frac{8\pi^2 k_B^2}{3eh^2} m^* T \left(\frac{\pi}{3n}\right)^{2/3} \quad (3)$$

where n is the number of carriers, e is the electron charge (1.602×10^{-19} Coulomb), μ is the carrier mobility, k_B is the Boltzmann constant, m^* is the effective mass of the carrier, h is the Planck constant (6.626×10^{-34} m^2 kg s^{-1}), and n is the carrier concentration.

The electrical conductivity of all specimens gradually decreased with increasing measurement temperature from 340 to 1046 K, demonstrating metallic behavior [34], as shown in Fig. 19. Figure 19(a) shows that the ZnO specimen doped only with Ga (y = 0) had the lowest values of electrical conductivity, from 1.11×10^3 to 6.08×10^2 S cm^{-1} from 340 to 1046 K, respectively, owing to the segregation of the secondary spinel phase $ZnGa_2O_4$ [15]. In contrast, the specimens (y = 0.005, 0.01, 0.02) with increased carrier concentrations had high electrical conductivities of 2.44–3.61×10^3 to 1.46–2.03×10^3 S cm^{-1} from 340 to 1046 K. The increase in electrical conductivity is assumed to be due to the substitution of Zn by doping with In and Ga.

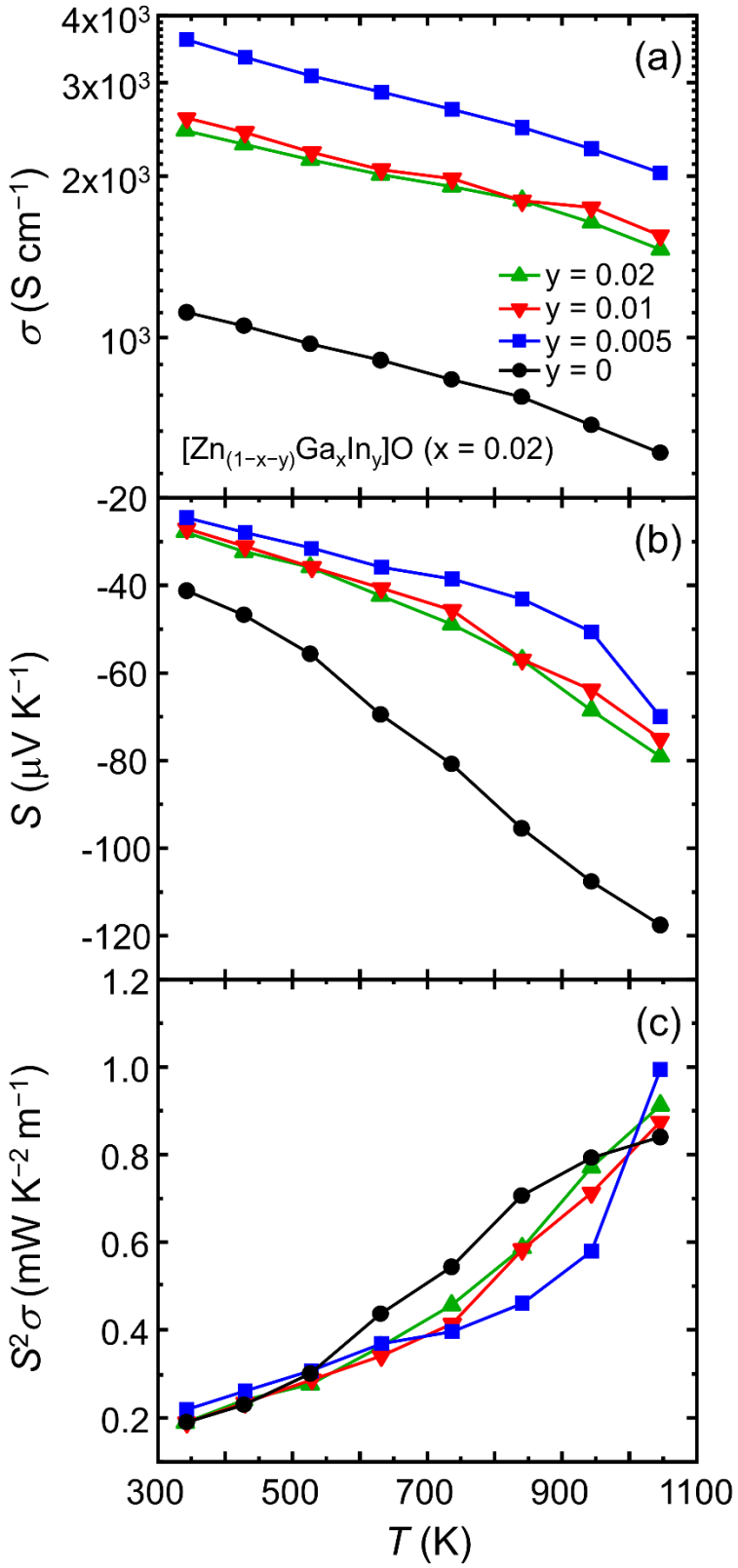

Fig. 19. Temperature dependence of the (a) electrical conductivity σ, (b) Seebeck coefficient S, and (c) power factor $S^2\sigma$ of $[Zn_{(1-x-y)}Ga_xIn_y]O$ (x = 0.02; y = 0, 0.005, 0.01, 0.02).

The highest electrical conductivity (2.03×10^3 S cm^{-1}) was obtained for the specimen with y = 0.005, which had the highest solubility of Ga at 1046 K, as shown in Table 3. The electrical conductivity of the present specimen had a high value of 2.67×10^3 S cm^{-1} in comparison with approximately 700 S cm^{-1} at 773 K [14,15]. This high electrical conductivity in the present specimen was due to the well-dispersed doping effect. Moreover, it can be elucidated that In and Ga were well-doped in the ZnO matrix because the specimen had the lowest agglomerated clusters in comparison to the other doped specimens (y = 0.01, 0.02), as shown in Fig. 17(b). Figures 19 (a) and (b) indicate the inverse relationship of the electrical conductivity and the absolute value of the Seebeck coefficient with the amount of doping. According to Eq. (3), the absolute value of the Seebeck coefficient increases with temperature, as shown in Fig. 19(b). The power factor of the In- and Ga-doped specimen with y = 0.005 improved in comparison to the Ga-doped specimen (y = 0), and the value of the power factor increased from 0.84 to 0.99 mW K^{-2} m^{-1} at 1046 K, as shown in Fig. 19(c). Accordingly, site substitution is an applicable method for increasing the power factor of ZnO. In and Ga act as dopants, generating electron carriers that produce TE effects; therefore, they are expected to be promising dopants for crystal structure stabilization or carrier tuning [35].

2.3.4. Thermal Conductivity and Dimensionless Figure of Merit

The thermal conductivity (κ) is composed of the electron and lattice thermal conductivities. The energy conversion efficiency and dimensionless figure of merit *(ZT*) of TE materials can be expressed using the following equation:

$$ZT = \frac{S^2\sigma}{\kappa_{\text{tot}}} = \frac{S^2\sigma}{\kappa_{\text{el}} + \kappa_{\text{lat}}}T \qquad (4)$$

where S is the Seebeck coefficient, σ is the electrical conductivity, and κ_{tot} is the total thermal conductivity, which consists of the electron thermal conductivity (κ_{el}) and lattice thermal conductivity (κ_{lat}) [36].

The temperature dependence of the thermal conductivity of $[Zn_{(1-x-y)}Ga_xIn_y]O$ (x = 0.02; y = 0, 0.005, 0.01, 0.02) and pure ZnO is plotted in Fig. 20. The total thermal conductivity of each specimen and pure ZnO is shown in Fig. 20(a). The thermal conductivities of all the specimens decreased substantially with increasing temperature. Factors such as particle size, density of the sintered specimen, porosity, and temperature can affect the thermal conductivity [11,12,37]. As mentioned above, thermal conductivity is derived from two components, and κ_p (phonon conductivity) is obtained from the following relationship:

$$\kappa_p = \kappa_i \propto \frac{1}{T} \qquad (5)$$

where κ_i is the intrinsic conductivity, and T is the absolute temperature, which are inversely proportional to each other [37]. The equation indicates the correlation between thermal conductivity and temperature, showing the reason for the decrease in thermal conductivity with increasing temperature. The decrease in total thermal conductivity was obtained by doping with In and Ga at low temperatures in the range 340–530 K. The high total thermal conductivity of 35 W K^{-1} m^{-1} for pure ZnO was dramatically decreased by the substitution of In and Ga, with a total thermal conductivity of 18 W K^{-1} m^{-1} with y = 0.01 at 340 K. The total thermal conductivity values of the specimen were 4 W K^{-1} m^{-1} with y = 0, 6 W K^{-1} m^{-1} with y = 0.01, 7 W K^{-1} m^{-1} with y = 0.02, and 8 W K^{-1} m^{-1} with y = 0.005 at 1046 K, and the specimen with y = 0 had a total thermal conductivity that was lower than the 5 W K^{-1} m^{-1} of pure ZnO at 1046 K.

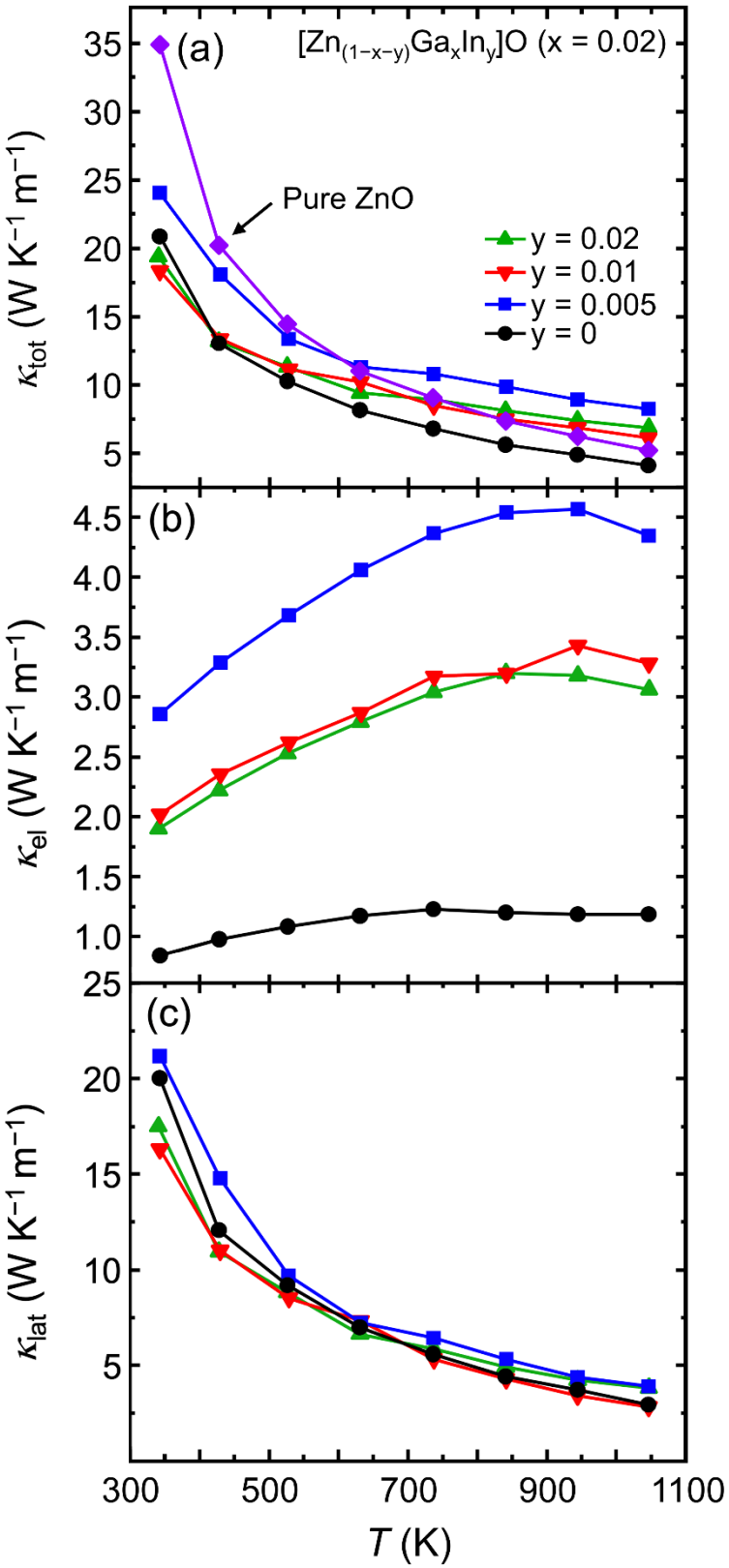

Fig. 20. Temperature dependence of the (a) total thermal conductivity (κ_{tot}), (b) electron thermal conductivity (κ_{el}), and (c) lattice thermal conductivity (κ_{lat}) of $[Zn_{(1-x-y)}Ga_xIn_y]O$ (x = 0.02; y = 0, 0.005, 0.01, 0.02) and pure ZnO.

A correlation between the thermal conductivity and the grain size has been reported, where the thermal conductivity decreases with decreasing grain size [24,38]. In the crystal lattice, thermal conductivity occurs due to phonon scattering because lattice vibrations contribute to thermal conductivity, as shown in Eq. (6) [39]. Consequently, a smaller grain size can shorten the phonon mean free path or enhance phonon scattering, thereby reducing the thermal conductivity.

$$\kappa = \frac{1}{3}\int C\rho v l \qquad (6)$$

where C is the specific heat, ρ is the density, v is the speed of sound, and l is the phonon mean free path. The calculated values of the electron thermal conductivity and lattice thermal conductivity are shown in Fig. 20(b) and 20(c), respectively. Figure 20(b) shows a trend similar to that of the electrical conductivity owing to their relationship, as presented in Eq. (7) [6]. Additionally, the decrease in the electron thermal conductivity indicates that the electrical conductivity greatly influenced the electron thermal conductivity above 944 K, as shown in Fig. 20(b), and the electron thermal conductivity can be estimated from the Wiedemann–Franz law, given by the following equation:

$$\kappa_{\mathrm{el}} = L\sigma T \qquad (7)$$

where σ is the electrical conductivity, T is the absolute temperature, and L is the Lorentz number (2.44×10^{-8} W Ω K^{-2}) [40]. According to previous research, the degenerate limit of the Lorentz number has errors when the Seebeck coefficient of the material is smaller than 50 μV K^{-1}. For this reason, the appropriate Lorentz number [41,42] was calculated using the following equation:

$$L = 1.5 + \exp\left[-\frac{|S|}{116}\right] \qquad (8)$$

The lattice thermal conductivity can be calculated using the equation $\kappa_{lat} = \kappa_{tot} - \kappa_{el}$. This is attributed to the crystalline structure, whereas the electron thermal conductivity generally depends on the concentration and mobility of the carrier. The lattice thermal conductivities of $[Zn_{(1-x-y)}Ga_xIn_y]O$ with y = 0.01 and 0.02 were 16 and 18 W K^{-1} m^{-1}, respectively, at 340 K. This result possibly corresponds to difference in the densities of the specimens with y = 0.01 and 0.02, 98.2% and 99.5%, respectively. The specimen with y = 0.01 was more porous than the y = 0.02 specimen; therefore, it achieved the lowest lattice thermal conductivity at 340 K, as shown in Fig. 20(c). Pores have a strong effect on the thermal conductivity of ceramics because they are a major interruption to the crystal lattice [35]. In contrast, doping with In and Ga had no significant effect at high temperatures, and it is concluded that the temperature is a predominant factor affecting the thermal conductivity, as presented in Eq. (5). At low temperatures, the lattice thermal conductivity was dominant, whereas the contributions of the electron and lattice thermal conductivities were similar at high temperatures, as shown in Fig. 20(b) and (c). The electron thermal conductivity varied in the ranged 0.84–2.86 W K^{-1} m^{-1} with a difference of 2.02 W K^{-1} m^{-1} at 340 K, whereas it fluctuates in the range 1.18–4.35 W K^{-1} m^{-1} with a difference of 3.17 W K^{-1} m^{-1} at 1046 K, as shown in Fig. 20(b). The comparatively small difference of 2.02 W K^{-1} m^{-1} led to a non-monotonic reduction in the lattice thermal conductivity (= $\kappa_{tot} - \kappa_{el}$) at low temperatures, while a monotonic reduction was observed owing to the large difference of 3.17 W K^{-1} m^{-1} at high temperatures, as shown in Fig. 20(b). This affects the lattice thermal conductivity, as shown in Fig. 20(c).

The increase in the dimensionless figure of merit with increasing temperature was calculated and is shown in Fig. 21. There was no significant difference in the lattice thermal

conductivity at high temperatures by doping with In and Ga. Therefore, the *ZT* value of the y = 0 specimen was the highest (*ZT* = 0.178 at 1046 K), and the *ZT* values of the specimen with y = 0.005, 0.01, and 0.02 were lower than that of the specimen with y = 0 because of the dispersed secondary phase (clusters of Zn–Ga–In–O), as shown in Fig. 17(b)–17(d), indicating insufficient doping conditions.

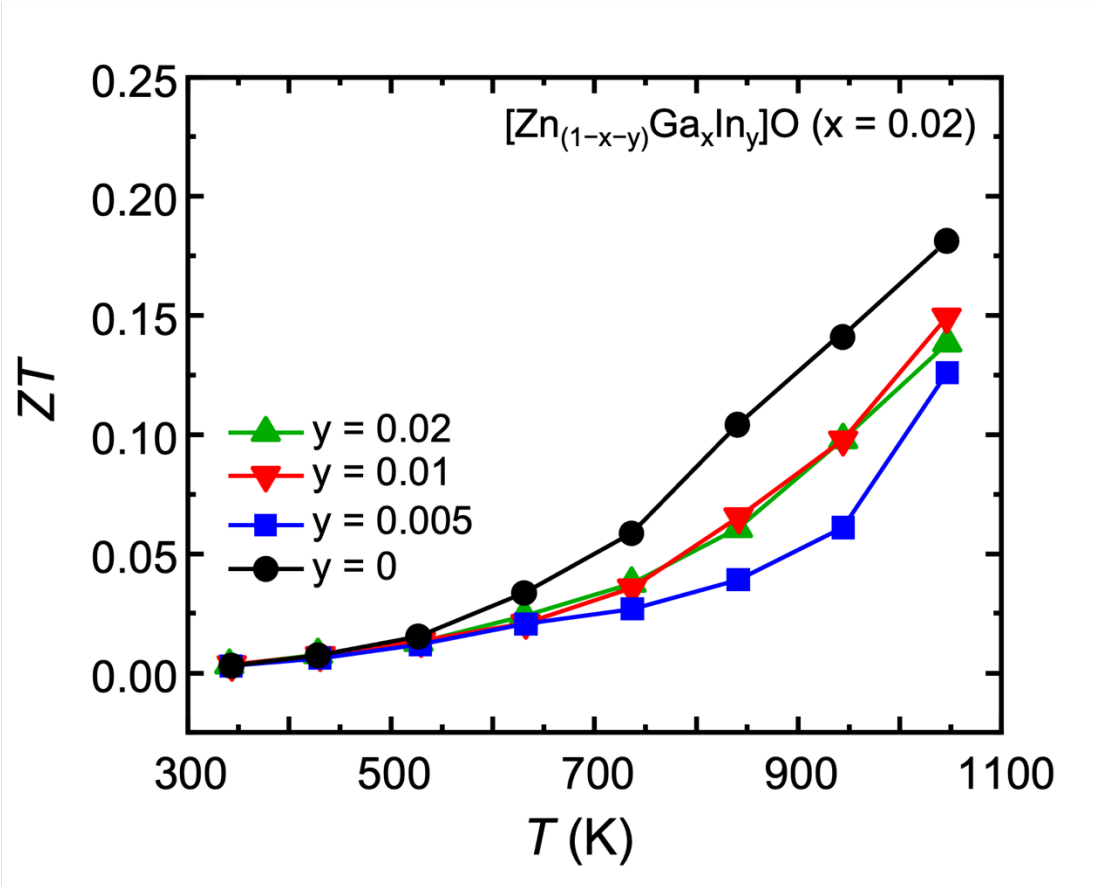

Fig. 21. Dimensionless figure of merit (*ZT*) of $[Zn_{(1-x-y)}Ga_xIn_y]O$ (x = 0.02; y = 0, 0.005, 0.01, 0.02).

2.4. Conclusions

In this study, $[Zn_{(1-x-y)}Ga_xIn_y]O$ (x = 0, 0.02; y = 0, 0.005, 0.01, 0.02) ceramics were fabricated via SPS at 1423 K, and the effects of doping with group 13 elements on the TE properties were examined. Crystal structure and microstructural analyses indicated the presence of a spinel secondary phase ($ZnGa_2O_4$) or intermediate compounds (Zn–Ga–In–O) with a high relative density, and $ZnGa_2O_4$ disappeared as In increased from y = 0 to 0.005. The secondary phase in the In- and Ga-doped ZnO was not identified from the XRD results, but it was confirmed by the chemical composition from the SEM/EDS analysis.

It can be concluded that the addition of In contributed to the increase in the solubility of Ga because doping with In and Ga enabled a higher doping of Ga. Consequently, the highest power factor of 0.99 mW K^{-2} m^{-1} was obtained by the $[Zn_{(1-x-y)}Ga_xIn_y]O$ specimen with x = 0.02 and y = 0.005 at 1046 K. It is notable that doping with In and Ga could reduce the thermal conductivity, attaining ZT = 0.003–0.015 from 340 to 530 K, respectively. This means that doping In and Ga into the ZnO matrix is useful for decreasing the thermal conductivity at 340–530 K.

References

[1] G.J. Snyder, E.S. Toberer, Complex thermoelectric materials, Nat. Mater. 7 (2008) 105–114.

[2] C.B. Vining, An inconvenient truth about thermoelectrics, Nat. Mater. 8 (2009) 83–85.

[3] T. Tsubota, M. Ohtaki, K. Eguchi, H. Arai, Thermoelectric properties of Al-doped ZnO as a promising oxide material for high-temperature thermoelectric conversion, J. Mater. Chem. 7 (1997) 85–90.

[4] S. Isobe, T. Tani, Y. Masuda, W.S. Seo, K. Koumoto, Thermoelectric performance of yttrium-substituted $(ZnO)_5In_2O_3$ improved through ceramic texturing, Jpn. J. Appl. Phys. 41 (2002) 731–732.

[5] J.P. Wiff, Y. Kinemuchi, K. Watari, Hall mobilities of Al- and Ga-doped ZnO polycrystals, Mater. Lett. 63 (2009) 2470–2472.

[6] T. Tsubota, M. Ohtaki, K. Eguchi, H. Arai, Thermoelectric properties of ZnO doped with the group 13 elements, in: Proceedings of the 16th International Conference on Thermoelectrics, IEEE, Piscataway (1997) 240–243.

[7] H.S. Kim, S.I. Kim, K.H. Lee, S.W. Kim, G.J. Snyder, Phonon scattering by dislocations at grain boundaries in polycrystalline $Bi_{0.5}Sb_{1.5}Te_3$, Phys. Status Solidi B 254 (2017) 1600103.

[8] H. Kaga, R. Asahi, T. Tani, Thermoelectric properties of doped $(ZnO)_mIn_2O_3$, Jpn. J. Appl. Phys. 43 (2004) 3540–3543.

[9] Y. Michiue, H. Nishijima, Y. Suzuki, T. Mori, Synthesis and thermoelectric properties of composite oxides in the pseudobinary system $ZnO\text{-}Ga_2O_3$, Solid State Sci. 65 (2017) 29–32.

[10] Y. Michiue, T. Mori, A. Prytuliak, Y. Matsushita, M. Tanaka, N. Kimizuka, Electrical, optical, and thermoelectric properties of $Ga_2O_3(ZnO)_9$, RSC Adv. 1 (2011) 1788–1793.

[11] S. Saini, P. Mele, T. Oyake, J. Shiomi, J.P. Niemelä, M. Karppinen, K. Miyazaki, C. Li, T. Kawaharamura, A. Ichinose, L. Molina-Luna, Porosity-tuned thermal conductivity in thermoelectric Al-doped ZnO thin films grown by mist-chemical vapor deposition, Thin Solid Films. 685 (2019) 180–185.

[12] R.V.R. Virtudazo, B. Srinivasan, Q. Guo, R. Wu, T. Takei, Y. Shimasaki, H. Wada, K. Kuroda, S. Bernik, T. Mori, Improvement in the thermoelectric properties of porous networked Al-doped ZnO nanostructured materials synthesized via an alternative interfacial reaction and low-pressure SPS processing, Inorg. Chem. Front. 7 (2020) 4118–4132.

[13] N.H.T. Nguyen, T.H. Nguyen, Y.R. Liu, M. Aminzare, A.T.T. Pham, S. Cho, D.P. Wong, K.H. Chen, T. Seetawan, N.K. Pham, H.K.T. Ta, V.C. Tran, T.B. Phan, Thermoelectric properties of indium and gallium dually doped ZnO thin films, ACS Appl. Mater. Interfaces 8 (2016) 33916–33923.

[14] A.T.T. Pham, T.A. Luu, N.K. Pham, H.K.T. Ta, T.H. Nguyen, D.V. Hoang, H.T. Lai, V.C. Tran, J.H. Park, J.K. Lee, S. Park, O. Michitaka, S.D. Park, H.Q. Nguyen, T.B. Phan, Multi-scale defects in ZnO thermoelectric ceramic materials co-doped with In and Ga, Ceram. Int. 46 (2020) 10748–10758.

[15] O.K.T. Le, A.T.T. Pham, N.K. Pham, T.H.C. Pham, T.H. Nguyen, D.V. Hoang, H.K.T. Ta, D.C. Truong, H.T. Lai, T.D.T. Ung, V.C. Tran, T.B. Phan, Compensation of Zn substitution and secondary phase controls effective mass and weighted mobility in In and Ga co-doped ZnO material, J. Materiomics 7 (2021) 742–755.

[16] T. Mori, Novel principles and nanostructuring methods for enhanced thermoelectrics, Small 13 (2017) 1702013.

[17] P.M. Radingoana, S. Guillemet-Fritsch, P.A. Olubambi, G. Chevallier, C. Estournès, Influence of processing parameters on the densification and the microstructure of pure

zinc oxide ceramics prepared by spark plasma sintering, Ceram. Int. 45 (2019) 10035–10043.

[18] P.M. Radingoana, S. Guillemet-Fritsch, J. Noudem, P.A. Olubambi, G. Chevallier, C. Estournès, Thermoelectric properties of ZnO ceramics densified through spark plasma sintering, Ceram. Int. 46 (2020) 5229–5238.

[19] J.H. Lee, J.G. Li, B.N. Kim, Q. Meng, X. Sun, B.K. Jang, Effect of annealing on microstructure and luminescence characteristics in spark plasma sintered Ce^{3+}-activated $(Gd, Lu)_3Al_5O_{12}$ garnet ceramics, J. Eur. Ceram. Soc. 41 (2021) 1586–1592.

[20] X. Liang, C. Wang, Electron and phonon transport anisotropy of ZnO at and above room temperature, Appl. Phys. Lett. 116 (2020) 043903.

[21] K. Momma, F. Izumi, VESTA 3 for three-dimensional visualization of crystal, volumetric and morphology data, J. Appl. Cryst. 44 (2011) 1272–1276.

[22] R.D. Shannon, Revised effective ionic radii and systematic studies of interatomic distances in halides and chalcogenides, Acta Crystallogr. A 32 (1976) 751–767.

[23] M.W. Barsoum, Series in material science and engineering: Fundamentals of ceramics, 1st ed., Institute of Physics Publishing, Bristol and Philadelphia, 2003.

[24] F. Giovannelli, C. Chen, P. Díaz-Chao, E. Guilmeau, F. Delorme, Thermal conductivity and stability of Al-doped ZnO nanostructured ceramics, J. Eur. Ceram. Soc. 38 (2018) 5015–5020.

[25] X. Kuang, G. Carotenuto, L. Nicolais, A review of ceramic sintering and suggestions on reducing sintering temperatures, Adv. Perform. Mater. 4 (1997) 257–274.

[26] Z.A. Munir, U. Anselmi-Tamburini, M. Ohyanagi, The effect of electric field and pressure on the synthesis and consolidation of materials: a review of the spark plasma sintering method, J. Mater. Sci. 41 (2006) 763–777.

[27] S.J.L. Kang, Sintering: densification, grain growth, and microstructure, Elsevier

Butterworth-Heinemann (2005) Ch.1, pp. 6–7.

[28] W. Komatsu, Y. Moriyoshi, N. Seto, Synergetic effect of ZnO with different dopents on sintering, Yogyo Kyokai. 77 (1969) 347–353.

[29] H.Ö. Toplan, H. Erkalfa, O.T. Özkan, The effect of the PbO addition on the sintering of ZnO, Ceram. - Silik. 47 (2003) 116–119.

[30] J. Kim, T. Kimura, T. Yamaguchi, Sintering of Sb_2O_3-doped ZnO, J. Mater. Sci. 24 (1989) 213–219.

[31] C. Qi, J. Chen, B. Sun, S. Liu, M. Liu, Y. Shu, J. He, Microstructure and phase transformation of IGZO targets with different stoichiometry during sintering, Ceram. Int. 46 (2020) 10568–10577.

[32] Ü. Özgür, Y.I. Alivov, C. Liu, A. Teke, M.A. Reshchikov, S. Doğan, V. Avrutin, S.J. Cho, H. Morkoç, A comprehensive review of ZnO materials and devices, J. Appl. Phys. 98 (2005) 041301.

[33] Z. Galazka, S. Ganschow, R. Schewski, K. Irmscher, D. Klimm, A. Kwasniewski, M. Pietsch, A. Fiedler, I. Schulze-Jonack, M. Albrecht, T. Schröder, M. Bickermann, Ultra-wide bandgap, conductive, high mobility, and high quality melt-grown bulk $ZnGa_2O_4$ single crystals, APL Mater. 7 (2019) 022512.

[34] B. Zhou, L. Chen, C. Li, N. Qi, Z. Chen, X. Su, X. Tang, Significant enhancement in the thermoelectric performance of aluminum-doped ZnO tuned by pore structure, ACS Appl. Mater. Interfaces 12 (2020) 51669−51678.

[35] J.S. Yoon, J.M. Song, J.U. Rahman, S. Lee, W.S. Seo, K.H. Lee, S. Kim, H.S. Kim, S.I. Kim, W.H. Shin, High thermoelectric performance of melt-spun $Cu_xBi_{0.5}Sb_{1.5}Te_3$ by synergetic effect of carrier tuning and phonon engineering, Acta Mater. 158 (2018) 289–296.

[36] M. Ohtaki, K. Araki, K. Yamamoto, High thermoelectric performance of dually doped

ZnO ceramics, J. Electron. Mater. 38 (2009) 1234–1238.

[37] B.K. Jang, Y. Sakka, Thermophysical properties of porous SiC ceramics fabricated by pressureless sintering, Sci. Technol. Adv. Mater. 8 (2007) 655–659.

[38] B.K. Jang, Y. Sakka, Influence of microstructure on the thermophysical properties of sintered SiC ceramics, J. Alloys Compd. 463 (2008) 493–497.

[39] B.K. Jang, Y. Sakka, N. Yamaguchi, H. Matsubara, H.T. Kim, Thermal conductivity of EB-PVD ZrO_2-4mol% Y_2O_3 films using the laser flash method, J. Alloys Compd. 509 (2011) 1045–1049.

[40] L. Han, N.V. Nong, W. Zhang, L.T. Hung, T. Holgate, K. Tashiro, M. Ohtaki, N. Pryds, S. Linderoth, Effects of morphology on the thermoelectric properties of Al-doped ZnO, RSC Adv. 4 (2014) 12353–12361.

[41] H.S. Kim, Z.M. Gibbs, Y. Tang, H. Wang, G.J. Snyder, Characterization of Lorenz number with Seebeck coefficient measurement, APL Mater. 3 (2015) 041506.

[42] K.H. Lee, S.W. Kim, Design and preparation of high-performance bulk thermoelectric materials with defect structures, J. Korean Ceram. Soc. 54 (2017) 75–85.

Chapter 3. Thermoelectric Performance of In and Ga Single/Dual-doped ZnO Ceramics Fabricated by SPS

3.1. Introduction

The social needs to meet the global energy demand and to solve environmental issues have increased over the past a few decades. Thermoelectric (TE) power generation is an efficient approach for harvesting energy from waste-heat, and TE materials allow the direct conversion of heat into electricity and vice versa through the Seebeck and Peltier effects, respectively [1,2]. The energy conversion efficiency (η) of a TE device mainly depends on its constituent materials via the dimensionless figure of merit $ZT = S^2\sigma T\kappa^{-1}$, where S, the Seebeck coefficient; σ, the electrical conductivity; T, absolute temperature; κ ($\kappa_{tot}= \kappa_{ele}+ \kappa_{lat}$), the total thermal conductivity, which comprises of the electron and lattice thermal conductivities. The η of TE devices depend on the ZT values as defined in Eq. (1) [3].

$$\eta = \frac{\Delta T}{T_h}\frac{\sqrt{1+ZT}-1}{\sqrt{1+ZT}+T_c/T_h} \quad (1)$$

where $\Delta T/T_h$ is the Carnot efficiency and ZT is the dimensionless figure of merit of the material. It can be seen that with an increase in the ZT value, the conversion efficiency increases. Therefore, it is necessary to maximize the ZT value of TE materials by increasing their power factor (PF, $S^2\sigma$) and reducing the thermal conductivity in order to improve their TE performance.

ZnO-based TE materials [4–11], such as Al-, In-, and Ga-doped ZnO, have gained immense attention because of their thermal stability at high temperatures. An efficient approach to increase the electrical conductivity of ZnO-based TE materials is to dope them with various

elements, such as In and Ga, because the ionic radii of In^{3+} (0.80 Å, coordination VI), Ga^{3+} (0.62 Å, coordination VI), and Zn^{2+} (0.74 Å, coordination VI) are comparable [11]. It is expected that as *n*-type dopants, In^{3+} and Ga^{3+} can substitute Zn^{2+}. Even though In- and Ga-doped ZnO has great potential as a TE material, only a few studies have been conducted on the TE performance of In- and Ga-doped ZnO [4,7,13]. Therefore, the effects of In and Ga dopants on the TE properties of ZnO have not been extensively investigated yet. In our previous work, we have reported that the *ZT* values of the dual-doped ZnO with In and Ga were still lower than that of Ga single-doped ZnO [7]. In addition, to prevent misunderstanding of the TE properties as well as the chemical and thermal stability of oxide-based TE materials at high temperatures, we have thus investigated this subject using epitaxial thin films of oxide based TE materials. Moreover, there is any research on the thin film of ZnO doped with In and Ga grown by reactive solid-phase epitaxy so it is needed to figure out the difference between the types of bulk and thin film on TE properties.

In this study, the TE properties of single/dual-doped ZnO ceramics prepared using a solid-state reaction and spark plasma sintering (SPS) with varying amounts of In and Ga as the dopants were investigated. SPS has the advantage of fast heating rates with applying pressure, and realizes high relative densities at low temperatures as compared to the conventional hot pressing method [14]. In particular, rapid consolidation can minimize the grain-growth, which is a prerequisite for TE materials to induce the phonon scattering effect at the grain boundaries [15].

The purpose of this study is to investigate the effect of the compositions of In and Ga single/dual-doped ceramics, which are two types of bulk and thin film on their TE performance. Microstructural and chemical composition analyses and TE measurements are conducted to identify the key factors affecting the TE properties of the ceramics.

3.2. Experimental Procedures

In chapter 3, two types of In and Ga doped ZnO, which are bulk and thin film, were fabricated. ZnO, Ga_2O_3, and In_2O_3 powders and ZnO, Ga_2O_3, and In_2O_3 nano powders (< 150 nm) were used as the starting materials (99.99%, Sigma-Aldrich, USA).

For the preparation of bulk type of ZnO, the raw powders were mixed to obtain single-doped ZnO with In, $[Zn_{(1-y)}In_y]O$ (y = 0.005, 0.01, 0.02, 0.03, 0.05), and dual-doped ZnO with In and Ga, $[Zn_{(1-x-y)}Ga_xIn_y]O$ (y = 0.005; x = 0.005, 0.01, 0.02, 0.03, 0.05), using the solid-state reaction method. For the preparation of thin film of ZnO, the composition is same with the dual-doped ZnO with In and Ga. The raw powder mixture was milled by planetary ball milling (Pulverisette 6, Fritsch GmbH, Germany) at a speed of 100 rpm using zirconia balls with a diameter of 5 mm as the mixing media. This dry process involved 40 cycles with a run time of 30 s and a pause time of 2 min to disperse the dopants in ZnO and to prevent the sticking of the mixture to the zirconia pot. The zirconia balls were separated from the mixture, and the mixture was sieved using a 250-mesh sieve to obtain uniform particle sizes. The mixture was then uniaxially pressed at 100 MPa into pellets with a thickness of 3 mm and a diameter of 20 mm. To improve the homogeneity of the pellets, the samples were calcined twice at 1373 K for 24 h with a heating rate of 100 K/h and cooled to 300 K in an air atmosphere. After the first calcination, the pellets were thoroughly ground in an agate mortar for 20 min, sieved, and pressed at 100 MPa into pellets with a thickness of 8 mm and a diameter of 10 mm. The second calcination was carried out under the same conditions as those for the first calcination, and the calcined pellets were reground and sieved. The powder was poured into a graphite mold with a diameter of 10 mm, lined with carbon paper, and uniaxially pressed by a graphite punch for the first pre-pressing under 50 MPa for 1 min before loading in the SPS chamber.

The powder was consolidated using a SPS machine (PLASMAN CSP-I-03121, S. S. Alloy, Japan) to obtain dense ceramics. The graphite die was placed in a vacuum chamber, which was

evacuated at ≤ 15 Pa. The powder was heated to 1423 K at a high heating rate of 100 K/min under a uniaxial pressure of up to 50 MPa and a holding time of 15 min. Subsequently, the pressure was released to prevent the formation of cracks by the external pressure, and the furnace was cooled to 373 K at the cooling rate of 20 K/min. The temperature was controlled using a proportional–integral–derivative control [16]. The height of the samples obtained after the consolidation was approximately 7.5 mm.

Powder X-ray diffraction (XRD) was carried out over the 2θ range of 20–80° at a scanning step of 0.01° using an X-ray diffractometer (MiniFlex600, Rigaku, Japan) with Cu Kα radiation (λ = 1.5406 Å) with a source power of 40 kV and 15 mA. The crystal structures of the single/dual-doped sintered samples were refined via the Rietveld refinement [17]. The microstructures and surface morphologies of the diamond-polished samples were examined using a scanning electron microscope (SEM, JCM-6000Plus NeoScope JEOL, Japan) with a backscattered electron (BSE) detector at an acceleration voltage of 15 kV. The chemical compositions of the ceramics were estimated using X-ray energy-dispersive spectroscopy (EDS).

For the characterization of thin film ZnO, several additional processes were carried out. All the experimental procedures are same up to the step of the consolidation by SPS. The experimental procedures explained below. A ZnO single crystalline layer was epitaxially grown on the YSZ substrate by a pulsed-laser-deposition (PLD) technique. The background pressure in the PLD chamber was 2×10^{-6} Pa, while the oxygen gas pressure was maintained at 3.0×10^{-3} Pa during the film deposition. A KrF excimer laser beam (λ = 420 nm; pulse duration = 20 ns; repetition frequency = 10 Hz) was focused through a SiO_2 glass window onto a rotating ZnO ceramic target to produce a photon energy density of ~1 J cm^{-2} pulse. Facing the target, the YSZ substrate (10 mm × 10 mm × 0.5 mm thick) was rotated mechanically and kept at 300°C during film growth.

Prior to the TE measurements, the sintered ceramics were cut and polished to obtain the required shapes and sizes. For the electrical measurements, the samples were cut into rectangular bars with the dimensions of 2.5 mm × 2.5 mm × 7.5 mm from the sintered pellets. On the other hand, for the thermal conductivity measurements, the samples were cut into square sheets with the dimensions of 5 mm × 5 mm × 1 mm. For both the measurements, the samples were cut along the direction parallel to the sintering pressing axis. The electrical conductivity (σ) and Seebeck coefficient (S) values of the samples were measured simultaneously over the temperature range of 344–1046 K in an air atmosphere using a four-probe Seebeck measuring apparatus (RZ2001i, Ozawa Science, Japan). The thermal conductivity (κ) values were determined from the thermal diffusivity (α) and specific heat capacity (C_p) values, which were measured simultaneously using a laser flash technique (LFA-502, Kyoto Electronics Manufacturing, Japan) under vacuum over the temperature range of 373–1073 K. The absolute C_p values of the samples were determined by comparing their measured values and the standard C_P value of molybdenum as the reference. The C_p values were also calculated using the Dulong-Petit law [18]. Finally, the thermal conductivity of the samples was determined using Eq. (2).

$$\kappa = \alpha C_\mathrm{p} \rho \qquad (2)$$

where κ, α, C_p, and ρ represent the thermal conductivity, thermal diffusivity, specific heat capacity, and density of the sample, respectively.

3.3. Results and Discussion

3.3.1. In Single-doped ZnO

3.3.1.1. Crystal Phase

Figure 22 shows the XRD patterns of the finely pulverized powders obtained after the SPS of ZnO with various In concentrations. Most of the observed peaks for the $[Zn_{(1-y)}In_y]O$ samples (y = 0.005, 0.01, 0.02, 0.03, 0.05) could be assigned to those of pure ZnO as the primary phase with the wurtzite structure and the $P6_3mc$ (186) space group.

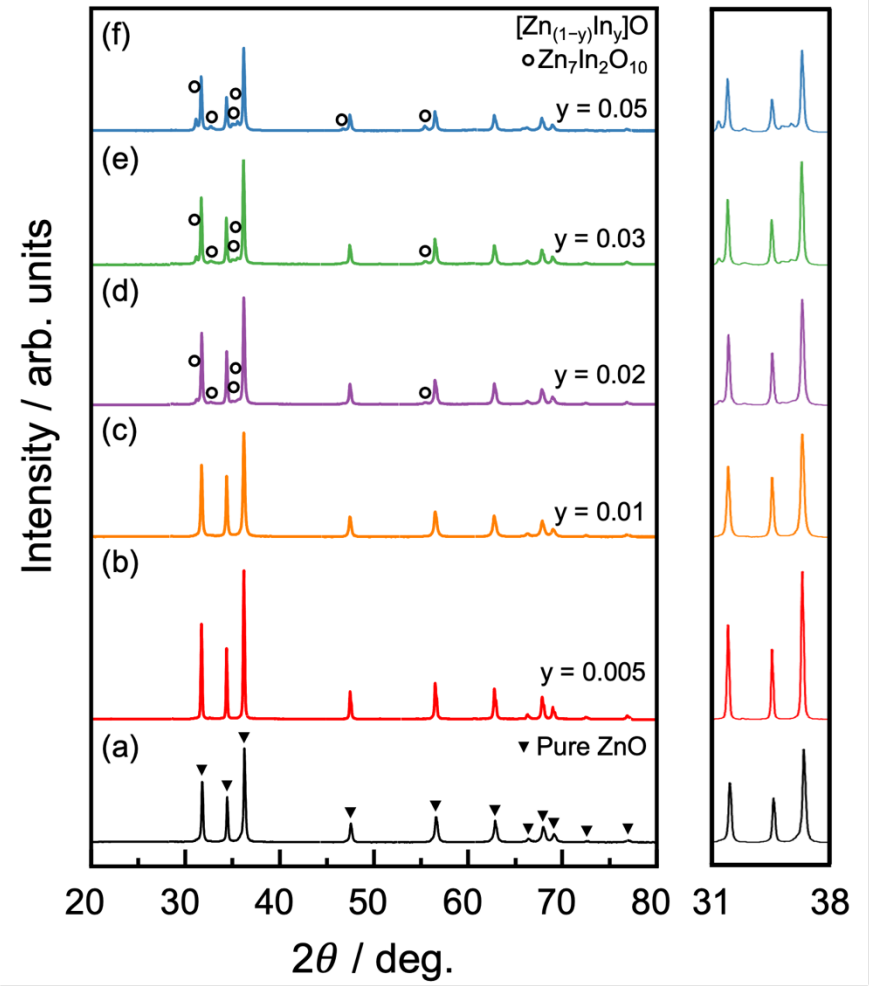

Fig. 22. Powder XRD patterns of (a) pure ZnO and the In single-doped $[Zn_{(1-y)}In_y]O$ sintered ceramics: y = (b) 0.005, (c) 0.01, (d) 0.02, (e) 0.03, and (f) 0.05. The right panel shows the expanded view over a range of 2θ = 31–38°.

The samples showed sharp and narrow peaks, indicating a good crystallinity and fairly large crystallite sizes. The impurity phases were detected in the XRD patterns of the single-doped ZnO samples ($y \geq 0.02$), exemplified as Fig. 22(d). The $Zn_7In_2O_{10}$ secondary phase was detected for the $[Zn_{(1-y)}In_y]O$ samples with $y = 0.02$. The intensity of the secondary phase peaks increased with increasing in y from 0.02 to 0.05, as shown in Fig. 22(d)–22(f). The appearance of the XRD peaks corresponding to $Zn_7In_2O_{10}$ is consistent with the results reported previously [19]. No secondary phase other than $Zn_7In_2O_{10}$ was detected for any of the samples, and the peak positions and relative peak intensities of the $[Zn_{(1-y)}In_y]O$ samples agreed with those of pure ZnO.

3.3.1.2. Microstructure and Phase Transition

The surface microstructures and the secondary phases of the In single-doped $[Zn_{(1-y)}In_y]O$ ($y = 0.005, 0.01, 0.02, 0.03, 0.05$) samples are shown in Fig. 23. The black, gray, and white areas in Fig. 23 represent the structural defects such as voids, the dense primary phase of In single-doped ZnO, and the secondary phases such as $Zn_7In_2O_{10}$ and the nonstoichiometric compounds Zn–In–O, respectively. To determine the chemical compositions of the phases, the EDS point analysis was performed at 20 points per each area distinguishable by the contrast in the BSE images marked as A, B, and C in Fig. 23(e), and the averaged compositions are shown in the table in Fig. 23. These results were consistent with the XRD results for $y = 0.05$ in Fig. 22(f).

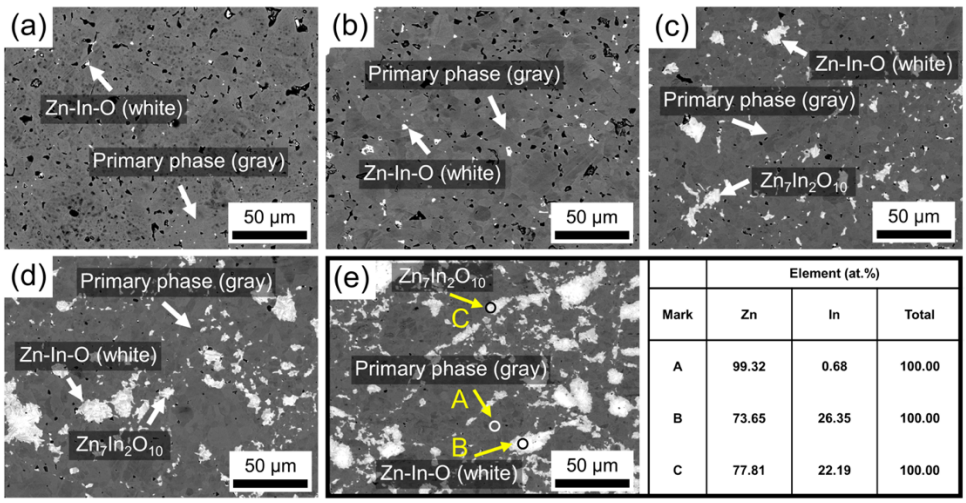

	Element (at.%)		
Mark	Zn	In	Total
A	99.32	0.68	100.00
B	73.65	26.35	100.00
C	77.81	22.19	100.00

Fig. 23. Microstructures of the polished surfaces of the In single-doped $[Zn_{(1-y)}In_y]O$ sintered ceramics: y = (a) 0.005, (b) 0.01, (c) 0.02, (d) 0.03, and (e) 0.05 in the BSE mode of SEM. The normalized atomic compositions of (e) marked as A, B, and C were measured using the EDS point analysis results.

The influence of the $Zn_7In_2O_{10}$ secondary phase on the TE properties of the samples is discussed in detail in section 3.3.3. Although pure ZnO exhibited a relative density of 91.3% lower than that of the In single-doped samples, all the doped samples showed high relative densities of ≥ 92.5% of the theoretical density of ZnO (5.61 g/cm^3), as shown in Table 4. This improvement in the relative density of the doped samples implies that an increase in the In_2O_3 amount (7.18 g/cm^3) [20] led to the formation of the secondary phases with higher theoretical density, suggesting that the doping conditions were insufficient for homogeneous distribution of In. However, In and Ga might serve as sintering aids in ZnO for densification, resulting in the increased relative density [7,21]. With an increase in y from 0 to 0.02, the Zn–In–O secondary phase appeared in the samples, and the $Zn_7In_2O_{10}$ phase seen as the white area in Fig. 23 started to appear at y = 0.02. In addition, when y increased from 0.02 to 0.05, the white area containing large amounts of In spread out as agglomerated clusters, as shown in Fig. 23(e).

Table 4. Relative densities of the single/dual-doped $[Zn_{(1-x-y)}Ga_xIn_y]O$ sintered ceramics with different compositions.

	Composition		Relative density (%)
Pure ZnO	x = 0	y = 0	91.3
Single-doped ZnO	x = 0	y = 0.005	92.5
	x = 0	y = 0.01	94.2
	x = 0	y = 0.02	98.0
	x = 0	y = 0.03	99.6
	x = 0	y = 0.05	100.0
Dual-doped ZnO	x = 0.005	y = 0.005	94.0
	x = 0.01	y = 0.005	96.3
	x = 0.02	y = 0.005	97.8
	x = 0.03	y = 0.005	99.5
	x = 0.05	y = 0.005	100.0

Figures 24(a)–24(e) show the EDS elemental mapping of In for the same viewing areas of the In single-doped $[Zn_{(1-y)}In_y]O$ (y = 0.005, 0.01, 0.02, 0.03, 0.05) samples shown in Fig. 23. The blue scale bar on the left side of the EDS maps indicates the relative concentration of In. When y increased from 0.005 to 0.01, the Zn–In–O secondary phase appeared. On the other hand, the $Zn_7In_2O_{10}$ phase started to appear when y increased from 0.01 to 0.02. The EDS elemental mapping confirmed the presence the $Zn_7In_2O_{10}$ phase in the samples. This is consistent with the results shown in Fig. 22 and Fig. 23.

The chemical composition of the primary phase, the matrix of the In single-doped ZnO, was estimated by carrying out the EDS point analysis. The values obtained from the 20 points on the matrix were averaged, and all the numbers were normalized to 100% excluding oxygen,

as shown in Table 5. The In content of the primary phase of the In-doped ZnO samples was 0.4–0.7 at.%. This indicates that In was still soluble in the ZnO matrix.

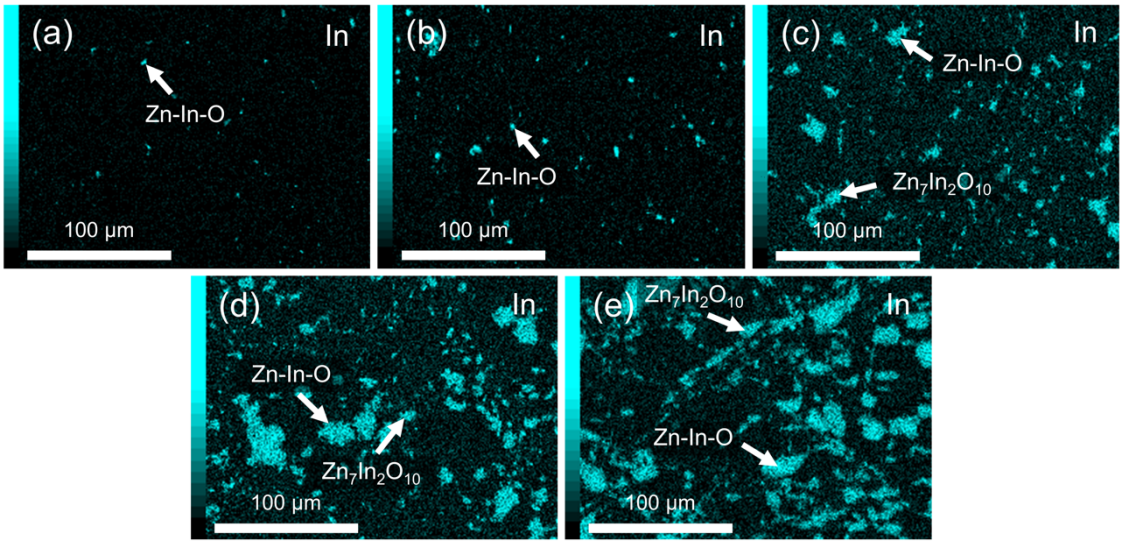

Fig. 24. EDS elemental mapping of In for the In single-doped $[Zn_{(1-y)}In_y]O$ sintered ceramics: y = (a) 0.005, (b) 0.01, (c) 0.02, (d) 0.03, and (e) 0.05.

3.3.2. In and Ga Dual-doped ZnO

3.3.2.1. Crystal Phase

The XRD patterns of pure ZnO and the In and Ga dual-doped $[Zn_{(1-x-y)}Ga_xIn_y]O$ (y = 0.005; x = 0.005, 0.01, 0.02, 0.03, 0.05) samples are shown in Fig. 25. All the samples have pure ZnO as the primary phase, and impurity phase peaks were observed for the samples with $x \geq 0.02$, as shown in Fig. 25(b)–25(f). The sample with x = 0.02, y = 0.005 showed a secondary $ZnGa_2O_4$ spinel phase, as shown in Fig. 25(d). The $ZnGa_2O_4$ phase often appears in Ga-doped ZnO and disappears at the sintering temperature of 1473 K [22]. Moreover, the limited solubility of Ga atoms (1 at.%) in the ZnO matrix can also lead to the formation of this phase. This is consistent with the low Ga content of the Ga-doped ZnO samples in this study with the Ga amounts exceeding the solubility limit [23,24]. The peaks corresponding to the $ZnGa_2O_4$

secondary phase increased their intensity with increasing x from 0.02 to 0.05, as shown in Fig. 25(d)–25(f), and the $Zn_7In_2O_{10}$ phase appeared at x = 0.05. In a previous paper, the $ZnGa_2O_4$ phase (x = 0.02) disappeared with increasing y from 0.005 to 0.02 since In promotes the solubility of Ga even Ga already exceeded solubility limit in the ZnO matrix [7]. On the other hand, the $ZnGa_2O_4$ phase existed x from 0.02 to 0.05 due to the low amount of In (y = 0.005), thus, In contributed to form $Zn_7In_2O_{10}$ phase at a high amount of Ga (x = 0.05) in this present study.

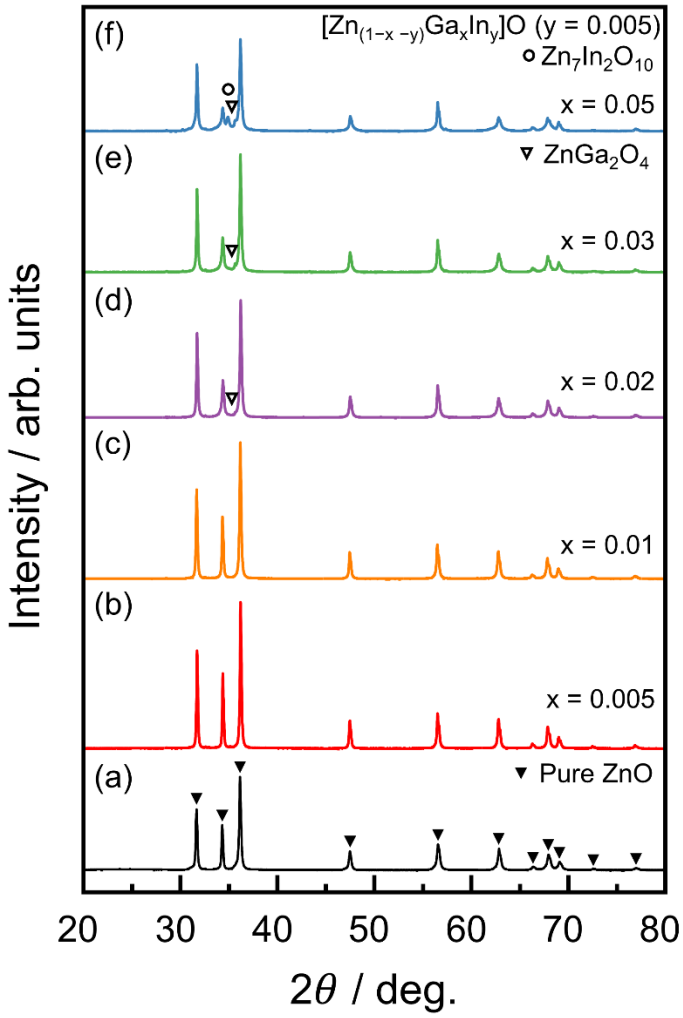

Fig. 25. Powder XRD patterns of (a) pure ZnO, and the In and Ga dual-doped $[Zn_{(1-x-y)}Ga_xIn_y]O$ sintered ceramics: y = 0.005; x = (b) 0.005, (c) 0.01, (d) 0.02, (e) 0.03, and (f) 0.05.

The $Zn_7In_2O_{10}$ phase has been reported that in the $ZnO–In_2O_3$ binary system the end member oxides react with each other above 1273 K, and there is a series of homologous compounds with the compositions given by $Zn_kIn_2O_{k+3}$, where k is an integer. In the previous study, $Zn_7In_2O_{10}$ formed at $k = 7$ and 1423 K [25,26], and this is in good agreement with the results in this study. Moreover, the decrease in the (002) peak intensity at approximately $2\theta = 34.4°$ (Fig. 25(d)–25(f)) indicates that a significant anisotropy occurred in In and Ga dual-doped ZnO [8].

3.3.2.2. Microstructure and Phase Transition

The BSE images of the In and Ga dual-doped $[Zn_{(1-x-y)}Ga_xIn_y]O$ samples (y = 0.005; x = 0.005, 0.01, 0.02, 0.03, 0.05) are shown in Fig. 26. The black, gray, and white areas represent the structural defects such as voids, the dense primary phase of In and Ga dual-doped ZnO, and the secondary phases such as $ZnGa_2O_4$ and the nonstoichiometric compounds Zn–In–Ga–O, respectively. At x = 0.005–0.03, only the Zn–In–Ga–O phase was observed in the BSE images (Fig. 26). However, a small amount of the $ZnGa_2O_4$ secondary phase appeared at x = 0.02 and 0.03 in XRD (Fig. 25(d) and 25(e)). To determine the chemical compositions of the $Zn_7In_2O_{10}$ and $ZnGa_2O_4$ secondary phases, the EDS point analysis was performed at 20 points each in the areas with the same contrast in the BSE images, and the compositional data were averaged within each contrast (marked as C and D in Fig. 26(e)). The results were consistent with the XRD results for x = 0.05 (Fig. 25(f)). The In and Ga dual-doped samples showed a high relative density of ≥ 94.0%, as listed in Table 4. This high relative density can be attributed to the increase in the In_2O_3 (7.18 g/cm^3) and Ga_2O_3 (6.44 g/cm^3) [20] amounts, which contributed to the formation of the secondary phase. The relative density of the In and Ga dual-doped ZnO ceramics reached 94.0–100%, which is higher than that reported in a previous study (79.8–91.0%) [13]. The reason for the high relative density achieved in this study is presumably the

use of SPS to achieve a densified microstructure with a short consolidation time by suppressing the grain-growth [7,27], which contributed to the improvement in the *ZT* of the samples.

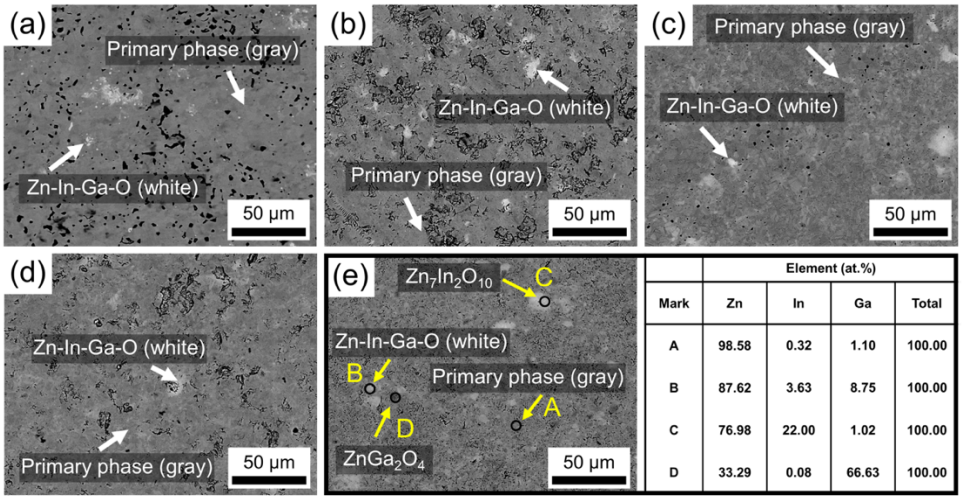

	Element (at.%)			
Mark	Zn	In	Ga	Total
A	98.58	0.32	1.10	100.00
B	87.62	3.63	8.75	100.00
C	76.98	22.00	1.02	100.00
D	33.29	0.08	66.63	100.00

Fig. 26. Microstructures of the polished surfaces of the In and Ga dual-doped $[Zn_{(1-x-y)}Ga_xIn_y]O$ sintered ceramics: y = 0.005; x = (a) 0.005, (b) 0.01, (c) 0.02, (d) 0.03, and (e) 0.05 in the BSE mode of SEM. The normalized atomic compositions of (e) marked as A, B, C, and D were measured using the EDS point analysis results.

The EDS elemental mapping of In and Ga for the In and Ga dual-doped $[Zn_{(1-x-y)}Ga_xIn_y]O$ (y = 0.005; x = 0.005, 0.01, 0.02, 0.03, 0.05) ceramics is shown in Fig. 27. The blue color scale bars on the left sides of the EDS maps indicate the relative concentration of In. The relative concentration of Ga in the same area are shown as the inset of each panel in a pink color. When x increased from 0.005 to 0.03, the Zn–In–Ga–O secondary phase appeared, while the $Zn_7In_2O_{10}$ and $ZnGa_2O_4$ phases appeared only at x = 0.05. In addition, the degree of agglomeration of Ga increased with increasing amount of Ga, especially when $x \geq 0.02$. This indicates that the amount of Ga exceeded the solubility limit in the ZnO matrix. The EDS elemental mapping confirmed the presence of the $Zn_7In_2O_{10}$ and $ZnGa_2O_4$ phases (Fig. 27(e)). This is consistent with the results shown in Fig. 25(f). Moreover, the agglomerated clusters of

In decreased as compared to those of In single-doped ZnO, as shown in Fig. 24, implying that Ga promotes the homogeneous doping of In in the ZnO matrix.

The chemical composition of the primary phase in In and Ga dual-doped ZnO was analyzed as listed in Table 5, and the maximum Ga concentration was determined as 0.8 at.% for the sample with x = 0.01 and y = 0.005, which showed the highest solubility among the dual-doped samples.

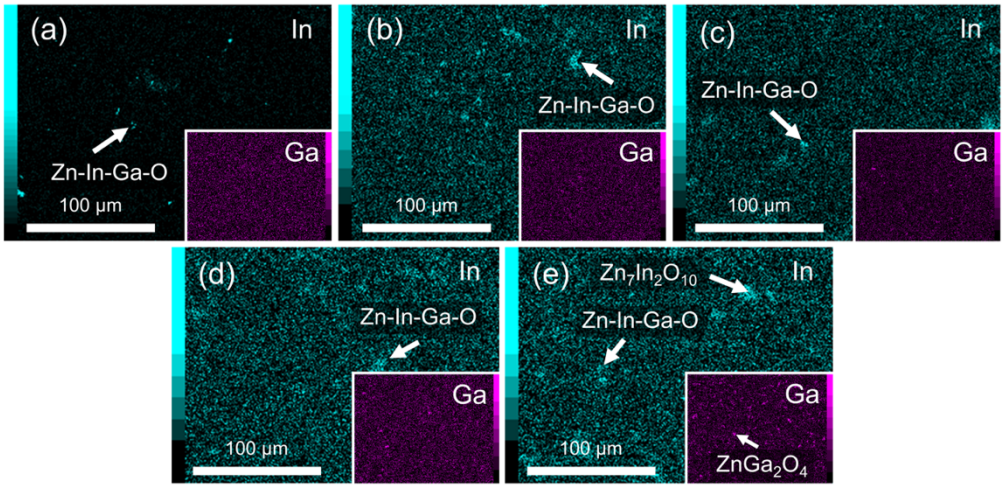

Fig. 27. EDS elemental mapping of In and Ga for the In and Ga dual-doped $[Zn_{(1-x-y)}Ga_xIn_y]O$ sintered ceramics: y = 0.005; x = (a) 0.005, (b) 0.01, (c) 0.02, (d) 0.03, and (e) 0.05. The relative concentration of Ga in the same area are shown as the inset of each panel in a pink color.

3.3.3. Thermoelectric Properties of Single/Dual-doped ZnO

Figure 28 shows the temperature dependence of the electrical conductivity (σ), the Seebeck coefficient (S), and the power factor (PF, $S^2\sigma$) of the samples. The Pisarenko relation given in Eq. (3) prevents a simultaneous increase of both σ and S (a trade-off relationship),

$$|S| = \frac{8\pi^2 k_B^2}{3eh^2} m^* T \left(\frac{\pi}{3n}\right)^{2/3} \qquad (3)$$

where k_B is the Boltzmann constant, e is the electron charge, h is the Planck constant, m^* is the effective mass of the carrier, T is the absolute temperature, and n is the carrier concentration. Pure ZnO shows an electrical conductivity of 4.2×10^{-2}–2.0 S cm^{-1} over the temperature range of 344–1046 K, exhibiting a semiconducting behavior, as shown in Fig. 28(a).

Table 5. Chemical composition of the primary phase of the single/dual-doped $[Zn_{(1-x-y)}Ga_xIn_y]O$ ceramics, as estimated from the EDS point analysis results. The composition was normalized oxygen by setting the total to 100.

Type of doping	Composition		Chemical composition (at.%)			Total
			Zn	Ga	In	
Single doping	x = 0	y = 0.005	99.6(3)		0.4(3)	100
	x = 0	y = 0.01	99.6(3)		0.4(3)	100
	x = 0	y = 0.02	99.5(3)		0.5(3)	100
	x = 0	y = 0.03	99.4(3)		0.6(3)	100
	x = 0	y = 0.05	99.3(3)		0.7(3)	100
Dual doping	x = 0.005	y = 0.005	99.3(4)	0.4(3)	0.3(2)	100
	x = 0.01	y = 0.005	98.9(5)	0.8(5)	0.3(1)	100
	x = 0.02	y = 0.005	99.3(4)	0.6(4)	0.1(1)	100
	x = 0.03	y = 0.005	99.5(8)	0.3(6)	0.2(3)	100
	x = 0.05	y = 0.005	99.4(4)	0.3(4)	0.3(2)	100

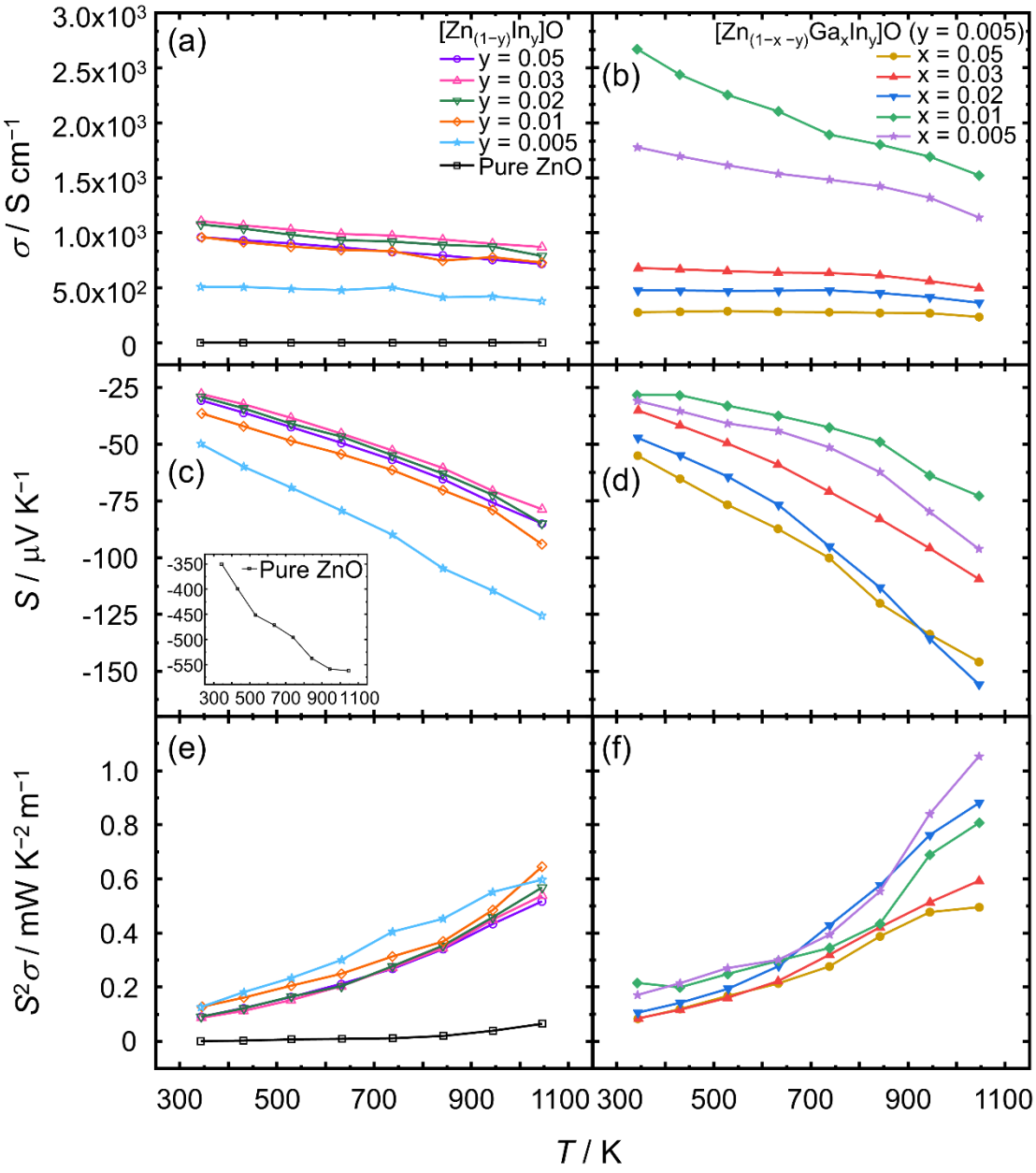

Fig. 28. Temperature dependence of (a, b) the electrical conductivity σ, (c, d) the Seebeck coefficient S, and (e, f) the power factor $S^2\sigma$: (a), (c), and (e) of pure ZnO and the In single-doped ZnO, and (b), (d), and (f) of the In and Ga dual-doped ZnO sintered ceramics, respectively. The S of pure ZnO is given in the inset of (c).

On the other hand, the single/dual-doped ZnO samples showed very high electrical conductivities as high as 2.8×10^2–2.7×10^3 S cm^{-1} exhibiting a metal-like behavior, in which the electrical conductivity decreases monotonically with increasing temperature, as shown in Fig. 28(a) and 28(b). These results clearly proved the efficient carrier injection by the In and Ga doping. The In single-doped ZnO samples with y = 0.02, 0.03, 0.05, which contained the $Zn_7In_2O_{10}$ secondary phase, showed higher electrical conductivity than that of the sample with y = 0.005. It has been reported that the electrical conductivity of $Zn_kIn_2O_{k+3}$ increases with decreasing *k*, which corresponds to higher In-doping in ZnO [28,29]. Hence, it is suggested that the formation of the $Zn_7In_2O_{10}$ phase contributes to increase the electrical conductivity of the samples. The In and Ga dual-doped ZnO (y = 0.005; x = 0.02, 0.03, 0.05) samples containing the $ZnGa_2O_4$ phase showed low electrical conductivity values at 344 K, which are 4–10 times lower than that of the sample with x = 0.01 because of the segregation of the $ZnGa_2O_4$ phase [30]. Furthermore, the sample with x = 0.05 and y = 0.005 showed the lowest electrical conductivity among all the doped ZnO samples as 2.8×10^2–2.3×10^2 S cm^{-1} because of its high $ZnGa_2O_4$ content, as shown in Fig. 25(f) and Fig. 27(e). The samples with x = 0.005, y = 0.005 and x = 0.01, y = 0.005 showed the highest electrical conductivities of 1.8×10^3–1.1×10^3 and 2.7×10^3–1.5×10^3 S cm^{-1}, respectively. The high electrical conductivities of these samples as compared to that of the single-doped ZnO can be attributed to their increased carrier concentration and carrier mobility [15] and the absence of the secondary phase. The comparison of the highest electrical conductivity between the previous and present studies shows 2.03×10^3 S cm^{-1} and 1.52×10^3 S cm^{-1} at 1046 K. In this study, a high electrical conductivity of 1.9×10^3 S cm^{-1} was achieved at 773 K, as compared to the previously reported value of approximately 700 S cm^{-1} [13,30], presumably being attributed to the high relative density of the samples. Figures 28(a, b) and 28(c, d) show that a trade-off relationship exists between the electrical conductivity and the absolute value of the Seebeck coefficient ($|S|$), and

|*S*| increased with increasing temperature. As the carrier concentration increased, |*S*| decreased as indicated by Eq. (3). The *S* of pure ZnO at 1046 K was –560 μV K^{-1}, while that of the sample with x = 0.01 and y = 0.005 was –70 μV K^{-1}. The *PF* values of pure ZnO and the In single-doped ZnO ceramics were 6.4 × 10^{-2} and 5.2 × 10^{-1}–6.5 × 10^{-1} mW K^{-2} m^{-1}, respectively, as shown in Fig. 28(e). Besides, the *PF* values of the In and Ga dual-doped samples with x = 0.005, 0.01, 0.02 and y = 0.005 improved considerably as compared to those of pure ZnO and the In single-doped samples, as shown in Fig. 28(f). The highest *PF* value of 1.1 mW K^{-2} m^{-1} was achieved for the sample with x = 0.005 and y = 0.005 at 1046 K in the present study, but the highest *PF* value was attained 0.99 mW K^{-2} m^{-1} for the sample with x = 0.02 and y = 0.005 in the previous study [7]. From this result, it is noticed that the decrease of Ga affected to achieving a slightly high *PF* value. The In and Ga dual-doped ZnO samples thereby showed higher *PF* than those of the pure ZnO and In single-doped ZnO samples because of their high electrical conductivity. Hence, it can be stated that substituting Zn sites with In and Ga is a promising approach for tuning the carrier concentration of ZnO to increase its *PF* [31].

Figure 29 shows the total thermal conductivity, which consists of the electron and lattice thermal conductivities of the samples. The energy conversion efficiency and *ZT* of a TE material are related as Eq. (1). The temperature dependence of the thermal conductivity of pure ZnO and the single/dual-doped $[Zn_{(1-x-y)}Ga_xIn_y]O$ (y = 0.005; x = 0.005, 0.01, 0.02, 0.03, 0.05) samples is shown in Fig. 29. The total thermal conductivities of all the samples investigated in this study are shown in Fig. 29(a) and 29(b). The thermal conductivity of the samples decreased substantially with increasing temperature. The thermal conductivity of a TE material is affected by several factors, such as the nanostructured grain or particle size, nanolayer, relative density, point defects, porosity, and temperature [32–34]. An inverse relationship exists between the lattice thermal conductivity and absolute temperature of crystalline materials around and above room temperature, i.e., the lattice thermal conductivity decreases with increasing temperature

due to increasing phonon-phonon scattering at higher temperatures. The In and Ga single/dual-doped samples showed the reduced total thermal conductivity at 344 K as compared to pure ZnO.

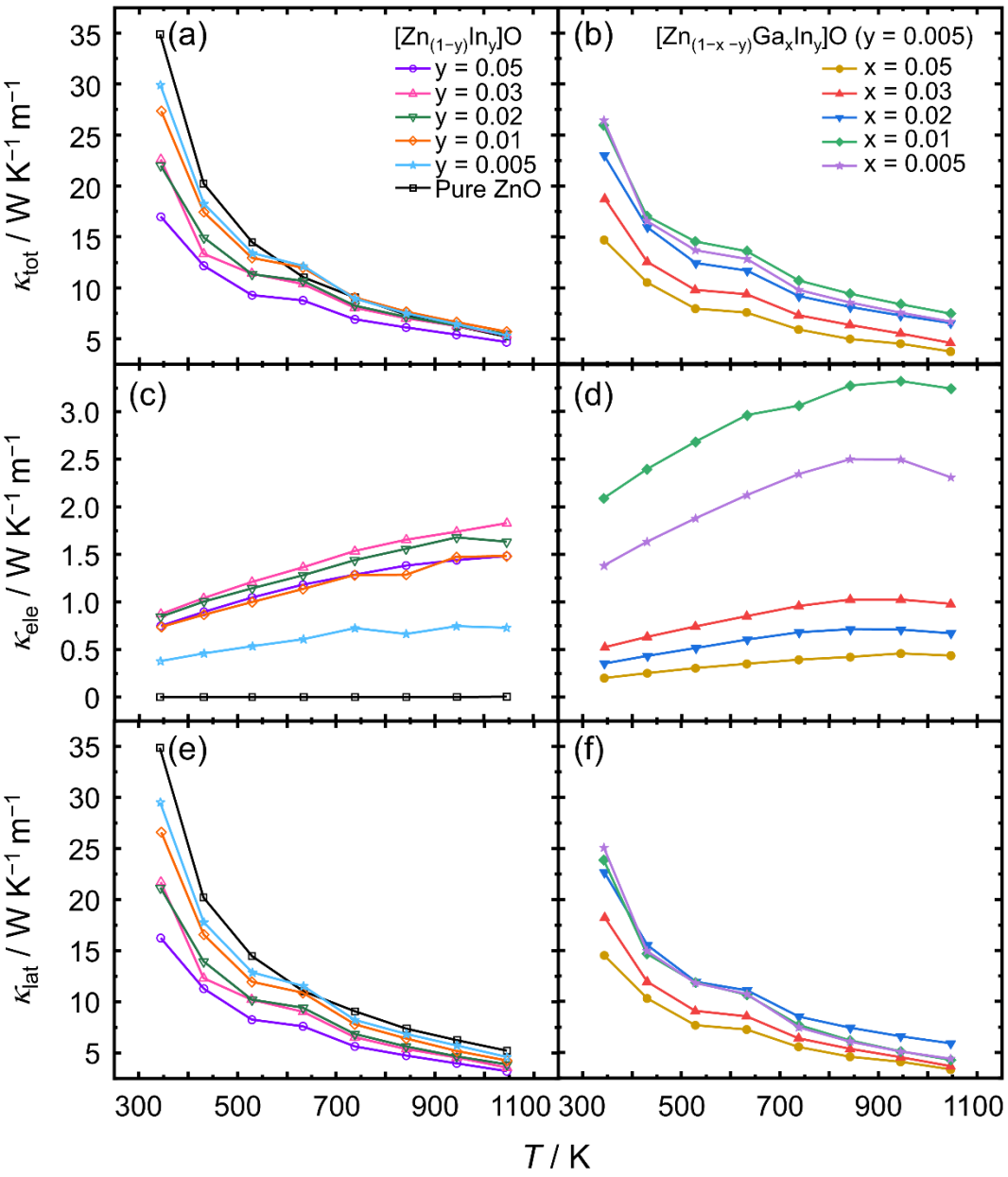

Fig. 29. Temperature dependence of (a, b) the total thermal conductivity κ_{tot}, (c, d) the electron thermal conductivity κ_{ele}, and (e, f) the lattice thermal conductivity κ_{lat} are shown: (a), (c), and (e) of pure ZnO and the In single-doped ZnO, and (b), (d), and (f) of the In and Ga dual-doped ZnO sintered ceramics, respectively.

At 344 K, pure ZnO showed a high total thermal conductivity of 35 W K^{-1} m^{-1}, which decreased dramatically to 15 W K^{-1} m^{-1} after the substitution of Zn sites by In and Ga at x = 0.05 and y = 0.005. The sample with x = 0.05 and y = 0.005 showed the lowest thermal conductivity of 4 W K^{-1} m^{-1} at 1046 K among all the dual-doped samples in the present study, and the lowest thermal conductivity of 6 W K^{-1} m^{-1} at 1046 K was attained in the previous study [7]. This suggests that the $Zn_7In_2O_{10}$ phase reduced the lattice thermal conductivity of the sample. The lattice thermal conductivity decreases with decreasing grain size of a material [35]. Various efforts have been made to prevent the grain-growth to enhance the phonon scattering and reduce the thermal conductivity. The electron and lattice thermal conductivities of the samples are shown in Fig. 29(c, d) and 29(e, f), respectively. The electron thermal conductivity decreased with increasing in temperature above 944 K, as shown in Fig. 29(d). This is due to the almost linear decrease in σ (Fig. 28(b)) multiplied by the linear contribution of T in the Wiedemann–Franz law in Eq. (4), resulting in a decreasing tendency of κ_{ele} at the highest temperature region [36].

$$\kappa_{ele} = L\sigma T \qquad (4)$$

where the κ_{ele} is the electron thermal conductivity, L is the Lorentz number, σ is the electrical conductivity, and T is the absolute temperature. It has been reported that errors occur in the calculation of the Lorentz number when the TE material has a Seebeck coefficient lower than 50 μV K^{-1} [37,38]. In such cases, the Lorentz number should be recalculated, following the equation in the literature [38].

$$L = 1.5 + \exp\left[-\frac{|S|}{116}\right] \qquad (5)$$

Figures 29(e) and 29(f) shows the lattice thermal conductivity of the samples, as calculated from their total thermal conductivity and electron thermal conductivity ($\kappa_{lat} = \kappa_{tot} - \kappa_{ele}$). The electron thermal conductivity of a TE material is affected by its carrier concentration; however, the lattice thermal conductivity depends on the crystal structure of the material. Regarding the predominance of the thermal conductivity at different temperatures, the lattice thermal conductivity was dominant at 344 K; however, the electron and thermal conductivities at 1046 K were comparable, as shown in Fig. 29(c, d) and 29(e, f). As a result, the small and large fluctuations in the electron conductivity caused a non-monotonic reduction in the lattice thermal conductivity at low temperatures and a monotonic reduction at high temperatures, respectively.

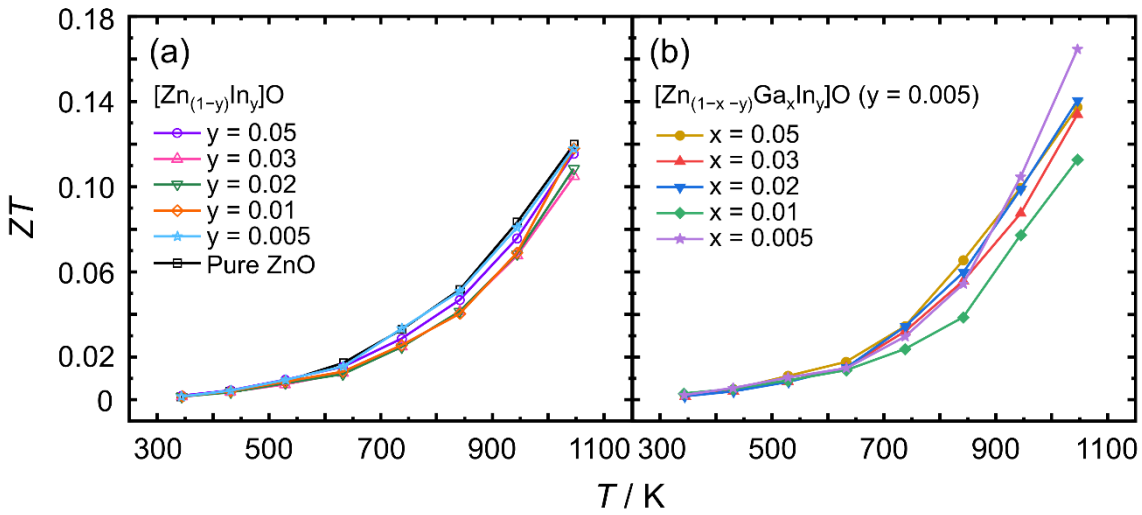

Fig. 30. Dimensionless figure of merit *ZT* of (a) pure ZnO and the In single-doped ZnO, and (b) the In and Ga dual-doped ZnO sintered ceramics.

Figure 30 shows the *ZT* values of the samples, as calculated from their electrical conductivity, Seebeck coefficient, and total thermal conductivity. The In and Ga dual-doped ZnO samples (y = 0.005; x = 0.005, 0.02, 0.03, 0.05) showed high *ZT* values. Although the sample with x = 0.05 and y = 0.005 showed the lowest total thermal conductivity of 4 W K^{-1}

m^{-1}, the sample with x = 0.005 and y = 0.005 showed the highest *PF* of 1.1 mW K^{-2} m^{-1}. Thus, the sample with x = 0.005 and y = 0.005 showed the highest *ZT* value of 0.17 at 1046 K because the *PF* value was dominant rather than the total thermal conductivity, as shown in Fig. 30(b). It should be noted that this *ZT* value is higher than that obtained in a previous study (*ZT* = 0.15 at 1046 K) [7]. In addition, in a previous study, the Ga single-doped sample (2 at.%) [7] showed a *ZT* value (0.21 at 1046 K) higher than that of the In single-doped sample (2 at.%) (0.11 at 1046 K). All the single-doped ZnO samples in this study showed the *ZT* values lower than 0.12, indicating that In doping alone was insufficient to increase *ZT* of ZnO as it led to the formation of an agglomerated Zn–In–O secondary phase as shown in Fig. 24.

3.3.4. Crystal Phase and Electrical Conductivity of Single/Dual-doped Nanosized ZnO

Figure 31 shows the XRD patterns of the after the SPS of nanosized pure ZnO, and In and Ga doped $[Zn_{(1-x-y)}Ga_xIn_y]O$ (y = 0.005; x = 0.005, 0.01, 0.02, 0.03, 0.05) with various Ga concentrations. All the samples could be assigned to those of pure ZnO as the primary phase, and secondary phase peaks were observed for the samples with $x \geq 0.01$, as shown in Fig. 31(c)–31(f).

The sample with x = 0.01, y = 0.005 showed a secondary $ZnGa_2O_4$ spinel phase, as shown in Fig. 31(c). The $ZnGa_2O_4$ phase often appears in Ga-doped ZnO ,and the limited solubility of Ga atoms (1 at.%) in the ZnO lead to the formation of this phase. This is almost consistent with the low Ga content of the Ga-doped ZnO samples in this study with the Ga dopants exceeding the solubility limit [23]. The peaks corresponding to the $ZnGa_2O_4$ secondary phase increased their intensity with increasing x from 0.01 to 0.05, as shown in Fig. 31(c)–31(f).

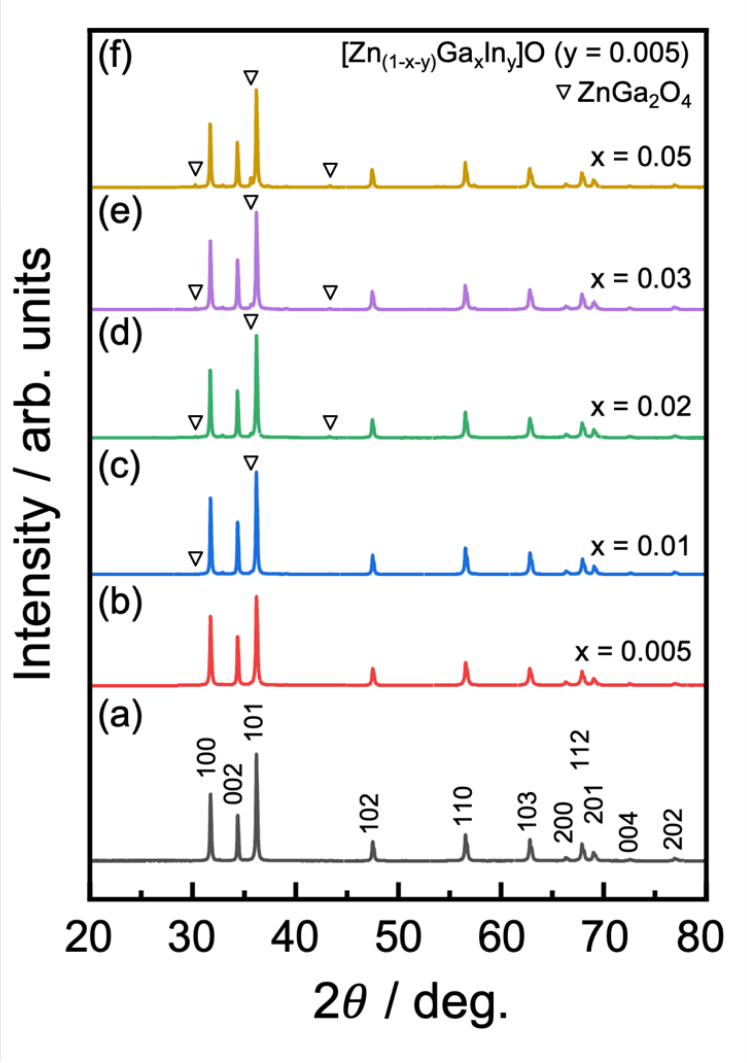

Fig. 31. Powder XRD patterns of nanosized (a) pure ZnO, and the In and Ga dual-doped $[Zn_{(1-x-y)}Ga_xIn_y]O$ sintered ceramics: y = 0.005; x = (b) 0.005, (c) 0.01, (d) 0.02, (e) 0.03, and (f) 0.05.

Figure 32 shows the temperature dependence of the electrical conductivity (σ), the Seebeck coefficient (S), and the power factor (PF, $S^2\sigma$) of the samples. Pure ZnO shows an electrical conductivity of 48–26 S cm^{-1} over the temperature range of 70–775°C, exhibiting a semiconducting behavior, as shown in Fig. 32(a).

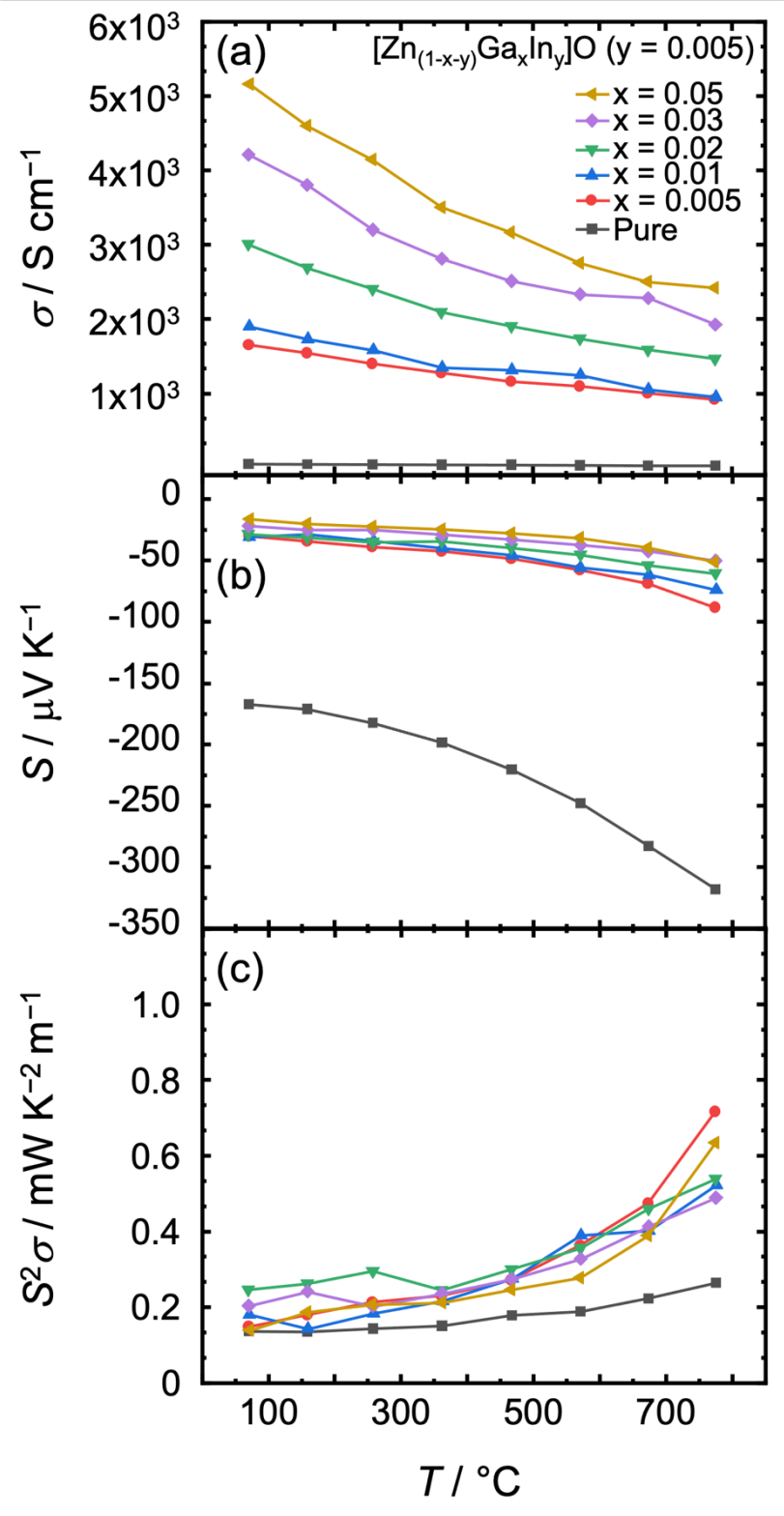

Fig. 32. Temperature dependence of the (a) electrical conductivity (σ), (b) Seebeck coefficient (S), and (c) power factor $S^2\sigma$ of nanosized $[Zn_{(1-x-y)}Ga_xIn_y]O$ (y = 0.005; x = 0.005, 0.01, 0.02, 0.03, 0.05) and pure ZnO.

3.3.5. Thin Films of In and Ga Dual-doped ZnO

Atomic force microscopy (AFM) surface images of the ZnO epitaxial films on an YSZ (111) substrate are shown in Fig. 33. The AFM images for the ZnO epitaxial films shows varied the concentration of Ga from x = 0.005–0.05. The grain size became smaller through the increasing of Ga. All the films has nanoscale corrugation, and the rms roughness is as large as 100 nm. It was found that the thickness of the In and Ga doped ZnO epitaxial layer, as evaluated using a high-resolution X-ray diffraction. The tendency of changed grain size occurs boundary scattering.

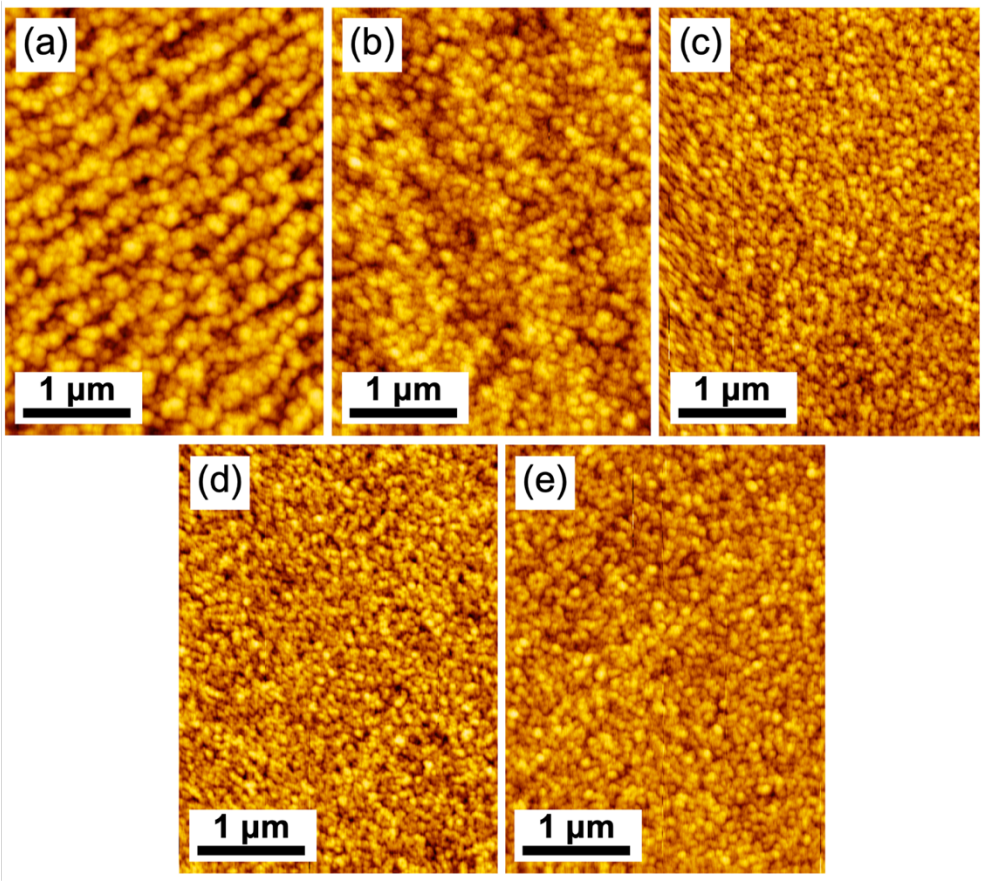

Fig. 33. AFM images of $[Zn_{(1-x-y)}Ga_xIn_y]O$ (y = 0.005), (a) x = 0.005, (b) x = 0.01, (c) x = 0.02, (d) 0.03, and (e) 0.05 ZnO epitaxial layer on YSZ (111).

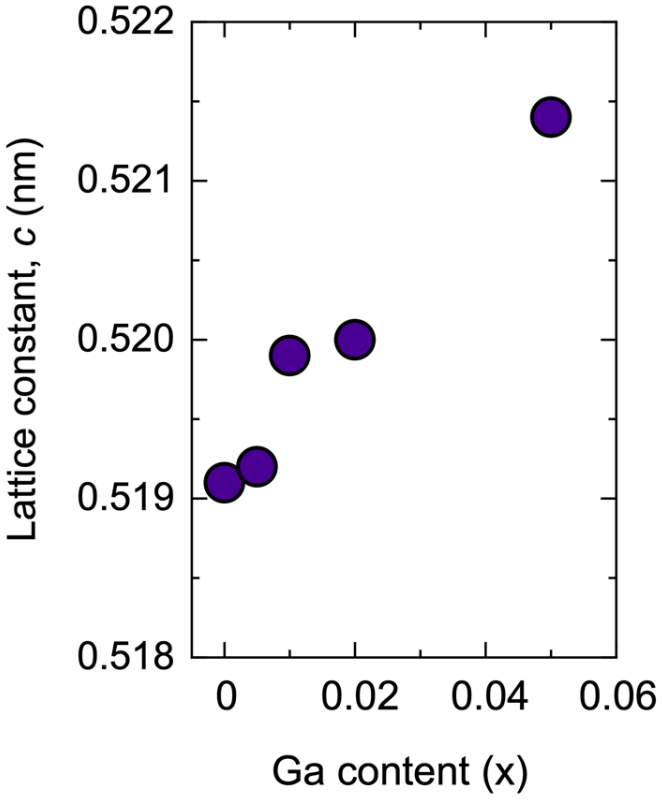

Fig. 34. Lattice constant with respect to the nominal concentration of $[Zn_{(1-x-y)}Ga_xIn_y]O$ (y = 0.005; x = 0.005, 0.01, 0.02, 0.05) and pure ZnO.

The lattice constants of In- and Ga-doped ZnO and pure ZnO, which were slightly changed by doping with different amounts of Ga, were investigated after Rietveld refinement, as shown in Fig. 34. The lattice constant of the non-substituted pure ZnO was c = 5.210 Å, which is in agreement with previous observations [39]. As the content of In increased from y = 0.005 to 0.05, the lattice constants c continuously increased, indicating the substitution of Ga^{3+} into the ZnO matrix. The lattice constants of the In- and Ga-substituted specimens were within 0.1% difference of those of pure ZnO. Because the ionic radii of In^{3+}, Ga^{3+}, and Zn^{2+} are similar, it is expected that In^{3+} and Ga^{3+} can substitute Zn^{2+} in the ZnO matrix. Moreover, The lattice constant values for ZnO can be calculated, and it is written as $c_f = 2d_{002} = \lambda/\sin\theta$ [40]. In the ZnO film, residual stress is generated by a difference between a lattice constant and a thermal

expansion coefficient between the film and the substrate. The residual stress of the ZnO film can be calculated as follows: $\varepsilon = [2C^2_{13} - C_{33}(C_{11} + C_{12})/2C_{13}] \times [(c_f - c_o)/c_o]$, C_{ij} is the elastic stiffness constant for ZnO (C_{11} = 209.7, C_{33} = 210.9, C_{12} = 121.1, and C_{13} = 105.1 GPa), and c_f and c_o = 0.52 nm are the lattice parameters of the ZnO films and strain-free ZnO bulk, respectively. If the stress is positive, the biaxial stress becomes tensile. On the other hand, if the stress is negative, the biaxial stress is compressive. Accordingly, the stress values calculated from ZnO, GZO (Ga-doped ZnO), and IGZO (In and Ga-doped ZnO) films mean that all deposited films are subjected to compressive stress [40].

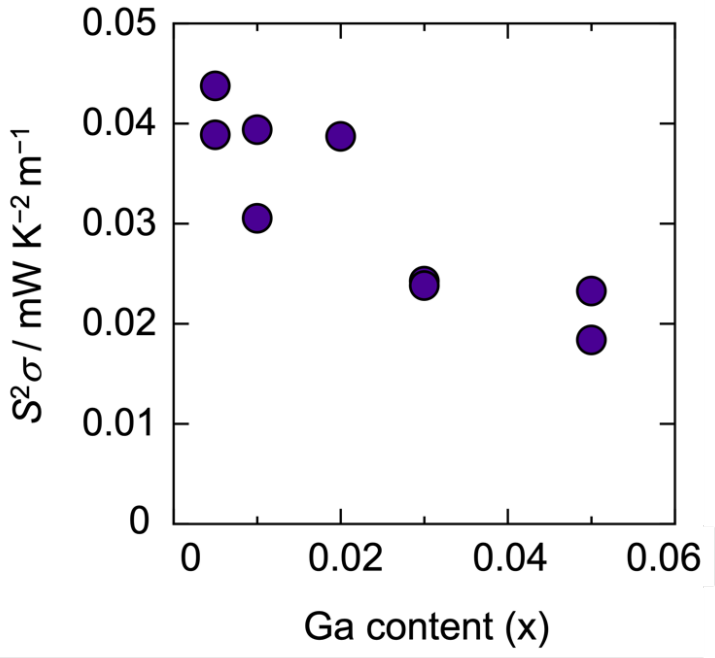

Fig. 35. The power factor $S^2\sigma$ with respect to the nominal concentration of $[Zn_{(1-x-y)}Ga_xIn_y]O$ (y = 0.005; x = 0.005, 0.01, 0.02, 0.03, 0.05).

The *PF*, showing the electrical contribution to the thermoelectric performance was calculated from the results. The *PF* values of In and Ga dual-doped ZnO ceramics were 4.4 × 10^{-2}–1.8 × 10^{-2} mW K^{-2} m^{-1}, respectively as Ga content increased (Fig. 35). Besides, the *PF*

values of the In and Ga dual-doped samples with x = 0.005, 0.01, 0.02, 0.03, 0.05 and y = 0.005 slightly decreased. It seems that Ga^{3+} ion is substitute in ZnO matrix well but the Ga^{3+} dose not contribute to increase carrier by doping. The lower *PF* value of 3.9×10^{-2} mW K^{-2} m^{-1} at 300°C from In and Ga dual-doped sample with x = 0.02 and y = 0.005 was achieved compared with a *PF* value of 3.3×10^{-1} mW K^{-2} m^{-1} from same composition but different size of starting materials (< 500 nm) at 300°C in previous study [41]. It is concluded that the size effect of starting material still unclear in TE properties since the thermal conductivity has not been conducted yet.

3.4. Conclusions

In the present study, sintered bodies of In single-doped $[Zn_{(1-y)}In_y]O$ (y = 0.005, 0.01, 0.02, 0.03, 0.05), and In and Ga dual-doped $[Zn_{(1-x-y)}Ga_xIn_y]O$ (y = 0.005; x = 0.005, 0.01, 0.02, 0.03, 0.05) ZnO ceramics were consolidated via SPS at 1423 K, and the influence of the In and Ga doping on the TE properties of the ceramics was investigated. The microstructural and chemical composition analyses indicated the presence of $Zn_7In_2O_{10}$ and $ZnGa_2O_4$ as the secondary phases in the single-doped ($y \geq 0.02$) and dual-doped ($y = 0.005$; $x \geq 0.02$) ZnO ceramics, respectively. The single and dual doping in this study increased the relative density of ZnO to 92.5–100%.

The highest power factor of 1.1 mW K^{-2} m^{-1} was achieved for the dual-doped $[Zn_{(1-x-y)}Ga_xIn_y]O$ sample with x = 0.005 and y = 0.005. However, the lowest total thermal conductivity of 4 W K^{-1} m^{-1} at 1046 K was achieved for the dual-doped $[Zn_{(1-x-y)}Ga_xIn_y]O$ sample with x = 0.05 and y = 0.005. Hence, the substitution of Zn by In and Ga is a promising approach to increase the *PF* values of ZnO by tuning its carrier concentration. Therefore, in this study, the In and Ga dual doping of ZnO was beneficial in improving its TE performance and achieving the maximum *ZT* of 0.17 at 1046 K.

To study on the effect of In and Ga dual-doped nanosized ZnO, different types of bulk and thin film of ZnO were fabricated with the same composition above. In the case of bulk ZnO, a secondary $ZnGa_2O_4$ spinel phase appeared from x = 0.01 to 0.05. And, in the case of thin film of ZnO, Ga succeeded to be substituted up to x = 0.05 in ZnO matrix but does not increase carrier concentration, contributing to *PF*.

References

[1] L.E. Bell, Cooling, heating, generating power, and recovering waste heat with Thermoelectric Systems, Science 321 (2008) 1457–1461.

[2] T. Mori, S. Priya, Materials for energy harvesting: At the forefront of a new wave, MRS Bull. 43 (2018) 176–180.

[3] G.J. Snyder, A.H. Snyder, Figure of merit ZT of a thermoelectric device defined from materials properties, Energy Environ. Sci. 10 (2017) 2280–2283.

[4] T. Tsubota, M. Ohtaki, K. Eguchi, H. Arai, Thermoelectric properties of ZnO doped with the group 13 elements, in: Proceedings of the 16th International Conference on Thermoelectrics, IEEE, Piscataway, (1997) 240–243.

[5] T. Tsubota, M. Ohtaki, K. Eguchi, H. Arai, Transport properties and thermoelectric performance of $(Zn_{1-y}Mg_y)_{1-x}Al_xO$, J. Mater. Chem. 8 (1998) 409–412.

[6] M. Kazeoka, H. Hiramatsu, W.S. Seo, K. Koumoto, Improvement in thermoelectric properties of $(ZnO)_5In_2O_3$ through partial substitution of yttrium for indium, J. Mater. Res. 13 (1998) 523–526.

[7] A. Jeong, K. Suekuni, M. Ohtaki, B.K. Jang, Thermoelectric properties of In- and Ga-doped spark plasma sintered ZnO ceramics, Ceram. Int. 47 (2021) 23927–23934.

[8] P. Díaz-Chao, F. Giovannelli, O. Lebedev, D. Chateigner, L. Lutterotti, F. Delorme, E. Guilmeau, Textured Al-doped ZnO ceramics with isotropic grains, J. Eur. Ceram. Soc. 34 (2014) 4247–4256.

[9] F. Giovannelli, A.N. Ndimba, P. Díaz-Chao, M. Motelica-Heino, P.I. Raynal, C. Autret, F. Delorme, Synthesis of Al doped ZnO nanoparticles by aqueous coprecipitation, Powder Technol. 262 (2014) 203–208.

[10] S. Isobe, T. Tani, Y. Masuda, W.S. Seo, K. Koumoto, Thermoelectric performance of yttrium-substituted $(ZnO)_5In_2O_3$ improved through ceramic texturing, Jpn. J. Appl. Phys.

41 (2002) 731–732.

[11] Y. Michiue, T. Mori, A. Prytuliak, Y. Matsushita, M. Tanaka, N. Kimizuka, Electrical, optical, and thermoelectric properties of $Ga_2O_3(ZnO)_9$, RSC Adv. 1 (2011) 1788–1793.

[12] R.D. Shannon, Revised effective ionic radii and systematic studies of interatomic distances in halides and chalcogenides, Acta Crystallogr. Sect. A. 32 (1976) 751–767.

[13] A.T.T. Pham, T.A. Luu, N.K. Pham, H.K.T. Ta, T.H. Nguyen, D.V. Hoang, H.T. Lai, V.C. Tran, J.H. Park, J.K. Lee, S. Park, O. Michitaka, S.D. Park, H.Q. Nguyen, T.B. Phan, Multi-scale defects in ZnO thermoelectric ceramic materials co-doped with In and Ga, Ceram. Int. 46 (2020) 10748–10758.

[14] Z.A. Munir, U. Anselmi-Tamburini, M. Ohyanagi, The effect of electric field and pressure on the synthesis and consolidation of materials: A review of the spark plasma sintering method, J. Mater. Sci. 41 (2006) 763–777.

[15] W.T. Chiu, C.L. Chen, Y.Y. Chen, A strategy to optimize the thermoelectric performance in a spark plasma sintering process, Sci. Rep. 6 (2016) 1–9.

[16] K.W. Ho, C.C. Hang, L.S. Cao, Controllers based on gain and phase margin specifications, Automatica. 31 (1995) 497–502.

[17] L.B. McCusker, R.B. Von Dreele, D.E. Cox, D. Louër, P. Scardi, Rietveld refinement guidelines, J. Appl. Crystallogr. 32 (1999) 36–50.

[18] S.O. Yurchenko, K.A. Komarov, N.P. Kryuchkov, K.I. Zaytsev, V.V. Brazhkin, Bizarre behavior of heat capacity in crystals due to interplay between two types of anharmonicities, J. Chem. Phys. 148 (2018) 134508.

[19] A. Yoshinari, K. Ishida, K. ichiro Murai, T. Moriga, Crystal and electronic band structures of homologous compounds $Zn_kIn_2O_{k+3}$ by Rietveld analysis and first-principle calculation, Mater. Res. Bull. 44 (2009) 432–436.

[20] I. Choi, M. Kim, N. On, A. Song, K.B. Chung, H. Jeong, J Park, J. Jeong, Achieving

high mobility and excellent stability in amorphous In-Ga-Zn-Sn-O thin-film transistors, IEEE Trans Electron Devices 67 (2020) 1014–1020.

[21] F. Giovannelli, C. Chen, P. Díaz-Chao, E. Guilmeau, F. Delorme, Thermal conductivity and stability of Al-doped ZnO nanostructured ceramics, J. Eur. Ceram. Soc. 38 (2018) 5015–5020.

[22] M.W. Wu, P.H. Lai, C.H. Hong, F.C. Chou, The sintering behavior, microstructure, and electrical properties of gallium-doped zinc oxide ceramic targets, J. Eur. Ceram. Soc. 34 (2014) 3715–3722.

[23] B.A. Cook, J.L. Harringa, C.B. Vining, Electrical properties of Ga and ZnS doped ZnO prepared by mechanical alloying, J. Appl. Phys. 83 (1998) 5858–5861.

[24] J.P. Wiff, Y. Kinemuchi, K. Watari, Hall mobilities of Al- and Ga-doped ZnO polycrystals, Mater. Lett. 63 (2009) 2470–2472.

[25] X. Liang, D.R. Clarke, Relation between thermolectric properties and phase equilibria in the ZnO-In_2O_3 binary system, Acta Mater. 63 (2014) 191–201.

[26] T. Moriga, D.D. Edwards, T.O. Mason, G.B. Palmer, K.R. Poeppelmeier, J.L. Schindler, C.R. Kannewurf, I. Nakabayashi, Phase relationships and physical properties of homologous compounds in the zinc oxide-indium oxide system, J. Am. Ceram. Soc. 81 (1998) 1310–1316.

[27] S.S. Lim, J.H. Kim, B. Kwon, S. Kim, H.H. Park, K.S. Lee, J. Baik, W. Choi, D.I. Kim, D.B. Hyun, J.S. Kim, S.H. Baek, Effect of spark plasma sintering conditions on the thermoelectric properties of $(Bi_{0.25}Sb_{0.75})_2Te_3$ alloys, J. Alloys Compd. 678 (2016) 396–402.

[28] T. Moriga, K. Ishida, K. Yamamoto, A. Yoshinari, K.I. Murai, Structural analysis of homologous series of $Zn_kIn_2O_{k+3}$ (k=3, 5, 7) and Zn_kInGaO_{k+3} (k=1, 3, 5) as thermoelectric materials, Mater. Res. Innov. 13 (2009) 348–351.

[29] Y.S. Nam, J.K. Choi, J.O. Hong, Y.H. Lee, M.H. Lee, W.S. Seo, Thermoelectric properties of $Zn_kIn_2O_{3+k}$ (k = 1∼9) homologous oxides, Korean J. Mater. Res. 13 (2003) 543–549.

[30] O.K.T. Le, A.T.T. Pham, N.K. Pham, T.H.C. Pham, T.H. Nguyen, D.V. Hoang, H.K.T. Ta, D.C. Truong, H.T. Lai, T.D.T. Ung, V.C. Tran, T.B. Phan, Compensation of Zn substitution and secondary phase controls effective mass and weighted mobility in In and Ga co-doped ZnO material, J. Materiomics 7 (2021) 742–755.

[31] J. Yoon, J. Song, J. Rahman, S. Lee, W. Seo, K. Lee, S. Kim, H.S. Kim, S.I. Kim, W. Shin, High thermoelectric performance of melt-spun $Cu_xBi_{0.5}Sb_{1.5}Te_3$ by synergetic effect of carrier tuning and phonon engineering, Acta Mater. 158 (2018) 289–296.

[32] A.F. May, J.P. Fleurial, G.J. Snyder, Thermoelectric performance of lanthanum telluride produced via mechanical alloying, Phys. Rev. B. 78 (2008) 1–12.

[33] L.D. Hicks, M.S. Dresselhaus, Effect of quantum-well structures on the thermoelectric figure of merit, Phys. Rev. B. 47 (1993) 12727–12731.

[34] B.K. Jang, Y. Sakka, Thermophysical properties of porous SiC ceramics fabricated by pressureless sintering, Sci. Technol. Adv. Mater. 8 (2007) 655–659.

[35] B.K. Jang, Y. Sakka, Influence of microstructure on the thermophysical properties of sintered SiC ceramics, J. Alloys Compd. 463 (2008) 493–497.

[36] X. Zhang, L.D. Zhao, Thermoelectric materials: Energy conversion between heat and electricity, J. Mater. 1 (2015) 92–105.

[37] H.S. Kim, Z.M. Gibbs, Y. Tang, H. Wang, G.J. Snyder, Characterization of Lorenz number with Seebeck coefficient measurement, Apl. Mater. 3 (2015) 041506.

[38] K. Lee, S. Kim, Design and preparation of high-performance bulk thermoelectric materials with defect structures, J. Korean Ceram. Soc. 54 (2017) 75–85.

[39] Ü. Özgür, Y.I. Alivov, C. Liu, A. Teke, M.A. Reshchikov, S. Doğan, V. Avrutin, S.J.

Cho, H. Morkoç, A comprehensive review of ZnO materials and devices, J. Appl. Phys. 98 (2005) 041301.

[40] N.H.T. Nguyen, T.H. Nguyen, Y.R. Liu, M. Aminzare, A.T.T. Pham, S. Cho, D.P. Wong, K.H. Chen, T. Seetawan, N.K. Pham, H.K.T. Ta, V.C. Tran, T.B. Phan, Thermoelectric properties of indium and gallium dually doped ZnO thin films, ACS Appl. Mater. Interfaces 8 (2016) 33916–33923.

[41] A. Jeong, K. Suekuni, M. Ohtaki, B.K. Jang, Thermoelectric properties of In- and Ga-doped spark plasma sintered ZnO ceramics, Ceram. Int. 47 (2021) 23927–23934.

Chapter 4. Characterization of ZnO Thermoelectric Ceramics and Their Microstructures Consolidated by Two-Step Spark Plasma Sintering

4.1. Introduction

Energy-harvesting materials and methodologies have been required to enable smart systems in our society to meet the increasing energy demands [1]. One of the eco-friendly and straightforward approach is the conversion of waste heat or environmental heat into electrical energy. The conversion efficiency [2] of thermoelectric (TE) materials is determined by the dimensionless figure of merit (ZT) given by the following equation:

$$ZT = \frac{S^2\sigma}{\kappa} \qquad (1)$$

where S, σ, κ, and T represent the Seebeck coefficient, the electrical conductivity, the thermal conductivity, and the absolute temperature, respectively [3].

ZnO TE material shows high electrical performance [4] with a power factor of ~0.4 mW K^{-2} m^{-1} at 1000°C, making it competitive with conventional TE materials. Also, ZnO ceramics exhibit the main limitation with the high κ value of ~5 W K^{-1} m^{-1} at 1000°C. There are several strategies to reduce the thermal conductivity, such as enhancing phonon scattering [5–8] by reducing the crystal grain size or consolidating nanostructure ceramics from nano powders [9,10].

In recent years, spark plasma sintering (SPS) has proven capable of consolidating bulk ceramic bodies with fine-grained microstructures showing superior properties in a wide range of materials. The differences between conventional sintering (CS) such as hot pressing [11] or

hot isotactic pressing [12] and two-step sintering (TS) [13–15] are as follows: In the case of CS, where a given powder is sintered at a certain single temperature, the densification is faster for smaller particles, leading to nonuniform grain size distributions with some very large grains and residual porosity. In the case of TS, on the other hand, pore channels become smoother during the first heating step at a higher temperature with a shorter duration, and the inhomogeneous densification is reduced, delaying pore-channel pinch-off until a later sintering stage [13]. The advantages of employing SPS for the consolidation of bulk TE oxides are that it can retain finer grains, achieve higher relative densities, minimize the loss of oxygen, and suppress grain-growth [16]. It is therefore imperative to develop a more advanced SPS technique that promotes only densification, without grain-growth, during sintering.

The TS method was introduced in the 1990s by Chu *et al*. [17] Chen and Wang developed a new TS technique as a promising approach to obtain fully dense nanograin ceramics [18]. The technique consists of (A) heating to a temperature (T_1) for the first-step of sintering, (B) achieving a critical density of > 75% theoretical density (TD) [18] to render pores unstable, and (C) lowering the temperature to T_2 for the second-step of sintering, during which only densification proceeds, without grain-growth. However, the combination of TS and SPS processes (TS-SPS) on ZnO-based TE oxides has not been studied yet.

In this work, the effects of the TS-SPS process under different heating conditions are addressed with focuses on the sample density, grain size, and TE performance of the non-doped ZnO ceramics as a preliminary research of TS-SPS.

4.2. Experimental Procedures

ZnO powder (99.99%, Sigma-Aldrich, USA) was used as purchased for the starting material. The ZnO powder was pulverized with a planetary ball mill (Pulverisette 6, Fritsch GmbH, Germany) at 300 rpm for 1.5 h. The powder was then molded into a pellet by applying a uniaxial pressure of 100 MPa. The samples were calcined at 1100°C for 24 h in air with heating and cooling rates of 100°C/h. After the first calcination, the pellets were thoroughly ground and then pressed at 100 MPa into pellets again. The second calcination was carried out under the same conditions as the first calcination, and the calcined pellets were reground.

The calcined powder was loaded into a graphite die with an inner diameter of 10 mm for SPS on a PLASMAN CSP-I-03121 (S. S. Alloy, Japan). The SPS chamber was evacuated at ≤ 25 Pa. The temperature for first-step sintering (T_1) was set at 1100 or 1150°C to be higher than the temperature for second-step sintering at 1050°C (T_2). A temperature higher than 1100°C was selected for T_1 based on the previous study [19]. For first-step sintering, the samples were heated to 1100 or 1150°C under a uniaxial pressure of 50 MPa at a high heating rate of 100°C/min with a holding time of 15 or 5 min, respectively. For second-step sintering, the holding time was varied: 30, 60, and 120 min at 1050°C. Subsequently, the pressure was released to prevent crack formation, and the furnace was cooled to 100°C at a cooling rate of 20°C/min. The height of the samples obtained after sintering was approximately 7 mm. The conditions of OS/TS-SPS processes are summarized in Table 6. The samples are named [one-step/two-step]-T_1-[duration of T_2 (1050°C)]. Schematic drawings of the temperature profiles of the OS/TS-SPS processes are shown in Fig. 36.

X-ray diffraction (XRD) measurement was carried out on a Rigaku MiniFlex 600 diffractometer operated with Cu Kα radiation at 40 kV and 15 mA. The scanning was performed over a range of 2θ = 20–80° with a scanning step of 0.01°. The Rietveld analysis [20] using PDXL 2 software was carried out to refine the crystal structures. For observation of

the sample microstructure, cross-sectional surfaces of the samples were polished with diamond abrasive pads with incremental grit sizes of up to #2000, then lapped with diamond suspensions with particle sizes of 3 and 0.5 μm. The electron backscatter diffraction (EBSD) measurement to analyze the grain size of the samples was carried out on a JSM-IT700HR (JEOL, Japan) field-emission scanning electron microscope equipped with an EBSD detector (C-Nano, Oxford Instruments, UK). ImageJ software was used to obtain the average grain sizes and their standard deviations for the microstructure of the samples [21].

The electrical conductivity σ and the Seebeck coefficient S were simultaneously measured in air using a four-probe DC method and a temperature-differential method, respectively, on a RZ2001i (Ozawa Science, Japan). The reproducibility of the σ and S measurements was confirmed by well-overlapped results for heating and cooling paths in the range of 27–800°C. The thermal diffusivity α and the specific heat C_p at 27–800°C were measured simultaneously on a LFA-502 (Kyoto Electronics, Japan) using a laser-flash method under vacuum. The absolute values of C_p were obtained through a comparative method using a molybdenum standard sample as a reference. The total thermal conductivity was calculated using the relation $\kappa = \alpha\, C_p\, d_s$, where d_s is the sample density.

Table 6. Conditions of the OS/TS-SPS processes for ZnO ceramic samples.

The sample names denote [one-step/two-step]-T_1-[duration of second-step sintering at 1050°C]. Note that, in first-step sintering, XX-1100 samples were kept at T_1 for 15 min, while XX-1150 samples were kept for 5 min. The second-step sintering was at 1050°C for all the samples.

	Heating conditions			
	First-step sintering		Second-step sintering	
Sample	T_1 (°C)	Holding time (min)	T_2 (°C)	Holding time (min)
OS-1100	1100	15	–	–
TS-1100-30	1100	15	1050	30
TS-1100-60	1100	15	1050	60
TS-1100-120	1100	15	1050	120
OS-1150	1150	5	–	–
TS-1150-30	1150	5	1050	30
TS-1150-60	1150	5	1050	60
TS-1150-120	1150	5	1050	120

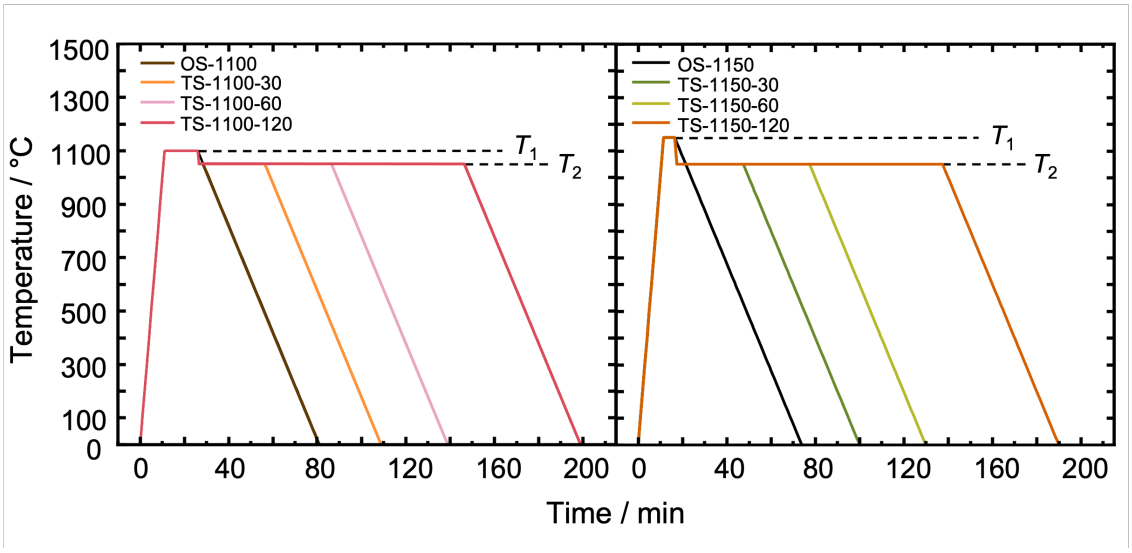

Fig. 36. Temperature profiles of OS/TS-SPS processes for ZnO ceramic samples.

4.3. Results and Discussion

4.3.1. Microstructural Analysis of ZnO

Figure 37 shows the XRD patterns of the ZnO ceramics formed by OS/TS-SPS. Regardless of the temperature and holding time of OS/TS-SPS, all the XRD patterns were assigned to the wurtzite structure of ZnO with the $P6_3mc$ (186) space group. The sharp and narrow XRD peaks indicate that the samples have good crystallinity and fairly large crystallite sizes. The lattice constants of all the samples were determined by the Rietveld refinement as a = 3.252 Å and c = 5.210 Å, which are in good agreement with the literature values [22].

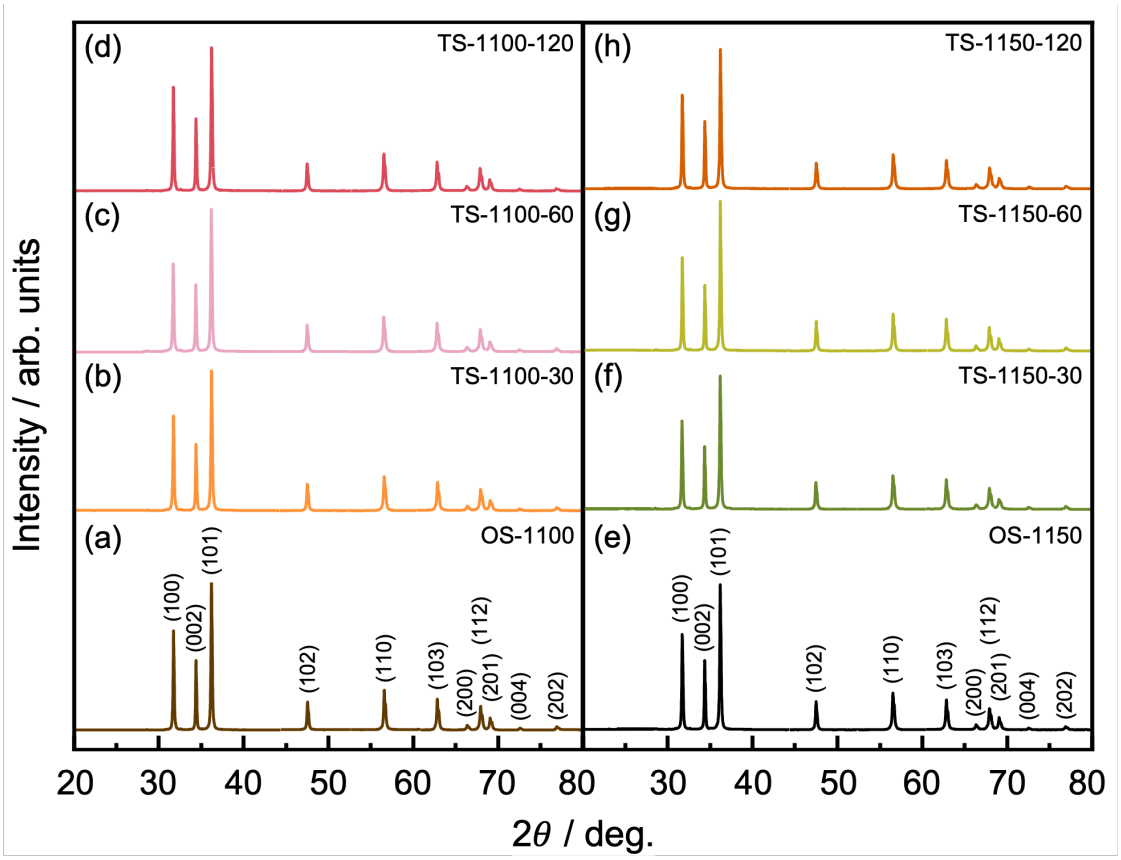

Fig. 37. X-ray diffraction patterns of the OS/TS-SPS ZnO samples in Table 6. The first-step sintering of (a)–(d) was at 1100°C for 15 min, while that of (e)–(h) was at 1150°C for 5 min. The second-step was maintained at 1050°C for 30, 60, and 120 min for (b) and (f), (c) and (g), and (d) and (h), respectively.

The relative densities of the OS/TS-SPS ZnO samples are summarized in Table 7. High relative densities of 91.4–94.9% were achieved except with OS-1150 (85.6%), and it seems that the duration at T_1 = 1150°C was insufficient for OS. The TS-SPS process thus proved a significant advantage for increasing the relative density in comparison with our previous study (91.3%) [19].

Table 7. Relative densities of the OS/TS-SPS ZnO under various conditions.

Sample	Relative density (%)
OS-1100	91.4
TS-1100-30	91.5
TS-1100-60	93.6
TS-1100-120	94.0
OS-1150	85.6
TS-1150-30	91.4
TS-1150-60	93.9
TS-1150-120	94.9

The EBSD measurement was carried out with a step size of 0.05 μm to analyze the microstructure of the samples. The normal-direction inverse pole figure (IPF) maps are expected to reveal the morphology, size, and orientation of the grains. Figure 38 shows the IPF maps of (a) OS-1100, (b) TS-1100-30, and (c) TS-1100-120. The black areas in the IPF maps correspond to the regions where EBSD failed to index the crystallographic orientation due to the holes (voids) or highly defective crystallinity of the grains. In agreement with the XRD data in Fig. 37, the IPF maps show no signs of preferred orientation. The OS-1100 sample consists of coarse grains with an average diameter of 8.1 μm, while the TS-1100-30 and TS-1100-120 samples have smaller and uniform grain sizes of 3.5 μm and 3.6 μm on average, respectively.

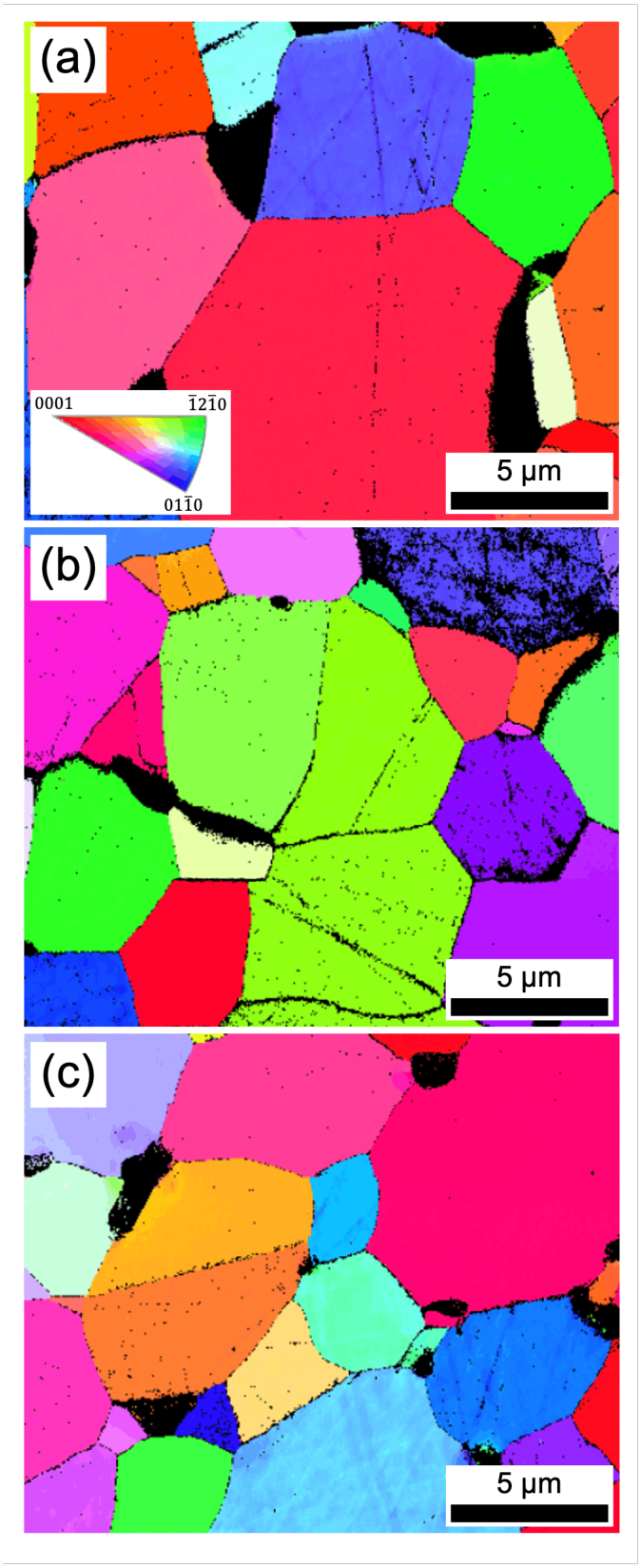

Fig. 38. IPF maps of the OS/TS-SPS ZnO. The samples are (a) OS-1100, (b) TS-1100-30, and (c) TS-1100-120. The map colors are assigned using the IPF color scale shown in (a).

The difference in grain size between the OS-SPS and TS-SPS samples clearly shows the suppression of grain-growth by 56% for the TS-SPS sample in comparison with its OS-SPS counterpart. There are two possible reasons for this grain-growth suppression by prolonged sintering at lower temperature at the second-step. The first reason might be a reported fact of the sintering behavior of ZnO: in a certain temperature range around 700°C, the grain-growth preferably proceeds, but the densification does not [23]. Since the first-step temperature (T_1 = 1100°C) is high enough but the duration is very short (15 min = 0.9 ks) in the present study, the OS samples had low relative densities, as shown in Table 7. This means that the OS samples have more room for grain-growth during cooling. On the other hand, the TS samples underwent prolonged sintering during the second-step at 1050°C, where they could be sufficiently densified, and thus the grains in the TS samples no longer had enough room to grow during subsequent cooling. The second reason was reported that the grain-growth was suppressed in alumina by a comparison of grain size in OS and TS sintering [24]. In the case of the OS sintering, the final grain size of the nearly fully dense alumina sample was higher than an average diameter of 1.2 μm (~ 98% TD) at 1300°C, whereas the TS sintering sample obtained the grain size of 0.85 μm on average (97.8% TD) at T_1 and T_2 = 1300, 1150°C, respectively [24]. These results clearly elucidated the mechanism of TS sintering, suppressing the grain-growth with a high relative density by triple junctions as well as pore junctions. Initially, a critical density should be achieved with sufficient triple junctions in the sample so that the triple junctions impede grain-boundary migration. Subsequently, when the sintering temperature reaches at T_2, densification is increased while preventing grain-growth. This TS-SPS strategy is expected to provide an opportunity to densify ZnO-based TE materials while retaining fine grains for the reduction of thermal conductivity.

4.3.2. Thermoelectric Properties

Figure 39 shows the temperature dependence of the electrical conductivity (σ), Seebeck coefficient (S), and power factor (PF, $S^2\sigma$). The trade-off between σ and $|S|$ against the carrier concentration n can be given according to the Boltzmann transport theory as follows [25]:

$$\sigma = ne\mu \qquad (2)$$

$$|S| = \frac{8\pi^2 k_B^2}{3eh^2} m^* T \left(\frac{\pi}{3n}\right)^{2/3}, \qquad (3)$$

where e is the electron charge, μ is the carrier mobility, k_B is the Boltzmann constant, m^* is the effective mass of electrons, h is the Planck constant, and T is the absolute temperature. The electrical conductivity of all samples gradually decreased with the temperature increase from 70 to 775°C, indicating a metallic behavior [26]. Figure 39(a) shows that OS-1100 has the lowest σ, from 8.2 to 1.6 S cm^{-1} over a temperature range of 70 to 775°C, respectively.

In contrast, the TS-SPS ZnO samples with second-step sintering at 1050°C for 30, 60, and 120 min have higher electrical conductivities, from 10–12 to 1.8–2.0 S cm^{-1} for temperatures from 70 to 775°C, respectively. The TS-SPS ZnO samples showed a higher σ than that of OS-SPS ZnO at 70°C and at 775°C (1.6 S cm^{-1}). Figures 39(a, c) and (b, d) shows the inverse relationship between σ and $|S|$, where $|S|$ increased with increasing temperature. It is noticeable that the OS-1150 sample with the lowest relative density (85.6%) shows the largest $|S|$, as seen in Fig. 39(d). This tendency of $|S|$ against the relative density was reported by Ohtaki *et al*. [27], where Al-doped nanovoid ZnO showed a larger $|S|$ than the samples without nanovoids. The S value of the TS-1100-120 sample was –632 μV K^{-1} at 775°C, while that of the TS-1150-120 sample was –605 μV K^{-1}. The PF values of the OS/TS-SPS ZnO samples were within a range of 6.3 × 10^{-5} to 6.8 × 10^{-5}–7.8 × 10^{-5} W K^{-2} m^{-1}, as shown in Fig. 39(e) and 39(f). Although the highest PF value in the present study was 7.8 × 10^{-5} W K^{-2} m^{-1} for the TS-1100-120 sample,

the highest *PF* value attained in our previous study was 6.4×10^{-5} W K^{-2} m^{-1} for the OS-1150 sample (non-doped ZnO) [28]. These findings imply that the TS-SPS process is effective to improve *PF*, and they strongly suggest that the carrier doping to TS-SPS ZnO will achieve much higher *PF* and, hence, *ZT* values.

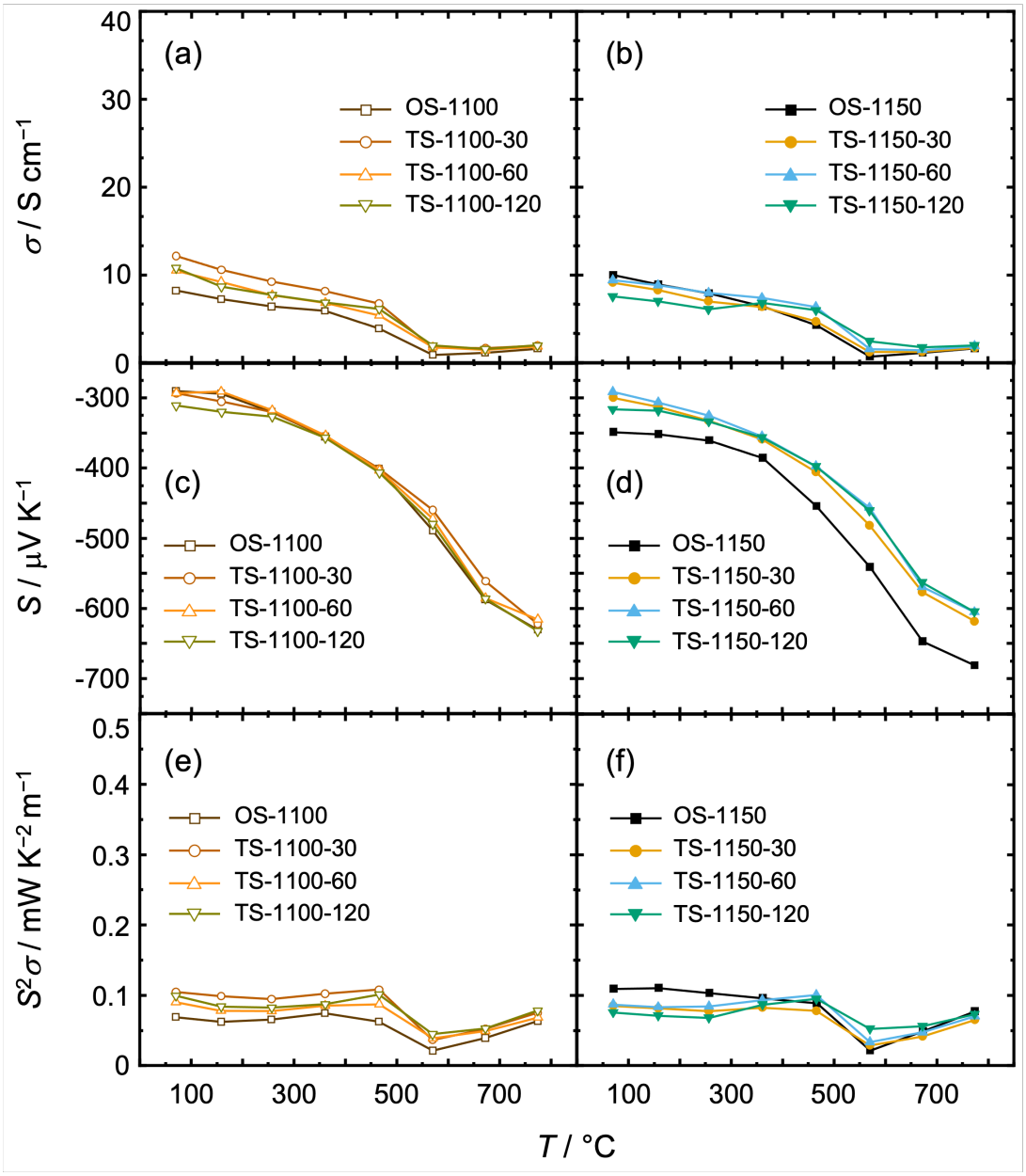

Fig. 39. Temperature dependence of (a, b) the electrical conductivity σ, (c, d) the Seebeck coefficient S, and (e, f) the power factor $S^2\sigma$. The first-step sintering conditions of (a), (c), and (e) were 1100°C for 15 min, and those for (b), (d), and (f) were 1150°C for 5 min.

Figure 40 shows the temperature dependence of the thermal conductivity of the OS/TS-SPS samples. The thermal conductivity decreased substantially with increasing temperature due to increasing phonon–phonon scattering [29–33].

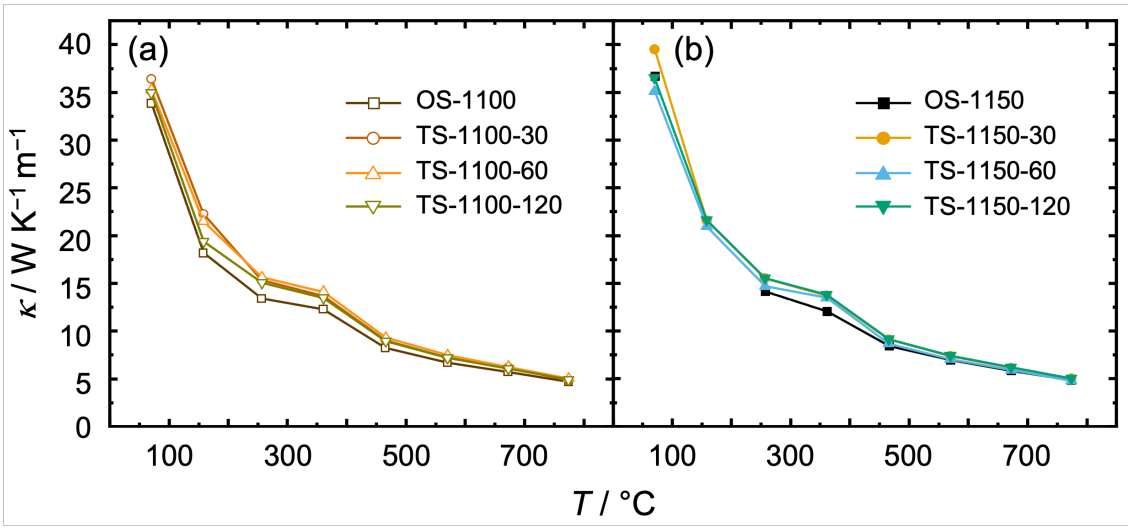

Fig. 40. Temperature dependence of the thermal conductivity κ of the OS/TS-SPS ZnO ceramic samples. The first-step sintering condition of (a) was 1100°C for 15 min, while that of (b) was 1150°C for 5 min.

The OS-1100 sample with an average grain size of 8.1 μm showed a slightly lower thermal conductivity of 4.7 W K^{-1} m^{-1} at 775°C compared with a higher value of 4.9 W K^{-1} m^{-1} for TS-1100-30 (grain size 3.5 μm) and TS-1100-120 (grain size 3.6 μm) samples, as seen in Fig. 40(a). These thermal conductivities are about 2 times lower than compared with the previously reported value of approximately 8 W K^{-1} m^{-1} for pure ZnO (grain size ~2.5 μm) at 827°C, showing the contribution of OS/TS-SPS processes [11,34]. Although it is known that small grains would shorten the mean free path of phonons and lower thermal conductivity [35], the order of the thermal conductivity in this study disagreed with the order of the grain size, probably due to the influence of the lower relative density of the OS-1100 sample. Figure 40 (b) shows the thermal conductivity of the OS/TS-SPS samples with T_1 = 1150°C for 5 min.

The TS-1150-60 sample showed the lowest thermal conductivity, 4.8 W K^{-1} m^{-1} at 775°C, among the TS-SPS samples, whereas the lowest thermal conductivity for non-doped ZnO formed by OS-SPS at 1150°C in our previous study was 5.2 W K^{-1} m^{-1} at 773°C [28]. It is thus implied that the decrease in sintering temperature in the TS-SPS process might reduce thermal conductivity while retaining a high relative density.

The dimensionless figure of merit of the OS/TS-SPS samples is shown in Fig. 41. All the OS/TS-SPS samples have rather similar *ZT* values of 0.014–0.017. It should be noted that the ZnO samples in this work are all non-doped ones. However, a comparison of OS-1100 and TS-1100-120 suggests that the smaller grains would be further beneficial for *ZT*, as supported by the EBSD results presented in Fig. 38. In other words, the TS-SPS process denotes that the *ZT* value of the present ZnO sample can be improved by optimizing its microstructures.

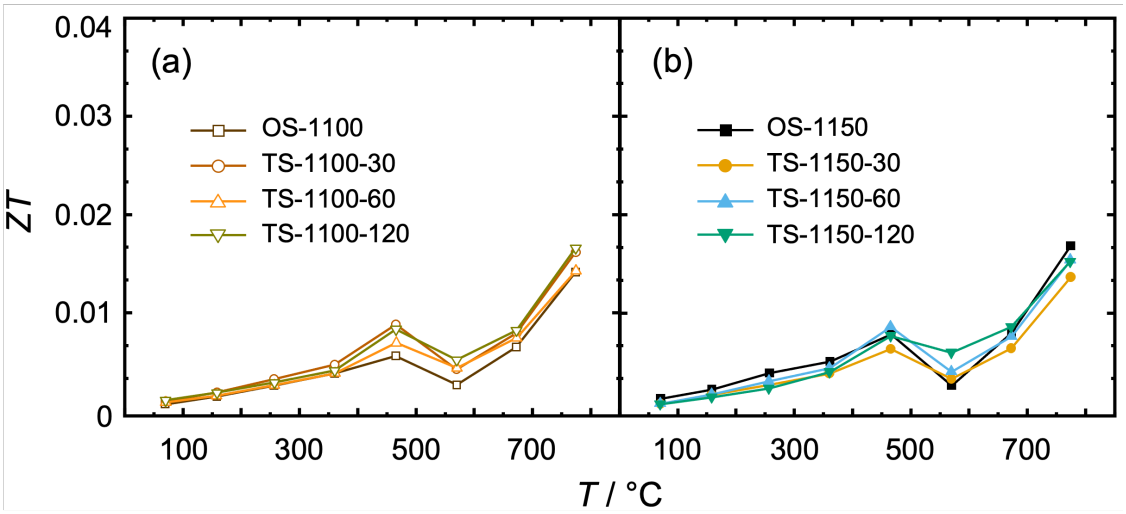

Fig. 41. Dimensionless figure of merit *ZT* of the OS/TS-SPS ZnO. The first-step sintering condition of (a) was 1100°C for 15 min, while that of (b) was 1150°C for 5 min.

4.4. Conclusions

ZnO TE ceramics were consolidated by OS/TS-SPS processes, and the effect of the TS-SPS process on the density, grain size, and TE performance of ZnO ceramics was investigated. All the XRD patterns were assigned to the wurtzite structure of ZnO. High relative densities of 91.4–94.9% were achieved except for OS-1150 (85.6%). The TS-SPS process thus proved a significant advantage for increasing the relative density. The EBSD results revealed a noticeable suppression of grain-growth (56%, reduced from 8.1 to 3.6 μm) for the TS-SPS sample with T_1 = 1100°C.

The highest *PF*, 7.8×10^{-5} W K^{-2} m^{-1}, was achieved for the TS-1100-120 sample, attaining a *ZT* of 0.017 at 775°C. The *PF* value was higher than that of the In and Ga dual-doped ZnO sample in our previous study, implying that the TS-SPS process is effective to improve *PF* and strongly suggesting that the carrier doping to TS-SPS ZnO can be expected to achieve much higher *PF* and hence *ZT* values. The TS-SPS strategy can provide a new opportunity for significant progress in ZnO-based TE materials.

References

[1] T. Mori, S. Priya, Materials for energy harvesting: At the forefront of a new wave, MRS Bull. 43 (2018) 176–180.

[2] I. Terasaki, R. Okazaki, H. Ohta, Search for non-equilibrium thermoelectrics, Scr. Mater. 111 (2016) 23–28.

[3] M. Ohtaki, Recent aspects of oxide thermoelectric materials for power generation from mid-to-high temperature heat source, J. Ceram. Soc. Jpn. 119 (2011) 770–775.

[4] M. Ohtaki, T. Tsubota, K. Eguchi, H. Arai, High-temperature thermoelectric properties of $(Zn_{1-x}Al_x)O$, J. Appl. Phys. 79 (1996) 1816–1818.

[5] E. Guilmeau, P. Díaz-Chao, O.I. Lebedev, A. Rečnik, M.C. Schäfer, F. Delorme, F. Giovannelli, M. Košir, S. Bernik, Inversion boundaries and phonon scattering in Ga:ZnO thermoelectric compounds, Inorg. Chem. 56 (2017) 480–487.

[6] S. Saini, P. Mele, T. Oyake, J. Shiomi, J.P. Niemelä, M. Karppinen, K. Miyazaki, C. Li, T. Kawaharamura, A. Ichinose, L. Molina-Luna, Porosity-tuned thermal conductivity in thermoelectric Al-doped ZnO thin films grown by mist-chemical vapor deposition, Thin Solid Films. 685 (2019) 180–185.

[7] R.V.R. Virtudazo, B. Srinivasan, Q. Guo, R. Wu, T. Takei, Y. Shimasaki, H. Wada, K. Kuroda, S. Bernik, T. Mori, Improvement in the thermoelectric properties of porous networked Al-doped ZnO nanostructured materials synthesized via an alternative interfacial reaction and low-pressure SPS processing, Inorg. Chem. Front. 7 (2020) 4118–4132.

[8] A.T.T. Pham, T.A. Luu, N.K. Pham, H.K.T. Ta, T.H. Nguyen, D.V. Hoang, H.T. Lai, V.C. Tran, J.H. Park, J.K. Lee, S. Park, O. Michitaka, S.D. Park, H.Q. Nguyen, T.B. Phan, Multi-scale defects in ZnO thermoelectric ceramic materials co-doped with In and Ga, Ceram. Int. 46 (2020) 10748–10758.

[9] H.S. Kim, S.I. Kim, K.H. Lee, S.W. Kim, G. J. Snyder, Phonon scattering by dislocations at grain boundaries in polycrystalline $Bi_{0.5}Sb_{1.5}Te_3$, Phys. Status Solidi B. 254 (2017) 1600103.

[10] F. Giovannelli, C. Chen, P. Díaz-Chao, E. Guilmeau, F. Delorme, Thermal conductivity and stability of Al-doped ZnO nanostructured ceramics, J. Eur. Ceram. Soc. 38 (2018) 5015–5020.

[11] H. Cheng, X.J. Xu, H.H. Hng, J. Ma, Characterization of Al-doped ZnO thermoelectric materials prepared by RF plasma powder processing and hot press sintering, Ceram. Int. 35 (2009) 3067–3072.

[12] S. Hirano, S. Isobe, T. Tani, N. Kitamura, I. Matsubara, K. Koumoto, Electrical and thermal transport properties in layer-structured $(ZnO)_mIn_2O_3$ (m = 5 and 9) ceramics, Jpn. J. Appl. Phys. 41 (2002) 6430–6435.

[13] N.J. Lóh, L. Simão, C.A. Faller, A. De Noni, O.R.K. Montedo, A review of two-step sintering for ceramics, Ceram. Int. 42 (2016) 12556–12572.

[14] L. An, A. Ito, T. Goto, Two-step pressure sintering of transparent lutetium oxide by spark plasma sintering, J. Eur. Ceram. Soc. 31 (2011) 1597–1602.

[15] Y. Pan, Y. Qiu, I. Witting, L. Zhang, C. Fu, J.W. Li, Y. Huang, F.H. Sun, J. He, G.J. Snyder, C. Felser, J.F. Li, Synergistic modulation of mobility and thermal conductivity in $(Bi,Sb)_2Te_3$ towards high thermoelectric performance, Energy Environ. Sci. 12 (2019) 624–630.

[16] Z.A. Munir, U. Anselmi-Tamburini, M. Ohyanagi, The effect of electric field and pressure on the synthesis and consolidation of materials: A review of the spark plasma sintering method, J. Mater. Sci. 41 (2006) 763–777.

[17] M.Y. Chu, L.C. De Jonghe, M.K.F. Lin, F.J.T. Lin, Precoarsening to improve microstructure and sintering of powder compacts, J. Am. Ceram. Soc. 74 (1991) 2902–

2911.

[18] I. W. Chen, X. H. Wang, Sintering dense nanocrystalline ceramics without final-stage grain growth, Nature 404 (2000) 168–171.

[19] A. Jeong, K. Suekuni, M. Ohtaki, B.K. Jang, Thermoelectric properties of In- and Ga-doped spark plasma sintered ZnO ceramics, Ceram. Int. 47 (2021) 23927–23934.

[20] L.B. McCusker, R.B. Von Dreele, D.E. Cox, D. Louër, P. Scardi, Rietveld refinement guidelines, J. Appl. Crystallogr. 32 (1999) 36–50.

[21] M. Doube, M.M. Klosowski, I. Arganda-Carreras, F.P. Cordelières, R.P. Dougherty, J.S. Jackson, B. Schmid, J.R. Hutchinson, S.J. Shefelbine, BoneJ: Free and extensible bone image analysis in ImageJ, Bone. 47 (2010) 1076–1079.

[22] Ü. Özgür, Y.I. Alivov, C. Liu, A. Teke, M.A. Reshchikov, S. Doğan, V. Avrutin, S.J. Cho, H. Morkoç, A comprehensive review of ZnO materials and devices, J. Appl. Phys. 98 (2005) 041301.

[23] M. Mazaheri, A.M. Zahedi, S.K. Sadrnezhaad, Two-step sintering of nanocrystalline ZnO compacts: Effect of temperature on densification and grain growth, J. Am. Ceram. Soc. 91 (2008) 56–63.

[24] Z.R. Hesabi, M. Haghighatzadeh, M. Mazaheri, D. Galusek, S.K. Sadrnezhaad, Suppression of grain growth in sub-micrometer alumina via two-step sintering method, J. Eur. Ceram. Soc. 29 (2009) 1371–1377.

[25] K.P. Ong, D.J. Singh, P. Wu, Analysis of the thermoelectric properties of n-type ZnO, Phys. Rev. B 83 (2011) 115110.

[26] B. Zhou, L. Chen, C. Li, N. Qi, Z. Chen, X. Su, X. Tang, Significant enhancement in the thermoelectric performance of aluminum-doped ZnO tuned by pore structure, ACS Appl. Mater. Inter. 12 (2020) 51669–51678.

[27] M. Ohtaki, K. Araki, Thermoelectric properties and thermopower enhancement of Al-

doped ZnO with nanosized pore structure, J. Ceram. Soc. Jpn. 119 (2011) 813–816.

[28] A. Jeong, M. Ohtaki, B.K. Jang, Thermoelectric performance of In and Ga single/dual-doped ZnO ceramics fabricated by spark plasma sintering, Ceram. Int. 48 (2022) 14414–14423.

[29] R.V.R. Virtudazo, Q. Guo, R. Wu, T. Takei, T. Mori, An alternative, faster and simpler method for the formation of hierarchically porous ZnO particles and their thermoelectric performance, RSC Adv. 7 (2017) 31960–31968.

[30] A.F. May, J.P. Fleurial, G.J. Snyder, Thermoelectric performance of lanthanum telluride produced via mechanical alloying, Phys. Rev. B. 78 (2008) 1–12.

[31] L.D. Hicks, M.S. Dresselhaus, Effect of quantum-well structures on the thermoelectric figure of merit, Phys. Rev. B. 47 (1993) 12727–12731.

[32] B.K. Jang, Y. Sakka, Thermophysical properties of porous SiC ceramics fabricated by pressureless sintering, Sci. Technol. Adv. Mater. 8 (2007) 655–659.

[33] C. Bourgès, Y. Bouyrie, A.R. Supka, R. Al Rahal Al Orabi, P. Lemoine, O.I. Lebedev, M. Ohta, K. Suekuni, V. Nassif, V. Hardy, R. Daou, Y. Miyazaki, M. Fornari, E. Guilmeau, High-performance thermoelectric bulk colusite by process controlled structural disordering, J. Am. Chem. Soc. 140 (2018) 2186–2195.

[34] S. Sulaiman, S. Izman, M.B. Uday, M.F. Omar, Review on grain size effects on thermal conductivity in ZnO thermoelectric materials, RSC Adv. 12 (2022) 5428–5438.

[35] K. Koumoto, Y. Wang, R. Zhang, A. Kosuga, R. Funahashi, Oxide thermoelectric materials: a nanostructuring approach, Annu. Rev. Mater. Res. 40 (2010) 363–394.

Chapter 5. Effects of Two-Step Spark Plasma Sintering on the Microstructures and Thermoelectric Properties of Pure/In-doped ZnO

5.1. Introduction

With increasing global concern for energy and environmental problems, thermoelectric (TE) technology has attracted attention because it can convert waste heat into electrical power [1]. Intermetallic compounds such as Bi_2Te_3 and PbTe can give the best performance as TE materials [2–4]. However, their operating temperatures (27–227°C and below 627°C, respectively) are inherently limited by their melting points, which are 580°C and 924°C, respectively. Even below the melting points, these materials are not attractive because surface oxidation and vaporization can easily occur at such high temperatures. Furthermore, their constituting heavy metal elements are mostly toxic, scarce, and expensive. The efficiency [5] of a TE material is defined by a dimensionless figure of merit, $ZT = S^2\sigma T / \kappa$, where S, σ, T, and κ are the Seebeck coefficient, electrical conductivity, absolute temperature, and thermal conductivity, respectively. The ZT values can be enhanced by maximizing the power factor ($S^2\sigma$, PF) and reducing the thermal conductivity.

One obstacle to increasing σ of ZnO is the limited solubility of donor dopants such as Al, In, and Ga, which is too low to achieve a sufficient carrier concentration for maximizing the PF of ZnO-based TE materials [6–8]. Therefore, increasing the solubility of donor dopants is needed to optimize the PF. However, the enhancement of the carrier concentration should be carefully designed because there is a trade-off between S and σ. A higher carrier concentration leads to a higher σ but a lower S. Therefore, a moderate carrier concentration is required to maximize the PF.

The spark plasma sintering (SPS) technique, which combines a pulsed large electric current and uniaxial pressure, was developed as an efficient method of sintering a powder at low temperatures in a short time. During SPS, the electric current is known to enhance densification by improving diffusion while suppressing grain-growth, preserving the fine-grained microstructures. In the case of conventional sintering (CS), such as hot pressing and one-step (OS) sintering [9], where a given powder is sintered at a certain single temperature, the densification is faster for smaller particles, leading to nonuniform distributions of grain sizes. In the case of two-step (TS) sintering [10,11], on the other hand, pore channels become smoother during the first heating step at a higher temperature with a shorter duration, and the inhomogeneous densification is reduced, delaying pore-channel pinch-off until a later sintering stage [10]. Some advantages of employing SPS for the consolidation of bulk thermoelectric oxides are that it can retain finer grains and achieve higher relative densities. Therefore, it is crucial to develop a SPS technique that promotes densification only without grain-growth.

The TS method was introduced by Chu *et al.* in the 1990s [12]. Wang and Chen proposed a new TS technique as a promising approach for obtaining high-density nanograin materials. The sequence of this technique is (i) heating to a temperature (T_1) for the first step of sintering, (ii) achieving a critical density above 75% theoretical density (TD) or more to destabilize the pores, and (iii) lowering the temperature to T_2 for the second step of sintering; only densification proceeds without grain-growth. Furthermore, a smaller grain size by suppressed grain-growth can shorten the phonon mean free path or enhance phonon scattering so that it can reduce the thermal conductivity. The thermal conductivity can be calculated as shown in Eq. (1) [13]

$$\kappa = \frac{1}{3}\int C\rho v l \qquad (1)$$

where C is the specific heat, ρ is the density, v is the speed of sound, and l is the phonon mean free path.

Nevertheless, a new combination of TS and SPS processes (TS-SPS) on ZnO-based thermoelectric oxides has not been studied so far. In our previous work, the characterization of pure ZnO ceramics on their microstructures and TE properties has been carried out [14] so that an advanced TE property of In-doped ZnO must be studied to figure out an improvement of doping in the ZnO matrix. The purpose of the present study is to investigate the effects of the TS-SPS process under different heating conditions on the relative density, grain size, and TE performance of the pure/In-doped ZnO ceramics.

5.2. Experimental Procedures

ZnO and In_2O_3 commercial powders (99.99%, Sigma-Aldrich, USA) were used as starting materials. Pure ZnO (non-doped ZnO) and In_2O_3 powders were mixed at appropriate ratios to prepare samples of $[Zn_{(1-x)}In_x]O$ (x = 0, 0.005) and pulverized using a planetary ball mill (Pulverisette 6, Fritsch GmbH, Germany) at a rotation speed of 100 rpm for 1.5 h.

The powders were then molded into pellets and uniaxially pressed at 100 MPa. To improve the homogeneity of the samples, the pellets were calcined at 1100°C for 24 h in air with heating and cooling rates of 100°C/h. After the first calcination, pellets were thoroughly ground in an agate mortar for 20 min and then pressed at 100 MPa again into pellets with a diameter of 20 mm. The second calcination was carried out under the same conditions as the first calcination, and the calcined pellets with a diameter of 20 mm were reground.

The calcined powder was loaded into a graphite die with an inner diameter of 10 mm, which was placed in SPS (PLASMAN CSP-I-03121, S. S. Alloy, Japan). For the SPS treatment, the SPS chamber was evacuated at ≤ 15 Pa. The temperature for the first-step sintering (T_1) was set at 1150°C so as to be higher than the temperature for the second-step sintering (T_2) at 900–1100°C [6] in a vacuum. For the first-step sintering, samples were heated at 1150°C under a uniaxial pressure of 50 MPa and the current of 17–253 A at a high heating rate of 100°C/min with a holding time of 15 min. For the second-step sintering, the temperature varied—900, 950, 1000, 1050, and 1100°C —for a duration of 30 min. Then the furnace was cooled to 100°C at a cooling rate of 20°C/min by releasing the pressure to avoid the formation of cracks. The sintering conditions of the OS/TS-SPS processes for pure and In-doped ZnO are summarized in Table 8. The samples are called [Pure/In-doped)]-OS(one-step)-T_1 and [Pure/In-doped)]-TS(two-step)-T_2. Schematic illustrations of the temperature profiles of the OS/TS-SPS processes for pure and In-doped ZnO are shown in Fig. 42.

Table 8. Sintering conditions of the OS/TS-SPS processes for pure and In-doped ZnO ceramic samples.

		Heating conditions			
		First-step sintering		Second-step sintering	
	Sample	T_1 / °C	Holding time /min	T_2 / °C	Holding time /min
Pure ZnO	P-OS-1150	1150	15	–	–
	P-TS-900	1150	15	900	30
	P-TS-950	1150	15	950	30
	P-TS-1000	1150	15	1000	30
	P-TS-1050	1150	15	1050	30
	P-TS-1100	1150	15	1100	30
In-doped ZnO	I-OS-1150	1150	15	–	–
	I-TS-950	1150	15	950	30
	I-TS-1000	1150	15	1000	30
	I-TS-1050	1150	15	1050	30

For the X-ray diffraction (XRD) measurements, sintered samples were analyzed with a Rigaku MiniFlex 600 diffractometer operated with Cu Kα radiation at 40 kV and 15 mA. The measurement angle (2θ) was over a range of 20–80° with a scanning step of 0.01°. The crystal structures of the pure/In-doped ZnO sintered samples were refined via the Rietveld refinement [15]. For observing the sample microstructure, cross-sectional surfaces of the samples were polished with diamond abrasive pads up to #2000 and then lapped with diamond suspensions with particle sizes of 3 and 0.5 μm. To analyze the microstructure so as to estimate the grain size of the samples, the electron backscatter diffraction (EBSD) was measured using a JSM-IT700HR (JEOL, Japan) field-emission scanning electron microscope (FE-SEM) equipped with an EBSD detector (C-Nano, Oxford Instruments, UK). The EBSD data was collected using software package AZtec 5.0 (C-Nano, Oxford Instruments, UK). The average grain sizes of the microstructure of the sample were calculated using ImageJ software [16].

Prior to the TE measurements, the sintered ceramics were cut and polished to obtain the required shapes and sizes. For the electrical measurements, the samples were cut from the sintered pellets into rectangular bars with dimensions of 2.5 mm × 2.5 mm × 8 mm. On the other hand, for thermal conductivity measurements, samples were cut into square plates with dimensions of 5 mm × 5 mm × 1 mm. The electrical conductivity, σ, and the Seebeck coefficient, S, were simultaneously measured in air using a four-probe DC method and a temperature-differential method, respectively, on a RZ2001i (Ozawa Science, Japan). The reproducibility of the σ and S measurements was confirmed by well-overlapped results for heating and cooling paths in a range of 27–800°C. The thermal diffusivity, α, and the specific heat, C_p, at 27–800°C were measured simultaneously with an LFA-502 (Kyoto Electronics, Japan) using a laser-flash method under vacuum. The absolute values of C_p of the samples were determined by comparing a molybdenum standard sample as a reference. The C_p values were also calculated using the Dulong–Petit law [17]. The total thermal conductivity was calculated using the relation $\kappa = \alpha\, C_p\, d_s$, where d_s is the sample density.

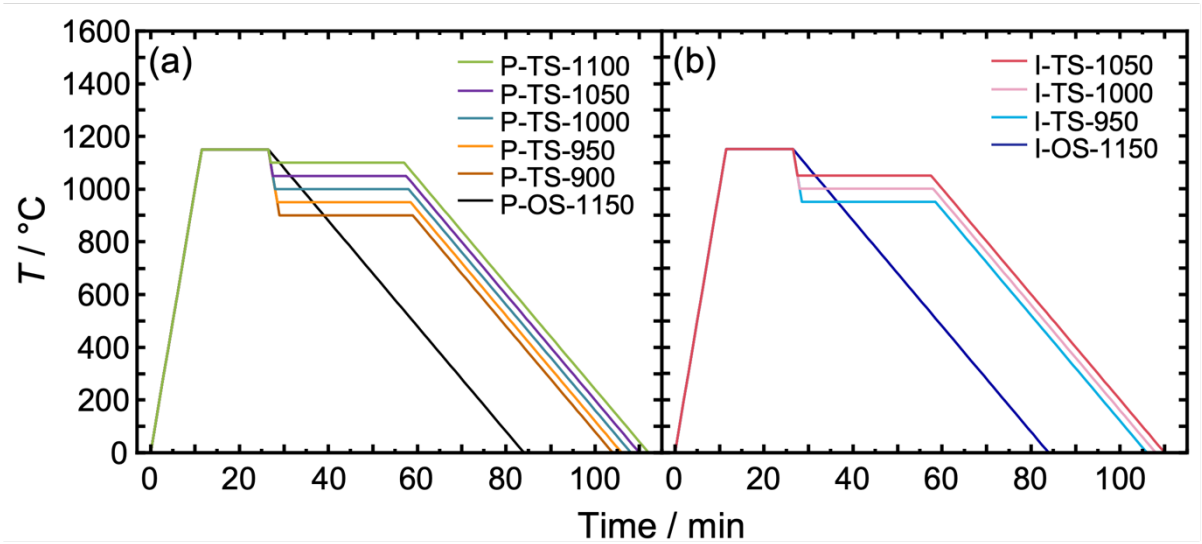

Fig. 42. Temperature profiles of the OS/TS-SPS processes for (a) pure and (b) In-doped ZnO ceramic samples.

5.3. Results and Discussion

5.3.1. Microstructural Analysis of Pure/In-doped ZnO

Figure 43 shows the XRD patterns of the pure/In-doped ZnO ceramics prepared by OS/TS-SPS. All of the XRD patterns were assigned to the wurtzite structure of ZnO with the $P6_3mc$ (186) space group regardless of the temperature and holding time of the OS/TS-SPS. There were many secondary phases such as homologous compounds [18], and sharp and narrow XRD peaks indicate that the samples have good crystallinity and fairly large crystallite sizes. Using the Rietveld refinement, the lattice constants of all samples were determined to be a = 0.325 nm and c = 0.521 nm, which are in good agreement with the literature values [19].

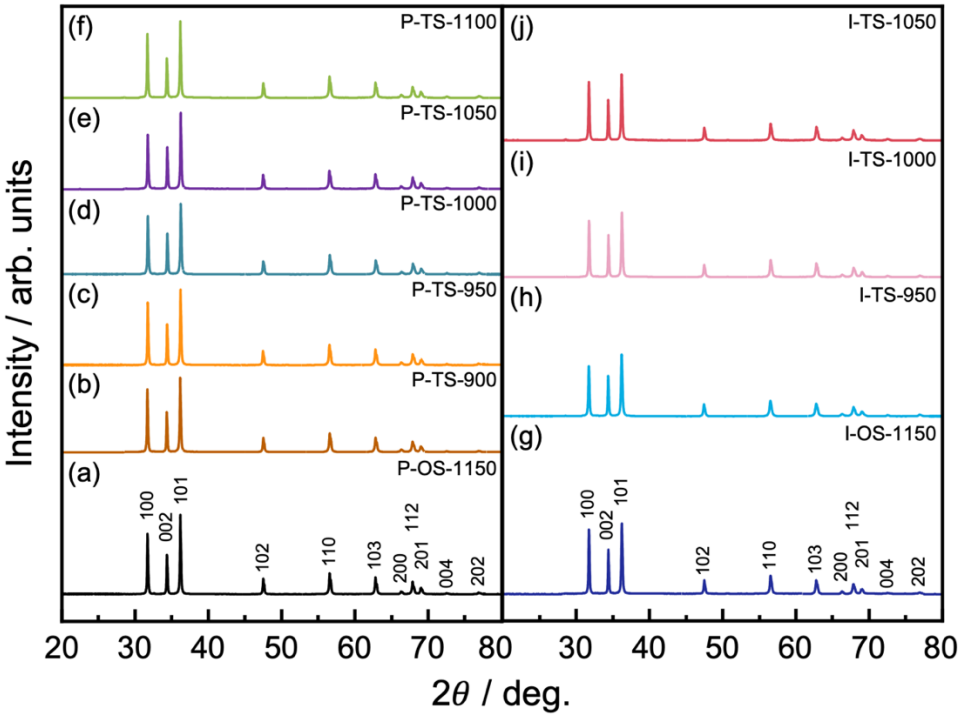

Fig. 43. X-ray diffraction patterns of (a)–(f) pure and (g)–(k) In-doped ZnO samples sintered by OS/TS-SPS in Table 8. The first-step sintering of (a)–(j) was at 1150°C for 15 min. The second-step sintering was maintained over a temperature range of 900–1100°C for 30 min.

Table 9. Relative densities of the OS/TS-SPS processes for pure and In-doped ZnO with various sintering conditions.

	Sample	Relative density (%)
Pure ZnO	P-OS-1150	96.5
	P-TS-900	98.1
	P-TS-950	97.9
	P-TS-1000	96.9
	P-TS-1050	98.3
	P-TS-1100	97.8
In-doped ZnO	I-OS-1150	94.6
	I-TS-950	95.3
	I-TS-1000	96.3
	I-TS-1050	95.5

The relative densities of the OS/TS-SPS pure/In-doped ZnO samples are summarized in Table 9. High relative densities of 94.6–98.3% were achieved for all samples. In the case of the TS-SPS pure/In-doped ZnO, the relative densities were higher than OS pure/In-doped ZnO (96.5% and 94.6%) in a range of 96.9–98.3% and 95.3–96.3%, respectively. The reason for the higher relative densities of TS-SPS samples than OS-SPS samples can be elucidated by the solid state sintering process. As for the driving force of sintering, the reduction in the total interfacial energy of the compact, which can be expressed by the following formula [20]:

$$\Delta(\gamma A) = \Delta\gamma A + \gamma\Delta A \qquad (1)$$

where γ is the specific surface (interface) energy, and A is the total surface (interface) area of the compact. The change in interfacial energy change ($\Delta\gamma$) is due to densification which is the replacement of solid/vapor interfaces (surface) by solid/solid surface in solid-state sintering,

and surface (interface) area change (ΔA) is attributed to grain coarsening (grain-growth). The reduction in total interfacial energy occurs though the densification and grain coarsening as the fundamental phenomena of sintering as shown in Fig. 44.

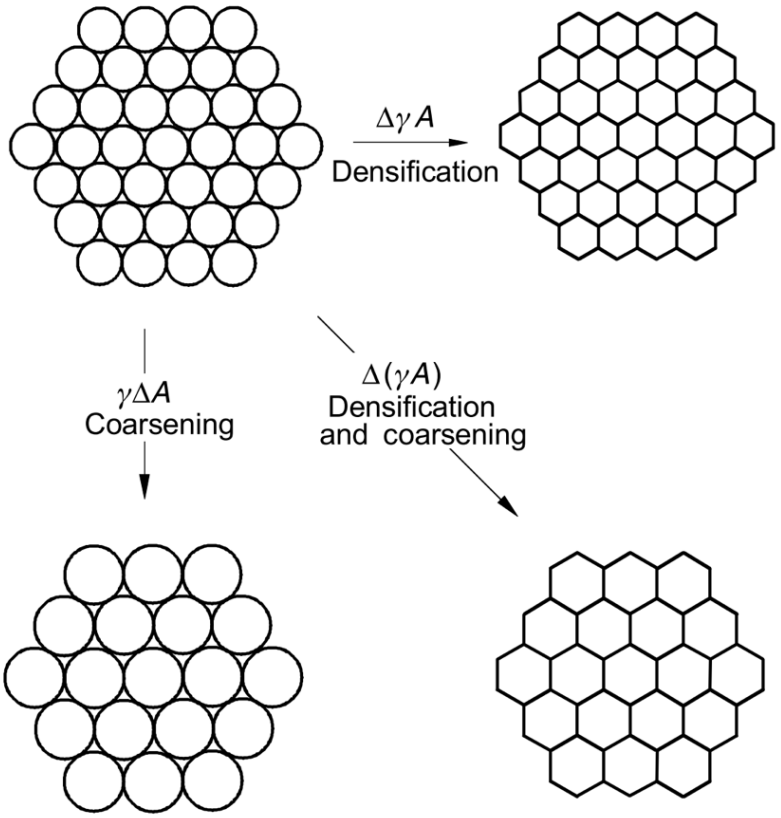

Fig. 44. Fundamental phenomena of sintering under the driving force, Δ (γA) [20].

The process of solid state sintering has three stages, including the early, intermediate, and final stages [21,22].

(i) Early stage: when the molded powder is heated, mass transport occurs at the contact point of particles (Fig. 45(a)). This stage is determined by the formation of necks between particles and involves irregular and angular pores. A partial area of the neck gradually increases with the growth of the neck part, and pores between the particles are surrounded by a large number of necks. Densification with 2–3% occurs at the early stage. At this stage, the pores between the

particles are almost connected from the surface of the molded body to the inside which is called an open pore [22].

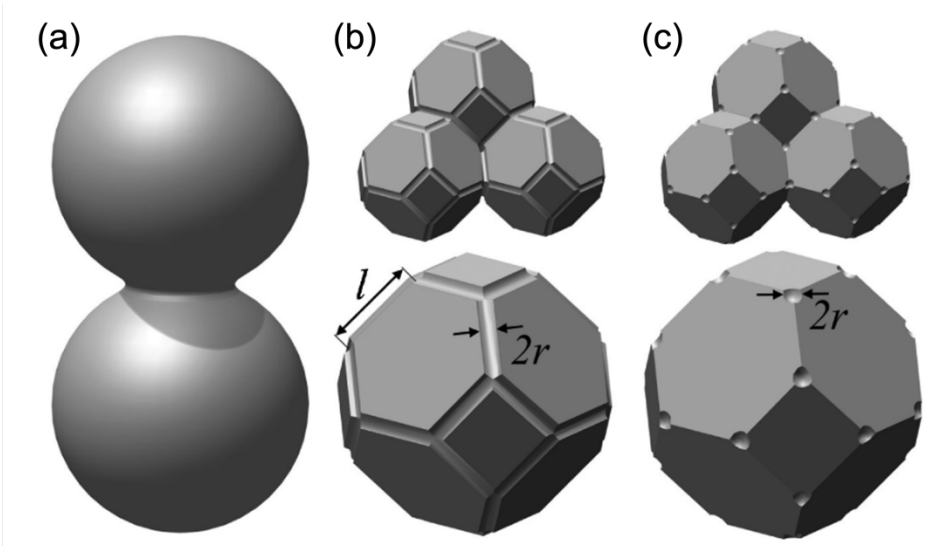

Fig. 45. Schematics of the sintering process at (a) early, (b) Intermediate, and (c) final stage [22].

(ii) Intermediate stage: the intermediate stage includes open pores. The volume of the open pores gradually shrinks, and the relative density increases by about 90–95%. Curvature around the pores continues to transfer mass and fill in concave areas. At the intermediate stage, the neck is large enough to overlap with interference. Particle rearrangement results in grains growth and pores shrinking [23]. As illustrated in Fig. 45(b), in the state of the open pore where all pores are connected through the ridge of the particles, and the pores are isolated from the apex part of the polyhedral particle to become a closed pore (Fig. 45 (c)).

(iii) Final stage: it involves mostly closed, and spherical pores and densification occurs from the state of the isolated pore to the final densification. In other words, pores remain at the corners of the polyhedral particles or in the particles, and the relative density is more than 95%. In the intermediate to final stage, the grain boundaries migrate and grain-growth occurs since

no pore exists to impede the process. Densification is completed by shrinking and disappearance of closed pores.

Therefore, it is explained that the reason for the increased density of TS-SPS samples compared with OS-SPS samples is the decrease of closed pores at the final stage of sintering through the prolonged sintering at low temperature for a longer duration than T_1. As a result, the TS-SPS process demonstrated a significant advantage in increasing the relative density as compared with our previous study (91.3 and 91.4–94.9%) [6,14].

Moreover, Moreover, differences in bulk pressure, vacancy concentration, and vapor pressure induce material transport. The phenomenon of material transport in solid-phase sintering and the kinetic analysis are summarized schematically. The following mechanisms of material movement that contribute to the growth of the neck in initial sintering are mentioned [20,22].

(i) Lattice diffusion (lattice diffusivity, D_l)

(ii) Grain boundary diffusion (grain boundary diffusivity, D_b)

(iii) Viscous flow (viscosity, η)

(iv) Surface Diffusion (surface diffusivity, D_s)

(v) Gas phase transport

- Evaporation/ condensation (vapor pressure difference, Δp)
- Gas diffusion (gas diffusivity, D_g)

The mass transport routes are shown for the transport mechanisms explained above (Fig. 46). Mass transport due to differences in interface curvature occurs under the parallel action of various mechanisms. Surface diffusion and grain boundary diffusion are the mass transportation using diffusion paths of free surfaces of particles, and grain boundary between particles, respectively. In particular, surface diffusion and particle diffusion become more important as the particle diameter of the raw material powder becomes finer. However, the

dominant mechanism may vary depending on the particle size, neck radius, temperature, and time of the given system.

Some of these mass transport mechanisms contribute to densification and shrinkage, on the other hand, others do not. The interparticle distance can only be reduced by the flow of bulk materials through viscous flow or the mass transport from the grain boundary by the movement of the atom. When the material comes from the surface of the particle to the neck, the distance between the particles does not decrease and the neck size increases due to the redistribution of the material. Thus, the grain boundary is a mass transport source for the densification and shrinkage of crystalline powder.

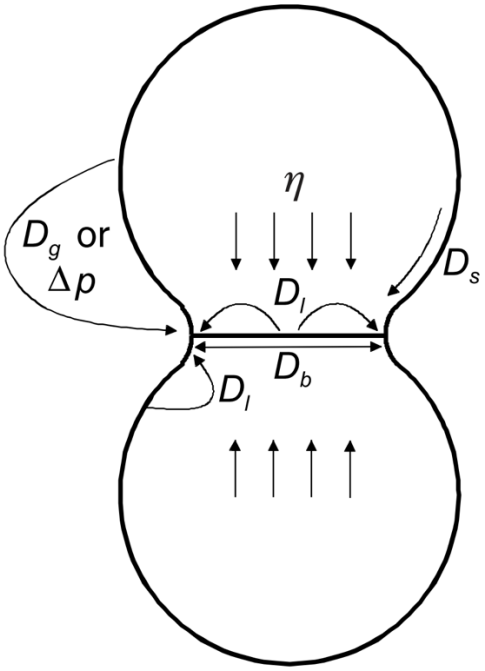

Fig. 46. Mass transport paths in the formation and growth of necks between particles during sintering [20].

EBSD measurement was carried out with an acceleration voltage of 20 kV and a step size of 0.05 μm to analyze the microstructure of the samples. To analyze the crystallite sizes and to image the crystal orientation, inverse pole figures (IPF) and IPF color maps are used to display

the crystallographic directions, the morphology, and the grain size. Figure 47 shows the IPF maps of (a) P-OS-1150, (b) P-TS-950, (c) I-OS-1150, and (d) I-TS-950. The black region of the IPF maps corresponds to regions where the EBSD failed to index the crystallographic orientation due to scratches from polishing, voids, or highly defective crystallinity of the grains. The IPF maps show no signs of preferred orientation, which is in agreement with the XRD data in Fig. 43.

P-OS-1150 and P-TS-950 consist of grains with average diameters of 7.9 and 6.8 μm, while I-OS-1150 and I-TS-950 have smaller grain sizes of 7.8 and 6.1 μm, on average, respectively. By comparing pure and In-doped ZnO, it was revealed that In-doping affects grain-growth. In other words, grain boundary migration is hindered by grain boundary pinning effect [24,25] in the ZnO matrix so that grain-growth is effectively suppressed. There are two possible reasons for this suppression of grain-growth by lowering the temperature in the second step. This can be elucidated as the sintering behavior of ZnO [26]. The grain-growth proceeds at a temperature range of around 700°C, but densification does not proceed. Since the first-step temperature (T_1 = 1150°C) is sufficiently high but the duration is very short (15 min = 0.9 ks) in the present study, the OS samples had low relative densities as compared with the TS samples, as shown in Table 9. This means that the OS samples have more intergrain spaces to allow for grain-growth during cooling. On the other hand, the TS samples underwent prolonged sintering during the second step in a range of 900–1100°C, where they could be sufficiently densified; thus, the grains in the TS samples have less space to grow during the subsequent cooling. Through the results, we could clearly prove the mechanism of TS which can achieve a high relative density with hindering grain-growth by pinning the grain boundaries through immobile triple junctions [27]. First, a sufficient number of triple junctions impede grain-boundary migration while achieving a critical density in the sample. Second, densification proceeds while grain-growth is avoided when the sintering temperature reaches T_2 [28]. It is expected that this

TS-SPS strategy could reduce thermal conductivity by maintaining fine grains and increasing the density of ZnO-based TE materials.

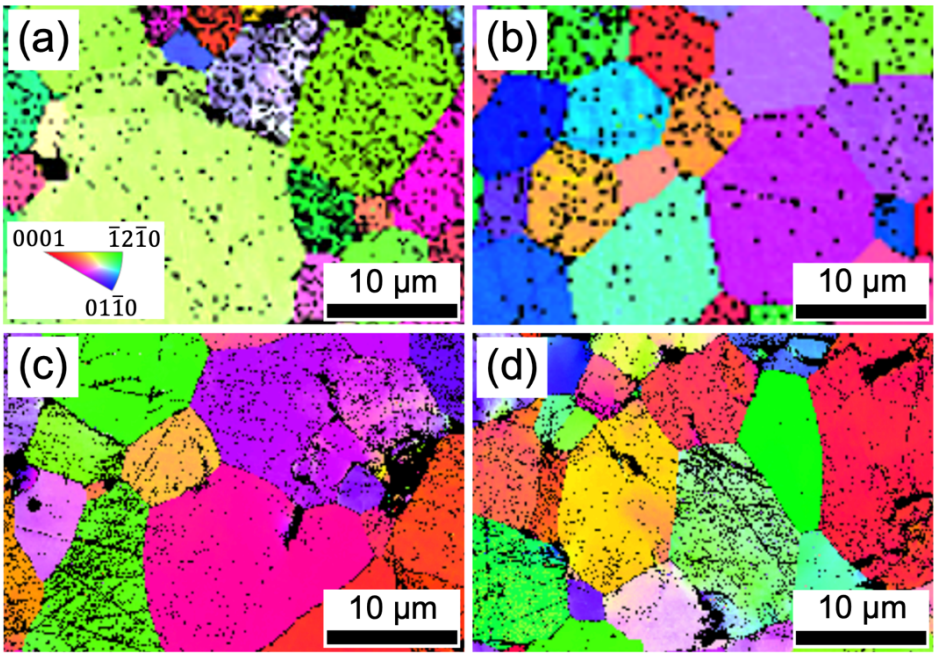

Fig. 47. Inverse pole figure (IPF) maps of the OS/TS-SPS pure and In-doped ZnO. The samples are (a) P-OS-1150, (b) P-TS-950, (c) I-OS-1150, and (d) I-TS-950. The EBSD color maps are assigned using the IPF color scale shown in (a).

5.3.2. Thermoelectric Properties

Figure 48 shows the temperature dependence of the electrical conductivity (σ), the Seebeck coefficient (S), and the power factor (PF, $S^2\sigma$) of the samples. The trade-off between σ and $|S|$ against the carrier concentration n can be given according to the Pisarenko relation [29].

The electrical conductivity of all samples gradually decreased as the temperature increased from 70 to 773°C, exhibiting a metallic behavior, in which the electrical conductivity decreases monotonically with increasing temperature, as shown in Fig. 48(a) and 48(b). Figure 48(b) showed very high electrical conductivities—as high as 3.0×10^2–4.3×10^2 S cm^{-1}—exhibiting

a metal-like behavior. By increasing the annealing temperature, the average grain size increases, which can be understood by considering the merging process during thermal annealing.

For ZnO particles, there are many dangling bonds related to the oxygen defects at the grain boundaries so that the I-TS-950 sample indicated a higher σ value (400 S cm^{-1} at 773°C) than those of the I-TS-1000 and I-TS-1050 samples. In contrast, the I-OS-1150 sample at 1150°C for 15 min has a lower σ value of 380 S cm^{-1} than the I-TS-950 sample does. Figures 48(a, c) and (b, d) shows a trade-off relationship between σ and $|S|$, where $|S|$ increased with increasing temperature. The S value of the P-TS-950 sample was –646 μV K^{-1} at 773°C, while that of the I-TS-950 sample was –158 μV K^{-1}. The PF values of the P-OS-1150 and P-TS-SPS 950 samples were 2.3 × 10^{-1} and 3.5 × 10^{-1} mW K^{-2} m^{-1}, respectively, as shown in Fig. 48(e). Although the highest PF value in the present study was 1.0 mW K^{-2} m^{-1} for the I-TS-950 sample, the highest PF value attained in our previous study was 6.0 × 10^{-1} mW K^{-2} m^{-1} for the I-OS-1150 sample (In-doped ZnO) [7]. These results strongly suggest that the TS-SPS process effectively improves the PF, and consequently, TS-SPS In-doped ZnO achieved much higher PF and higher ZT values.

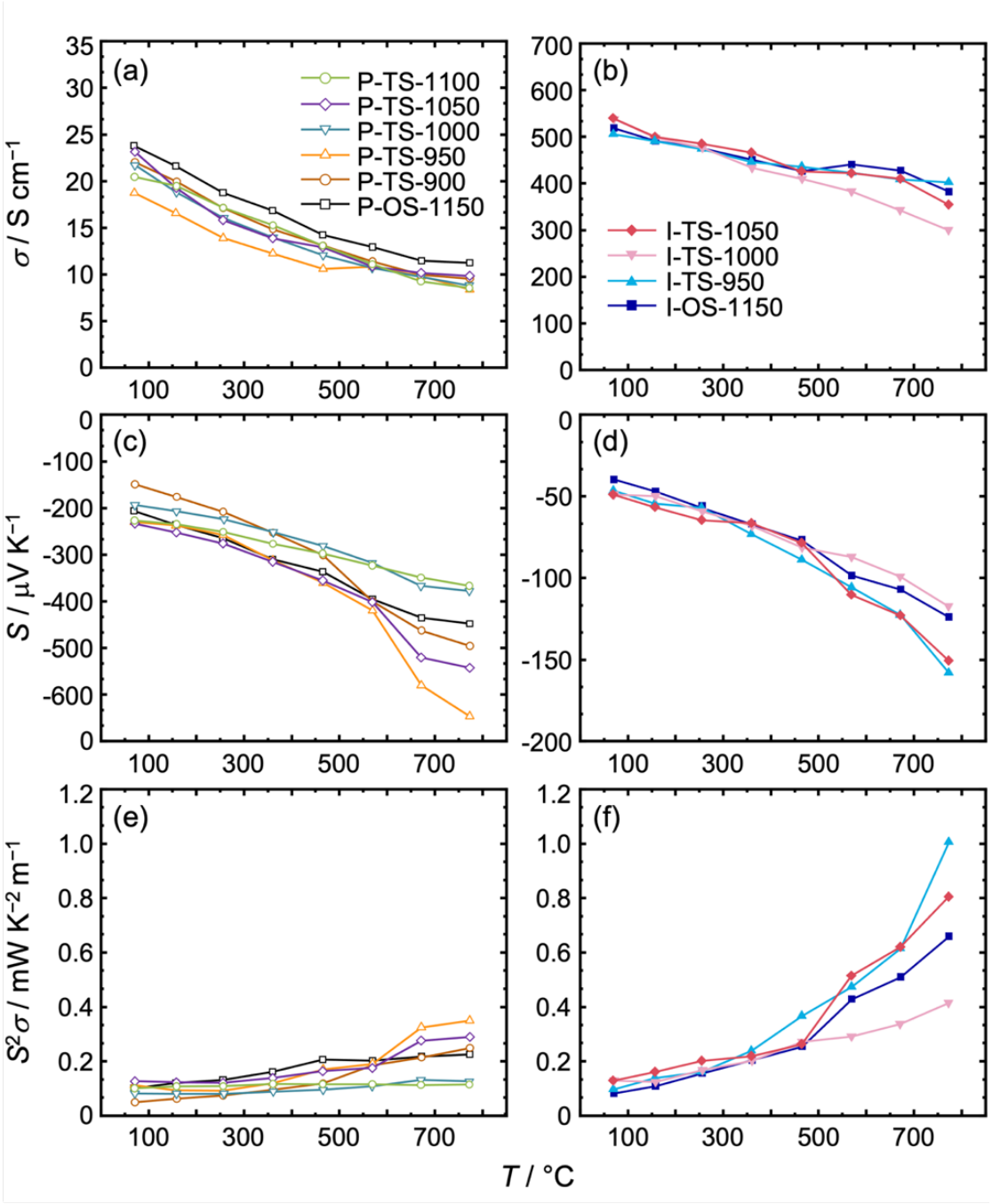

Fig. 48. Temperature dependences of (a, b) the electrical conductivity σ, (c, d) the Seebeck coefficient S, and (e, f) the power factor $S^2\sigma$ are shown: (a), (c), and (e) OS/TS-SPS pure and (b), (d), and (f) In-doped ZnO ceramic samples. First-step sintering of all samples was at 1150°C for 15 min. Second-step sintering was maintained over a temperature range of 900–1100°C for 30 min, and the number of "XX" in TS-XX samples indicated each sintering temperature.

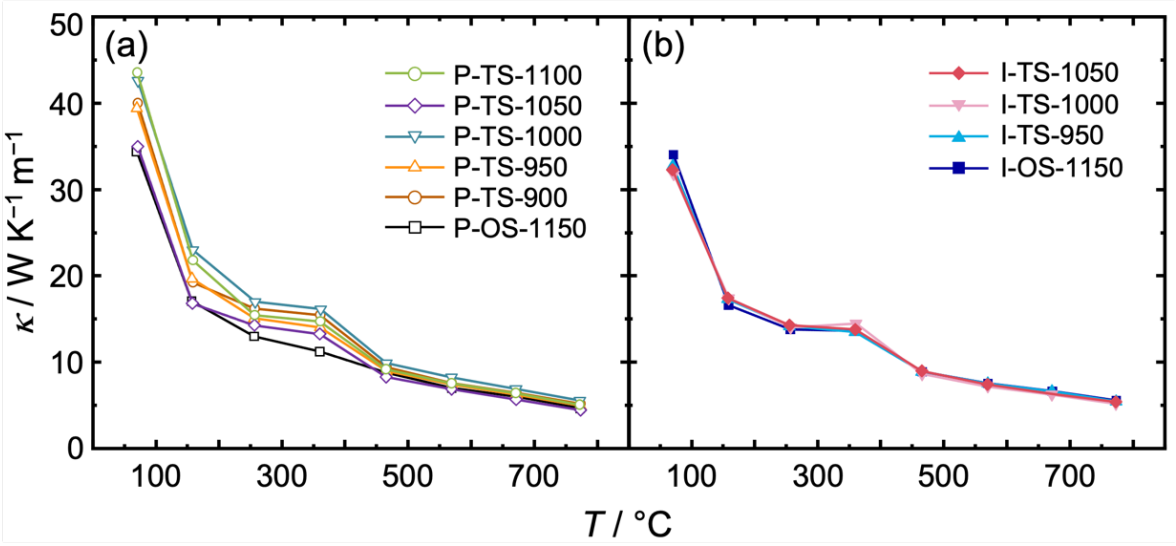

Fig. 49. Temperature dependence of the thermal conductivity κ of (a) the OS/TS-SPS pure and (b) the In-doped ZnO ceramic samples. First-step sintering of all samples was at 1150°C for 15 min. Second-step sintering was maintained over a temperature range of 900–1100°C for 30 min, and the number of "XX" in TS-XX samples indicated each sintering temperature.

Figure 49 shows the temperature dependence of the thermal conductivity of the OS/TS-SPS pure/In-doped ZnO samples. The thermal conductivity of the samples decreased substantially as temperatures increased due to increasing phonon–phonon scattering [30,31]. The P-OS-1150 sample (grain size 7.9 μm) indicated a lower thermal conductivity of 4.6 W K^{-1} m^{-1} as compared with the value of 5.2 W K^{-1} m^{-1} for P-TS-950, with an average grain size of 6.8 μm at 773°C, as seen in Fig. 49(a). However, the I-TS-950 sample, with an average grain size of 6.1 μm, showed a slightly lower thermal conductivity of 5.4 W K^{-1} m^{-1}, as compared with a higher value of 5.5 W K^{-1} m^{-1} at 773°C for I-OS-1150 with an average grain size of 7.8 μm, as shown in Fig. 49(b). Even these values of thermal conductivities are similar in a range of 5.2−5.5 W K^{-1} m^{-1}, but it may be elucidated that In-doped ZnO was more suitable for the OS/TS-SPS processes to decrease the thermal conductivities, since In as a dopant plays a role

in the pinning effect [24,25]. Figure 49 (b) shows the thermal conductivity of the I-OS/TS-SPS samples with T_1 = 1150°C for 15 min and T_2 = 950, 1000, and 1050°C for 30 min. Among the TS-SPS samples, the I-TS-1000 sample (relative density 96. 3%) showed the lowest thermal conductivity, 5.2 W K^{-1} m^{-1} at 773°C, whereas the lowest thermal conductivity for In-doped ZnO (relative density 92. 5%) formed by OS-SPS at 1150°C in our previous study was 5.3 W K^{-1} m^{-1} at 773°C [7]. It is thus implied that the decrease in sintering temperature (T_2) in the TS-SPS process might reduce thermal conductivity while keeping a high relative density.

The dimensionless figure of merit (*ZT*) of the OS/TS-SPS pure and In-doped ZnO samples is indicated in Fig. 50. Figure 50(a) shows that P-OS/TS-SPS samples have *ZT* values of 0.024–0.074, lower than *ZT* values (0.083–0.194) of I-OS/TS-SPS samples in Fig. 50(b). On the contrary, the I-TS-950 sample had a higher *ZT* value (0.194) than those in previous studies, such as OS-SPS In-doped ZnO (*ZT* = 0.118) and OS-SPS In/Ga dual-doped ZnO (*ZT* = 0.165) [7]. Moreover, it should be noted that *ZT* value of In-doped ZnO is higher than that of pure ZnO, and In dopant is essential for *ZT*, as supported by the EBSD results presented in Fig. 47(c) and 47(d). In other words, the TS-SPS process demonstrates that the *ZT* value of the present pure/In-doped ZnO sample can be improved by optimizing their microstructures.

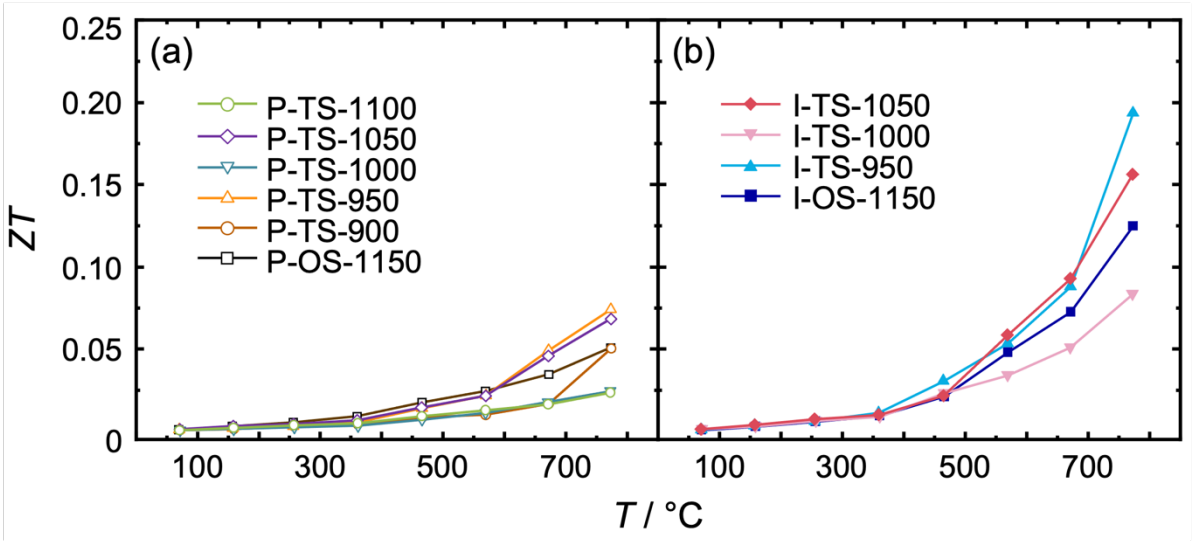

Fig. 50. Dimensionless figure of merit *ZT* of (a) the OS/TS-SPS pure and (b) In-doped ZnO ceramic samples. First-step sintering of all samples was at 1150°C for 15 min. Second-step sintering was maintained over a temperature range of 900–1100°C for 30 min, and the number of "XX" in TS-XX samples indicated each sintering temperature.

5.4. Conclusions

Pure and In-doped ZnO thermoelectric ceramics were prepared by OS/TS-SPS processes, and the effect of the TS-SPS process on the relative density, grain size, and TE performance of ZnO ceramics was investigated. XRD analysis showed that there were many secondary phases, and the wurtzite structure of ZnO was evident regardless of the temperature and holding time of OS/TS-SPS. High relative densities of 94.6–98.3% were achieved without significant grain-growth. Thus, the TS-SPS process proved to have a significant advantage for increasing the relative density. The EBSD results revealed a noticeable suppression of grain-growth (21.8%, reduced from 7.8 to 6.1 μm) in I-OS-1150 and I-TS-950 samples with T_1 = 1150°C and T_2 = 950°C.

The highest *PF*, 1.0 mW K^{-2} m^{-1}, was achieved for the I-TS-950 sample, attaining an increased *ZT* (55.2%, from 0.125 to 0.194 compared with I-OS-1150) at 773°C. The *PF* value was higher than that of the In-doped ZnO sample in our previous study [7], proving that the TS-SPS process is an effective strategy for improving *PF*, strongly suggesting that the carrier doping to TS-SPS ZnO achieves much higher *PF* and, therefore, higher *ZT* values. This new TS-SPS strategy can provide an opportunity for significant progress in developing ZnO-based TE materials.

References

[1] T. Mori, S. Priya, Materials for energy harvesting: At the forefront of a new wave, MRS Bull. 43 (2018) 176–180.

[2] L.D. Zhao, B.P. Zhang, J.F. Li, H.L. Zhang, W.S. Liu, Enhanced thermoelectric and mechanical properties in textured n-type Bi_2Te_3 prepared by spark plasma sintering, Solid State Sci. 10 (2008) 651–658.

[3] K.H. Lee, S.W. Kim, Design and preparation of high-performance bulk thermoelectric materials with defect structures, J. Korean Ceram. Soc. 54 (2017) 75–85.

[4] P.Y. Deng, K.K. Wang, J.Y. Du, H.J. Wu, From dislocation to nano-precipitation: evolution to low thermal conductivity and high thermoelectric performance in n-Type PbTe, Adv. Funct. Mater. 30 (2020) 2005479.

[5] I. Terasaki, R. Okazaki, H. Ohta, Search for non-equilibrium thermoelectrics, Scr. Mater. 111 (2016) 23–28.

[6] A. Jeong, K. Suekuni, M. Ohtaki, B.K. Jang, Thermoelectric properties of In- and Ga-doped spark plasma sintered ZnO ceramics, Ceram. Int. 47 (2021) 23927–23934.

[7] A. Jeong, M. Ohtaki, B.K. Jang, Thermoelectric performance of In and Ga single/dual-doped ZnO ceramics fabricated by spark plasma sintering, Ceram. Int. 48 (2022) 14414–14423.

[8] O.K.T. Le, A.T.T. Pham, N.K. Pham, T.H.C. Pham, T.H. Nguyen, D.V. Hoang, H.K.T. Ta, D.C. Truong, H.T. Lai, T.D.T. Ung, V.C. Tran, T.B. Phan, Compensation of Zn substitution and secondary phase controls effective mass and weighted mobility in In and Ga co-doped ZnO material, J. Materiomics 7 (2021) 742–755.

[9] H. Cheng, X.J. Xu, H.H. Hng, J. Ma, Characterization of Al-doped ZnO thermoelectric materials prepared by RF plasma powder processing and hot press sintering, Ceram. Int. 35 (2009) 3067–3072.

[10] N.J. Lóh, L. Simão, C.A. Faller, A. De Noni, O.R.K. Montedo, A review of two-step sintering for ceramics, Ceram. Int. 42 (2016) 12556–12572.

[11] L. An, A. Ito, T. Goto, Two-step pressure sintering of transparent lutetium oxide by spark plasma sintering, J. Eur. Ceram. Soc. 31 (2011) 1597–1602.

[12] M.Y. Chu, L.C. De Jonghe, M.K.F. Lin, F.J.T. Lin, Precoarsening to improve microstructure and sintering of powder compacts, J. Am. Ceram. Soc. 74 (1991) 2902–2911.

[13] B.K. Jang, Y. Sakka, N. Yamaguchi, H. Matsubara, H.T. Kim, Thermal conductivity of EB-PVD ZrO_2-4mol% Y_2O_3 films using the laser flash method, J. Alloys Compd. 509 (2011) 1045–1049.

[14] A. Jeong, M. Ohtaki, B.K. Jang, Characterization of ZnO thermoelectric ceramics and their microstructures consolidated by two-step spark plasma sintering, J. Ceram. Soc. Jpn. 130 (2022) 889–894.

[15] L.B. McCusker, R.B. Von Dreele, D.E. Cox, D. Louër, P. Scardi, Rietveld refinement guidelines, J. Appl. Crystallogr. 32 (1999) 36–50.

[16] M. Doube, M.M. Klosowski, I. Arganda-Carreras, F.P. Cordelières, R.P. Dougherty, J.S. Jackson, B. Schmid, J.R. Hutchinson, S.J. Shefelbine, BoneJ: Free and extensible bone image analysis in ImageJ, Bone. 47 (2010) 1076–1079.

[17] S.O. Yurchenko, K.A. Komarov, N.P. Kryuchkov, K.I. Zaytsev, V.V. Brazhkin, Bizarre behavior of heat capacity in crystals due to interplay between two types of anharmonicities, J. Chem. Phys. 148 (2018) 134508.

[18] H.J. Cho, Y. Wu, Y.Q. Zhang, B. Feng, M. Mikami, W. Shin, Y. Ikuhara, Y.M. Sheu, K. Saito, H. Ohta, Anomalously Low Heat Conduction in Single-Crystal Superlattice Ceramics Lower Than Randomly Oriented Polycrystals, Adv. Mater. Interfaces 8 (2021) 1–8.

[19] Ü. Özgür, Y.I. Alivov, C. Liu, A. Teke, M.A. Reshchikov, S. Doğan, V. Avrutin, S.J. Cho, H. Morkoç, A comprehensive review of ZnO materials and devices, J. Appl. Phys. 98 (2005) 041301.

[20] S.J.L. Kang, Sintering: densification, grain growth, and microstructure, Elsevier Butterworth-Heinemann (2005) Ch.1, pp. 6–7.

[21] S. Mirzababaei, S. Pasebani, A review on binder jet additive manufacturing of 316L stainless steel, J. Manuf. Mater. Process. 3 (2019) 82.

[22] H. Yoshida, Fundamentals of sintering: ―theory and practice ― II. densification kinetics, Mater. Jpn. 58 (2019) 677–683.

[23] B.N. Kim, T.S. Suzuki, K. Morita, H. Yoshida, J.G. Li, H. Matsubara, Theoretical analysis of experimental densification kinetics in final sintering stage of nano-sized zirconia, J. Eur. Ceram. Soc. 39 (2019) 1359–1365.

[24] B.K. Jang, Microstructure of nano SiC dispersed Al_2O_3-ZrO_2 composites, Mater. Chem. Phys. 93 (2005) 337–341.

[25] H.L. Zhuang, J. Pei, B. Cai, J. Dong, H. Hu, F.H. Sun, Y. Pan, G.J. Snyder, J.F. Li, Thermoelectric performance enhancement in BiSbTe alloy by microstructure modulation via cyclic spark plasma sintering with liquid phase, Adv. Funct. Mater. 31 (2021) 1–11.

[26] M. Mazaheri, A.M. Zahedi, S.K. Sadrnezhaad, Two-step sintering of nanocrystalline ZnO compacts: Effect of temperature on densification and grain growth, J. Am. Ceram. Soc. 91 (2008) 56–63.

[27] Z.R. Hesabi, M. Haghighatzadeh, M. Mazaheri, D. Galusek, S.K. Sadrnezhaad, Suppression of grain growth in sub-micrometer alumina via two-step sintering method, J. Eur. Ceram. Soc. 29 (2009) 1371–1377.

[28] U. Czubayko, V.G. Sursaeva, G. Gottstein, L.S. Shvindlerman, Influence of triple

junctions on grain boundary motion, Acta Mater. 46 (1998) 5863–5871.

[29] J. Androulakis, I. Todorov, D.Y. Chung, S. Ballikaya, G. Wang, C. Uher, M. Kanatzidis, Thermoelectric enhancement in PbTe with K or Na codoping from tuning the interaction of the light- and heavy-hole valence bands, Phys. Rev. B. 82 (2010) 115209.

[30] R.V.R. Virtudazo, B. Srinivasan, Q. Guo, R. Wu, T. Takei, Y. Shimasaki, H. Wada, K. Kuroda, S. Bernik, T. Mori, Improvement in the thermoelectric properties of porous networked Al-doped ZnO nanostructured materials synthesized via an alternative interfacial reaction and low-pressure SPS processing, Inorg. Chem. Front. 7 (2020) 4118–4132.

[31] E. Guilmeau, P. Díaz-Chao, O.I. Lebedev, A. Rečnik, M.C. Schäfer, F. Delorme, F. Giovannelli, M. Košir, S. Bernik, Inversion boundaries and phonon scattering in Ga:ZnO thermoelectric compounds, Inorg. Chem. 56 (2017) 480–487.

Chapter 6. Conclusions

Advanced TE materials with excellent performance in various applications have been constantly developed due to rapidly developing TE science and technology. It is found that effective ZnO dopants can achieve higher electrical conductivity and lower thermal conductivity. Therefore, the first objective is to investigate TE parameters such as electrical conductivity, Seebeck coefficient, thermal conductivity, and *ZT* for the ZnO TE materials before and after doping, and their relation with these parameters changing. The final objective is to apply the new TS-SPS processes with achieving a critical density of > 75% theoretical density at the first heating step and densification while preventing grain-growth at the second heating step to improve *PF*, strongly suggesting that the carrier doping to TS-SPS ZnO achieves much higher *PF* and, therefore, higher *ZT* values. The following are outlined conclusions of each chapter.

Chapter 2. Thermoelectric Properties of In- and Ga-doped Spark Plasma Sintered ZnO Ceramics

In- and Ga-doped consolidated ZnO, $[Zn_{(1-x-y)}Ga_xIn_y]O$, ceramics were fabricated via SPS, and the solubility of dopants and the correlation between crystal structure and various compositions on the TE properties were investigated. Crystal structure and microstructural analyses indicated the presence of a spinel secondary phase ($ZnGa_2O_4$) with a high relative density, and $ZnGa_2O_4$ disappeared as In increased from y = 0 to 0.005. It can be concluded that the addition of In contributed to the increase in the solubility of Ga because doping with In and Ga (x = 0.02; y = 0.005) enabled higher doping of Ga. Consequently, doping with In and Ga could achieve the highest *PF* of 0.99 mW K^{-2} m^{-1} at 773°C, and reduce the thermal conductivity, attaining *ZT* = 0.003–0.015 from 67 to 257°C.

Chapter 3. Thermoelectric Performance of In and Ga Single/Dual-doped ZnO Ceramics Fabricated by SPS

For the comparison of In single, and In and Ga dual doping effect on ZnO, the sintered bodies of In single-doped, and In and Ga dual-doped ZnO ceramics were consolidated via SPS. The microstructural and chemical composition analyses indicated that the secondary phases of $Zn_7In_2O_{10}$ and $ZnGa_2O_4$ existed in the single/dual doped ZnO. Through the TE characterization, it was revealed that the segregation of $ZnGa_2O_4$ phase affected to decrease electrical conductivity. Although the presence of secondary phases, the highest *PF* and the lowest thermal conductivity were achieved for dual-doped ZnO. Hence, the substitution of Zn by In and Ga is a promising approach to increase the values of *PF* of ZnO by tuning its carrier concentration. Therefore, the In and Ga dual doping of ZnO was beneficial in improving its TE performance.

Chapter 4. Characterization of ZnO Thermoelectric Ceramics and Their Microstructures Consolidated by Two-Step Spark Plasma Sintering

To investigate the effect of control of grain sizes on TE properties, the density, grain size, and TE performance of pure ZnO ceramics were studied by applying OS/TS-SPS processes with temperature profiles. High relative densities of 91.4–94.9% were achieved except for OS-1150 (85.6%). The TS-SPS process thus proved a significant advantage for increasing the relative density. Moreover, a noticeable suppression of grain-growth (56%, reduced from 8.1 to 3.6 μm) for the TS-1100-120 sample proved the effect of fine-grained microstructures. The value of *PF*, 7.8×10^{-5} W K^{-2} m^{-1} at 775°C (TS-1100-120) was higher than that of the OS-SPS pure ZnO sample in chapter 3, indicating that the TS-SPS process is effective to improve *PF*.

Chapter 5. Effects of Two-Step Spark Plasma Sintering on the Microstructures and Thermoelectric Properties of Pure/In-doped ZnO

Pure and In-doped ZnO ceramics were successfully prepared by SPS with OS/TS temperature profiles to optimize the TS-SPS process. High relative densities of 94.6–98.3% were achieved without significant grain-growth. It was revealed that a noticeable suppression of grain-growth (21.8%, reduced from 7.8 to 6.1 μm) in OS-SPS and TS-SPS samples with T_1 = 1150°C and T_2 = 950°C. The highest *PF*, 1.0 mW K^{-2} m^{-1}, was achieved for the TS-SPS sample, attaining an increased *ZT* (55.2%, from 0.125 to 0.194 compared with I-OS-1150) at 773°C. The *ZT* value was the highest value of In and Ga dual-doped ZnO in this thesis, proving that the TS-SPS process is an effective strategy for improving *PF*, strongly suggesting that the carrier doping to TS-SPS ZnO achieves much higher *PF* and, therefore, higher *ZT* values.

The main challenge was to improve the TE performance of In and Ga dual-doped ZnO. Although the optimization of doping with In and Ga in ZnO was successfully conducted, the reduction of thermal conductivity could not be significantly improved. As an alternative to the fine-grained microstructure, TS-SPS processes were applied to non-doped and In-doped ZnO for the first time. Through the temperature profiles, the TS-SPS process was divided into two kinds of steps to achieve a high critical density and densification while preventing grain-growth at the first and second heating steps, respectively. As a result, it was possible to achieve the fine-grained microstructure that a noticeable suppression of grain-growth (21.8%, compared with In-doped OS-SPS) with a relative density of 96%.

The meaningful enhancement of the ZnO TE ceramics in TE properties was achieved by doping and applying the TS-SPS process. Consequently, it is expected that the new TS-SPS strategy can provide a new opportunity for significant contribution to ZnO-based TE materials.

Research Achievements

1. List of published papers

[1] **A. Jeong** and B.K. Jang, “Effects of two-step spark plasma sintering on the microstructures and thermoelectric properties of Pure/In-doped ZnO”, Materials Science and Technology of Japan, 59 (2022) 33–39.

[2] **A. Jeong**, M. Ohtaki, and B.K. Jang, “Characterization of ZnO thermoelectric ceramics and their microstructures consolidated by two-step spark plasma sintering”, Journal of the Ceramic Society of Japan, 130 (2022) 889–894.

[3] **A. Jeong**, M. Ohtaki, and B.K. Jang, “Thermoelectric performance of In and Ga single/dual-doped ZnO ceramics fabricated by spark plasma sintering”, Ceramics International, 48 (2022) 14414–14423.

[4] **A. Jeong**, K. Suekuni, M. Ohtaki, and B.K. Jang, “Thermoelectric properties of In- and Ga-doped spark plasma sintered ZnO ceramics”, Ceramics International, 47 (2021) 23927–23934.

- 解説

[1] ジョン アロン, 大瀧 倫卓, 張 炳國, “酸化物系熱電材料の研究開発動向”, 材料の科学と工学, 58 (2021) 18–21.

2. List of international academic conferences

[1] **A. Jeong**, M. Ohtaki, and B.K. Jang, "Effect of Doping with Indium and Gallium on Thermoelectric Properties in Zinc Oxide", at the ICACC 2022 (The 46th International Conference and Exposition on Advanced Ceramics Composites), Online conference, 01/23-28 (2022).

[2] **A. Jeong** and B.K. Jang, "Thermoelectric Performance of ZnO Ceramics Co-doped with Ga and In Fabricated by Spark Plasma Sintering", at the 23rd CSS-EEST (Cross Straits Symposium on Energy and Environmental Science and Technology), Online conference, 12/02-03 (2021).

[3] **A. Jeong** and B.K. Jang, "Thermoelectric Properties and Microstructure of In- and Ga-doped ZnO fabricated by Spark Plasma Sintering", at the IEICES-2021 (International Exchange and Innovation Conference on Engineering & Science), Online conference, 10/21-22 (2021).

3. List of domestic academic conferences

[1] ジョン アロン, 大瀧 倫卓, 張 炳國, "Thermoelectric Characterization of In and Ga Single/Dual-doped ZnO Consolidated by Spark Plasma Sintering", 日本熱電学会学術講演会 (TSJ2022), アオーレ長岡, 長岡, 08/08-10 (2022).

[2] ジョン アロン, 大瀧 倫卓, 張 炳國, "Synthesis and Thermoelectric Characterization of In and Ga co-doped ZnO by Spark Plasma Sintering", 日本材料科学会, 2022 年度学術講演大会, オンライン開催, 05/18-19 (2022).

[3] ジョン アロン, 大瀧 倫卓, 張 炳國, "Microstructure and Thermoelectric Properties of In- and Ga-doped ZnO consolidated by Spark Plasma Sintering", 日本セラミックス協会 2022 年年会, オンライン開催, 03/10-12 (2022).

[4] ジョン アロン, 末國 晃一郎, 大瀧 倫卓, 張 炳國, "Effect of Doping Concentration on the Thermoelectric Properties of In and Ga doped ZnO by Spark Plasma Sintering", 日本材料科学会, 2021 年度学術講演大会, オンライン開催, 05/20-21 (2021).

[5] ジョン アロン, 末國 晃一郎, 大瀧 倫卓, 張 炳國, "Thermoelectric Performance of In and Ga Co-doped ZnO Fabricated by Spark Plasma Sintering", 日本セラミックス協会 2021 年年会, オンライン開催, 03/23-25 (2021).

Acknowledgments

I would like to appreciate my esteemed supervisor Prof. Byung-Koog Jang for his invaluable supervision, full support, effort in research, and guidance of daily during the doctoral course at Kyushu University. During the short term of two and a half years for the Ph. D. course, he made me grow up through his outstanding guidance on the way how to set up originality, research direction, experimental procedures, and methods of solving problems for thermoelectric research. He gave me a roadmap on the TS-SPS process with doping on thermoelectric materials. Based on the guidance, I learned how to be a self-directed learner and to prepare academic papers professionally as the most important task so I would like to show respect to Prof. Jang. His continuous supervision with plentiful experience has encouraged me in all the time of my academic research. The guidance of my professor that I had never received anywhere else, and it was by far the best. I have been extremely lucky to have a supervisor who cared so much about my research. Consequently, I have achieved significant research achievements, leading to a post-doctoral fellowship.

I am extremely grateful to Prof. Michitaka Ohtaki and Prof. Koichiro Suekuni for their immense knowledge, experimental support, and academic discussion regarding thermoelectric materials. I would like to express my gratitude to Prof. Michitaka Ohtaki, Prof. Koichiro Suekuni, Prof. Ken Watanabe, and Prof. Koji Miyazaki for their informative comments and guidance as the thesis committee, and Prof. Kiichi Hamamoto for dealing with the process of the early graduation although their schedule is quite tight.

I would like to express appreciation to Prof. Kyuhyoung Lee during the research on the preparation of sheet Al-doped ZnO by hydrothermal synthesis at Yonsei University. He helped me to plan my research theme and gave me valuable discussion as a supervisor. Also, I am grateful to Prof. Hiromichi Ohta during the research on thermoelectric performance of the

epitaxial thin films of In and Ga dual-doped ZnO at Hokkaido University. Thanks to the opportunities, I learned a lot in the thermoelectric research field at different universities. Moreover, I am tremendously appreciative of the sincere advice and mentorship of Prof. Jondo Yun and Prof. Si-Young Choi and their encouragement helped me to endure a rough time abroad.

On campus, I would like to thank Ms. Rumiko Ide and Ms. Kyoko Nozoe, staff of the major office for their help with administrative processes without any problems during the Ph.D. course. Also, my appreciation also goes out to our lab mates Ji-Hwoan Lee and Seung-Hyeon Kim for team spirit. I could not have done it without our lab members. Particularly, I am really grateful to my friends, Seungwon Lee, Kayoung Park, Hyungrok Jo, Taeyoung Kim, Kwangsu Kim, Shoya Iwanami, Junyoung Heo, Katsuaki Hashikuni, Nhat Quang Minh Tran, Maneeyom Sasikan, and Yuki Miwa. Thanks for having my back and helping for the research. My gratitude extends to Rotary Yoneyama Memorial Foundation and Mr. Takayuki Yamada for the scholarship opportunity to undertake my studies at Kyushu University.

First and foremost, I must express my very profound gratitude to my beloved parents for their wholehearted support throughout my years of study, especially Ph. D. course. My parents always suggested to me that I should do what I hope to do and achieve it without regret. I will never forget their devoted care and trust. This accomplishment would not have been possible without them. Thank you for always believing in me. I will remember forever what you have guided me.

Finally, I am convinced that the valuable research and academic activities will be my biggest asset during two and a half years on Chikushi Campus at Kyushu University. Thank you for your goodness in my life.

January, 2023

ジョン　アロン

JEONG AHRONG